ABSTRACT

Title of Document: DEVELOPMENT OF ION-MOBILITY AND MASS SPECTROMETRY FOR PROBING THE REACTIVITY OF NANOPARTICLES AND NANOCOMPOSITES

Lei Zhou, Doctor of Philosophy, 2009

Directed By: Michael R. Zachariah, Professor
Chemical Physics Program
Department of Mechanical Engineering and Chemistry

Aerosols of diameter smaller than 100 nm, usually are referred as nanoparticles or ultrafines, have received considerable interests lately as a source of building blocks to novel materials. However, our capabilities for charactering these materials are greatly limited by lack of appropriate diagnostic tools. The objective of this work is to develop new aerosol-based techniques for the characterization of nanoparticles and nanocomposites. Though the scope of this dissertation is focused on probing the reactivity of metal based nanoparticles/nanocomposites and their applications in energetic materials, the methods provide generic approaches for understanding the intrinsic reactivity of nanoparticles.

Real-time single particle mass spectrometry (SPMS) has been used to study the reactivity of aluminum nanoparticles. The SPMS is a powerful tool due to its

ability to obtain quantitative information at the single particle level. Here in this work, we conducted extensive investigations on the quantification of the SPMS. Particle morphology and composition biases on quantifying the composition of nanoparticles were observed experimentally, was related to the high non-linear properties of the laser-particle interaction. To understand pulsed laser interaction with nanoparticles, as it applied to the implementation and quantification of SPMS, we employed a one-dimensional hydrodynamic model to determine the characteristic behavior of ions produced from the particle. In the simulation, the temporal evolution of the ionization state and energy were evaluated as a function of aluminum particle size that were heated and ionized by a nanosecond laser. The results are shown to be consistent with our experimental observation, and suggest that particle size-dependent energetic ions led to the power law relationship between peak area and particle size observed in our single particle mass spectrometer.

Another approach to probe the reactivity of the nanoparticles is an ion-mobility spectrometry method. The basic idea of the experimental approach is to prepare nanoparticles of well characterized size/shape, and monitor particle size and mass changes during oxidation in free-flight. In this work, we studied nickel nanoparticles oxidation. Particles of well-controlled sizes and structure were generated in-situ, and subsequently size selected using a differential mobility analyzer (DMA). These particles were oxidized in a flow reactor at various temperatures and the size and mass change of the reacted particle were measured by a second DMA, or an aerosol particle mass analyzer (APM). We found the experimental data can be divided into an oxidation region, and a phase transition region. On the basis of the

diffusion-controlled rate equation in the shrinking core model, we obtained size-resolved activation energies for nickel nanoparticles oxidation, as well as the absolute burn time and the effective diffusion coefficient.

Finally, a new Time-of-Flight mass spectrometer (TOFMS) combined with a temperature jump (T-Jump) technique is developed for time resolved analysis of the ultrafast condensed phase reaction, with focus on the decomposition, ignition and combustion processes of solid energetic materials. As the first application of this instrument, nanocomposite thermite systems of aluminum/copper oxide (Al/CuO) and aluminum/iron oxide (Al/Fe_2O_3) were studied, and the possible reaction mechanism and reaction steps of nanocomposite thermites were discussed based on time-resolved mass spectra measurements obtained from T-Jump/TOF mass spectrometry.

DEVELOPMENT OF ION-MOBILITY AND MASS SPECTROMETRY FOR PROBING THE REACTIVITY OF NANOPARTICLES AND NANOCOMPOSITES

By

Lei Zhou

Dissertation submitted to the Faculty of the Graduate School of the
University of Maryland, College Park, in partial fulfillment
of the requirements for the degree of
Doctor of Philosophy
2009

Advisory Committee:
Professor Michael R. Zachariah, Chair
Professor Gregory Jackson
Professor Howard Milchberg
Professor Bryan Eichhorn
Professor Robert Walker

Dedication

This work is dedicated to my parents and my family

Acknowledgements

I would like to thank many people for their help in making my work here possible, and my life here enjoyable.

First and foremost, I am deeply indebted to my adviser, Dr. Michael Zachariah, for his consistent support throughout the years of my graduate study. He has brought me to the exciting field of nanoparticle research, and sparked my interest in a number of interesting problems. Dr. Zachariah has given me the time for my mind to wonder while his careful guidance, meticulous instructions and invaluable encouragements has ensured I stay on track. His advice in both research and life has been one of my most valuable assets throughout my life, I am grateful for everything professor Zachariah has done for me from the bottom of my heart.

I would also like to express my gratitude to Professor Gregory Jackson, Professor Bryan Eichhorn and Professor Robert Walker for serving on my advisory committee and all the professors who have helped me with my research and study. I must particularly thank Professor Howard Milchberg for being my Ph.D committee member and for his many wonderful insights and helpful suggestions on my research. He developed the entire hydrodynamic code which is the most critical element in my work on understanding the laser particle interaction, and I would not be able to accomplish the project without his support. I also offer my sincere gratitude to the chair of Chemical Physics Program, Professor Michael Coplan, his advice and experience has been of enormously value to me.

I would like to thank Dr. Kihong Park, who was post-doctoral researcher in our lab, and mentor during my first year of graduate study and research. His

knowledge and experience has been very critical for me in scientific thinking and has led me to the fascinating nanoparticle research. I also thank Dr. Weidong Cui and Dr. Dongguen Lee for the valuable comments and suggestions, which has greatly increased my understanding of mass spectrometry.

I must also thank all of my friends especially all of my colleagues in our group, with whom I have had a number of conversations, both on personal and professional levels. My time here in Maryland would have been much more difficult without their friendship. Special thanks go to Dr. Ashish Rai, Dr. De-hao Tsai, Xiaofei Ma, Kyle Sullivan, Nicholas Piekiel, Snehaunshu Chowdbury and Pedro Bueno, with whom I have had the great pleasure of collaborative work. Our time working together was and continues to be a source of great inspiration for me. Thank you all for your help.

Upon finishing my Ph.D. study, I am grateful for my parents and my family. I can never have made it to this point without their support. They provide me extensive educational opportunities, taught me invaluable lessons and even when I am at the other side of the world, their love and support is always with me. I would also like to thanks Jie Chen for her continuous support, thank you for being here.

Finally, I wish to acknowledge the funding support from the Army Research Office and the Defense Threat Reduction Agency.

Table of Contents

List of Tables

Chapter 2

Chapter 3

Chapter 4

Chapter 5

List of Figures

Chapter 1

Chapter 2

Chapter 3

Chapter 4

Chapter 5

Chapter 6

Chapter 7

List of Abbreviations

SEM	Scanning Electron Microscopy
XPS	X-ray Photoelectron Spectroscopy
TG	Thermogravimetry
DTA	Differential Thermal Analysis
MIC	Metastable Intermolecular Composites
DSC	Digital Scanning Calorimetry
DMA	Differential Mobility Analyzer
AMP	Aerosol Particle Mass Analyzer
SPMS	Single Particle Mass Spectrometry
TEM	Transmission Electron Microscopy
MCP	Microchannel Plates
TOF	Time of Flight
EI	Electron Ionization
T-Jump	Temperature Jump
TOFMS	Time-of-Flight Mass Spectrometer
FTIR	Fourier Transform Infrared Spectroscopy
MALDI	Matrix-Assisted Laser Desorption/Ionization
PMT	Photomultiplier Tube

Chapter 1

Introduction

1.1 Aerosols and Nanoparticles

Aerosols are suspensions of solid or liquid particles in a gas phase medium, they are ubiquitous throughout the atmosphere.[1, 2] Dust, smoke, fume, mist and haze are all examples of aerosol phenomena. The field of aerosols research is broad, encompassing many physical/chemical studies, from the understanding of behavior and properties of aerosols to the application of this knowledge to solve practical problems. Aerosol science is highly interdisciplinary in many respects, it links physics, chemistry, biology, materials science, and several other disciplines. Its fields of interest are diverse, on one hand aerosols are considered as undesirable or "bad aerosols" in the field such as environmental pollution, human health or contamination control. On the other hand, aerosols can also be "good aerosols" and serve as building blocks of new materials. Despite the distinct natures of these areas, the fundamental physical principals of aerosols remain the same, aerosol technology can serve as a bridge between different fields and solve problems using similar theoretical concepts and experimental techniques.

Aerosols can be classified in many ways depending on their physical states, chemical compositions or the sources of generation. However, it is the dimension of aerosol systems that makes them interesting and unique. Aerosol systems cover particles of a wide range of sizes, from coarse particles up to millimeter range to ultrafine particles down to nanometer range. Furthermore, since the aerosols are two

phase systems, which include the particles and the gas medium, the interaction of gas medium and particles occurs in the phase boundary of molecular dimension. Therefore, the scope of aerosol studies varies from microscale phenomena to macroscopic systems. Over such a broad dimension, not only the properties and behavior of aerosols can change drastically, the fundamental physics laws that governing these properties also alter with particle size. In particular, aerosols of diameter ~100 nm or smaller, which are usually referred as nanoparticles or ultrafine, have received considerable interest lately due to their unique behaviors and properties. It is in this size range that aerosols science and nanotechnology meet. Nanotechnology is new, popular concept that focuses on manipulating matters in atomic or molecular level for developing nano-scaled materials and devices. The scope of nanotechnology is extremely diverse and interdisciplinary, including many research activities which the characteristic dimension is in the orders of hundreds nanometers or less, and the advance of nanotechnology will likely to have significant impact on many aspects of science and engineering.

Nanoparticles, along with many other nanostructures such as nanowires or nanorods, are primary targets of nanotechnology research. Nanoparticles are in a unique position that bridge bulk materials and isolated atoms or molecules. The physical/chemical properties of a bulk material should have little to do with their size, however, as the dimension approaching to nano-scale, the properties of materials often become strongly size dependent and many interesting or sometimes unexpected behaviors can be observed. For instance, the reactivity of a piece of aluminum metal is stable but can be turned to aggressive combustion in case of aluminum

nanoparticles. The research of nanoparticle is then to explore and understand the strong size dependence of the physical and chemical properties of these particles.

The many interesting behaviors or properties that nanoparticles exhibit can be contributed to nanoparticle's enhanced surface area to volume ratio. It is self-evident that smaller the particle size, the higher the surface area will be for a sample powder of given mass, and as the percentage of atoms at the surface of a material increases, the surface effects become dominated. Moreover, the high specific surface area offers enormous advantages for diffusion, which can significantly alter the reactivity of nanoparticles.

The strong size-dependent properties of nanoparticles give opportunities for creating entirely new class of materials or devices by controlling the size and structure of nanoparticles. However, it is the very same reason make the nanoparticles research a challenging task. As the nanotechnology progresses, researches are continuously discovering new materials and new material classes, the development of appropriate characterization tools and methods becomes critical for nanoparticles study. Many conventional techniques and methods for charactering bulk materials have been extended to characterize nanoparticles, such as scanning electron microscopy (SEM), x-ray photoelectron spectroscopy (XPS), thermogravimetry (TG) or differential thermal analysis (DTA). Generally those methods require a filter or substrate to collect a sample, as well as subsequently performing off-line analysis. However, the physical and chemical characteristic of nanoparticles may change over a short time interval, which makes sample introduction techniques crucial in nanoparticle analysis. Furthermore, conventional methods suffer from contamination

and alteration of the sample, for instance, evaporation of a volatile species can change the collected particles before analysis.[3] In addition, the experimental uncertainties associated with mass/heat transfer effects within the bulk sample make the condensed-phase reaction characterization of nanoparticles difficult.[4-6] These significant drawbacks greatly limited our capability for probing the intrinsic reactivity and properties of nanoparticles.

With this in mind, one would like to have methods to explore the intrinsic properties of nanoparticles in a size-resolved, real-time manner, and that where the aerosols technology back to our attention. Many aerosol concepts emphasis a microscopic approach to understand the properties and behaviors of individual particle, and the objective of this thesis is to employ these aerosol concepts to develop tools and methods for probing the intrinsic properties of nanoparticles. In addition, a novel approach to probe particle-particle reaction is also developed. The tools and methods developed here would be insightful complements to conventional analysis methods and can certainly benefit our understanding on the fundamental natures of nanoparticles.

The scope of this thesis is focused on the study of reactivity of nanoparticles and their applications in energetic materials using the new developed approaches. However, we would like to point out that the methods developed here are generic, and can be applied to many other nano-material related studies.

1.2 Energetic Materials

Energetic materials, such as explosives, pyrotechnics, and propellants, are classes of materials that can release large amounts of chemical energy upon reaction.

The goal of energetic materials research is to exploit low cost and environmental friendly energetic materials with high stability and high performance. There has been significant research effort directed to energetic materials, ranging from synthesis of new chemical formulations to the development of theoretical models and experimental techniques for materials characterization. And the recent interest in this field is primarily focused on finding advanced materials with enhanced reactivity, reduced sensitivity and tunable energy release for intended applications.

In general, energetic materials can be considered as mixing of fuels and oxidizers. Depending on how the fuels and oxidizers mixed, energetic materials can be either chemically pure compounds where fuels and oxidizers are intimately incorporated into one molecular, or composite materials that are mixtures of separate fuels and oxidizers. Traditionally, monomolecular based energetic materials, such as TNT, RDX, HMX, or CL-20, have been popular choices for many military and civil applications. The advantage of these materials is that the fuels and oxidizers are mixed at atomic level, therefore the mass transport processes can be minimized as the chemical reaction are intramolecular reactions, and the reaction rate is primarily controlled by chemical kinetics. As the result, the exothermic reactions of monomolecular based energetic materials have a rapid energy release rate. However, in term of total available energy, monomolecular based energetic materials have a poor performance and the low energy density greatly limited their applications.

In contrast to monomolecular based energetic materials, composite energetic materials have significantly higher energy densities, and have received great attention because of this reason. In particular, metal based composite energetic materials, also

known as thermites, have been a field of intense research in last decades. A thermite reaction is highly exothermic which involves mixture of a metallic fuel and a metal oxide as oxidizer, as show below

$$M_1 + M_2O \rightarrow M_1O + M_2 + \Delta H \quad (1.1)$$

Here M_1 is the metal fuel while M_2O is the metal oxide and the reaction results in a release of energy ΔH. In principal, any reactive metal can be used as the fuel, but aluminum is by far the common choice because its low cost and high enthalpy of combustion (-1676 KJ/mol).[7, 8] The energy density is defined as the energy release ΔH per unit volume or unit mass. Figure 1.1 shows the energy density of some typical thermite mixtures compare to commonly used monomolecular based energetic materials, and it clearly shows that those thermite mixtures significantly outperform the traditional organic energetic materials in term of total available energy.[9] On the other hand, since the fuel and oxidizer in thermites are not as intimately mixed as monomolecular materials, the thermites then undergo bi-molecular reactions which are primarily controlled by the mass transport of the diffusion process. In another word, the overall reaction rate is significantly slower than monomolecular materials and the low energy release rate of these composite materials greatly limited their use toward certain applications.

One of the exciting developments of nanoparticles is their application toward energetic materials. In recent years, nanocomposite thermites, also known as Metastable Intermolecular Composites (MIC), have been developed by using metal based nanoparticle as reactive components and have attracted great attentions because of their enhanced energy release rate.[10-12] In nanocomposite thermites, the reactive

components are mixed at the nano-scale so that diffusion length can be greatly reduced and the surface area can be increased. As a result nanostructured particles have a much higher reactivity than their corresponding micron sized cousins. Aside from the fast reaction rate, the unique nanostructure of MICs also allows a control over the reactivity by varying parameters such as particle size, morphology and local composition.[13-15]

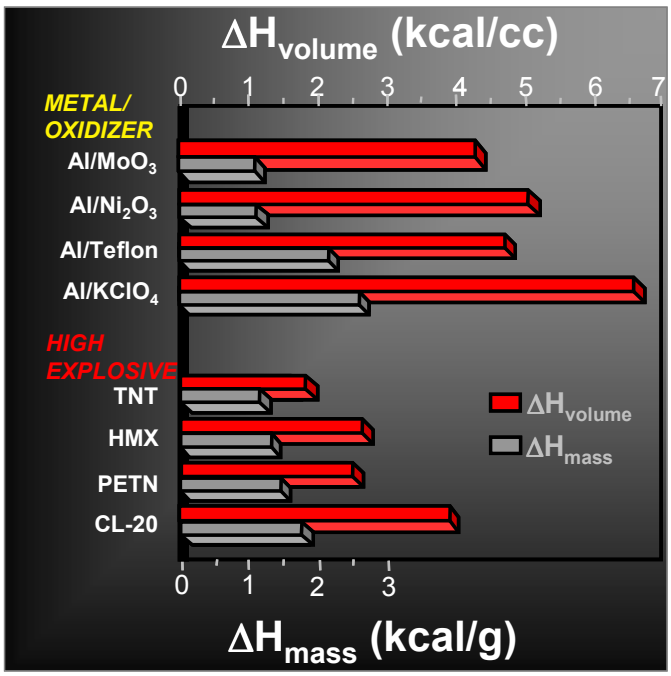

Figure 1.1 Energy density of commonly used monomolecular based energetic materials and metal based composite energetic materials

Because these classes of material are relatively new they have not been studied as extensively as traditional monomolecular based or composite based energetic materials. Not surprisingly diagnostic tools have not been developed to study dome of the unique features of this class of materials either. Studies of thermite energetic materials are very difficult due to their fast and intense reaction, and the

relatively low gas production. Measurement of combustion properties such as flame speed, burn rate, or ignition temperatures are typical methods to characterize thermite reactions.[11, 12, 16-21] The reaction mechanism is often studied with traditional thermal analysis techniques such as thermogravimetric analysis (TGA), differential thermal analysis (DTA) or digital scanning calorimetry (DSC). With the help of electron microscopy and X-ray diffraction, reaction products and detailed reaction kinetics at slow heating can be revealed.[22-24] While experimental data obtained from low heating rate conditions can be extrapolated to the high heating regime, it has been shown that heating rate has an effect on the reaction process.[22, 23, 25] Reaction pathways or mechanisms can change drastically from a slow heating process to a fast heating process, therefore, it is preferred to conduct experiments under high heating rates. Furthermore, most of experimental techniques discussed here are measurements of bulk samples instead of intrinsic reactivity of nanoparticles.

1.3 Scope of the Thesis

As the science of nanotechnology progresses, researches are continuously discovering new materials and material classes for which we need improved methods and tools for probing their intrinsic reactivity and properties. As discussed in the previous sections, aerosol based concepts and techniques are ideal for such applications and may offer certain advantages over conventional methods. The objective of this work is to employ aerosol based concepts and techniques to study the reactivity of nanoparticles and nanocomposites. This thesis can be categorized in two ways. First, to provide knowledge of just how reactive a material is, we develop methods to probe the intrinsic size-dependent reactivity of individual metal particles.

And second, the development of measurement tools to study particle-particle reaction, and probe the reactivity of nanocomposite materials under combustion-like condition.

Chapter 2 describe a new method that combines two ion-mobility spectrometry approaches, tandem differential mobility analysis (TDMA)[26, 27] and tandem differential mobility – particle mass analysis (DMA-APM)[28, 29] to probe the size resolved reactivity of nanoparticles. Using this method, we conducted on-the-fly investigations on the oxidation kinetics of nickel nanoparticles to evaluate their potential use as a fuel in energetic materials. Nickel nanoparticles were generated in-situ using gas-phase thermal pyrolysis of nickel carbonyl. Four particle sizes (40, 62, 81 and 96 nm, mobility size) were then selected by using a differential mobility analyzer. These particles were sequentially oxidized in a flow reactor at various temperatures (25-1100 °C). The size and mass change of the size selected and reacted particles were then measured by a second DMA, or an APM. We found that both particle size and mass were increased as the temperature increased. However, at higher temperature (600-1100°C), a different mass and size change behavior was observed which could attribute to a phase transition between NiO and Ni_2O_3. A shrinking core model employed to extract the size- resolved kinetic parameters shows that the activation energy for oxidation decreased with decreasing particle size The burning time power dependence on particle size was found to be less than 2 and nickel particles were found to be kinetically more active than aluminum.

Real-time Single Particle Mass Spectrometry (SPMS)[3, 5, 30] has been a powerful tool due to its ability to obtain qualitative and quantitative characteristic of a single particle. There has been significant progress on quantitatively determining

particle size and composition with SPMS using the laser ablation/ionization technique.[3, 5, 30-35] Recently, this method was also employed to study size-resolved reactivity of aluminum nanoparticles.[4] Chapter 3 and 4 will focus exclusively on the development and improvement of this technique, including both theoretical modeling work and experimental characterization on the quantification of particle size and composition with SPMS.

Understanding the characteristic behavior of ions produced from the interaction of a high energy laser pulse with nanoparticles is essential for quantitative determination of composition and size of nanoparticles from single particle mass spectrometry. In chapter 3, we employed a one-dimensional hydrodynamic model,[36] where the laser field is coupled to the non-equilibrium time-dependent plasma hydrodynamics of the heated particles. We focus on regimes of laser width from 0.01 ns to 10 ns (532 nm wavelength, 100mJ/pulse) and particle size (20 - 400 nm in diameter) most relevant to commonly used SPMS, and determine the properties of ions generated during the interaction with a strong laser pulse. We compare the simulation results with experiments conducted on aluminum nanoparticles.

The laser-particle interaction is separated into a “soft heating” regime followed by a hydrodynamic expansion. Simulation results showed that the ablation/ionization is effectively complete well before the laser ever reaches its peak intensity. As the pulse width decreased for a given pulse energy, the kinetic energy of ions increased, suggesting that too short a pulse laser (i.e., high laser intensity) would be undesirable because higher energetic ions lead to lower detection efficiency in the SPMS. Results also show that for particle sizes in the range of 100 nm ~ 400 nm, as

particle size increased, the kinetic energy of ions produced from the particle increased with a power law relationship, consistent with experiment. Lastly our simulations indicated that ions from the surface of the particle are of higher energy, and therefore have lower detection efficiency.

With the complete ionization technique, quantitative information about particle size and elemental stoichiometry for a single component particle can be obtained. However, it is more complex to deal with multi-component composite particles. The morphology and the composition of particles will change the thermal and optical properties of the particle and thus the laser-particle interaction. In chapter 4, multi-component particles of different morphologies are generated and used to examine the limitations of the complete ionization approach. The experimental results show that there are component and morphology biases which can be related to the high nonlinear properties of the laser-particle interaction. The relative laser absorptivity of each component is found to have a significant impact on the particle heating and ion formation process. In addition, the ion distribution formed from the laser-particle interaction is in part a result of charge transfer, and electron-ion recombination. A qualitative explanation for the observed behavior is developed, which involves the characteristic time for laser heating and intraparticle heat conduction.

In chapter 5, we turn our attention to the reactivity of composite materials. A new T-Jump/time-of-flight mass spectrometer for time-resolved analysis of rapid pyrolysis chemistry of solids and liquids, with a focus on energetic materials, was developed. The instrument employs a thin wire substrate which can be coated with

the material of interest, and can be rapidly heated (10^6 K/s). The T-Jump probe is inserted with the extraction region of a linear-TOF, which enables multiple spectra to be obtained during a single reaction event. By monitoring the electrical characteristics of the heated wire, the temperature could also be obtained and correlated to the mass-spectra. As example, we present time-resolved spectra for the ignition of nitrocellulose and RDX. The fidelity of the instrument is demonstrated in the spectra presented which show the temporal formation and decay of several species in both systems. A simultaneous measurement of temperature enables us to extract the ignition temperature and the characteristic reaction time. The time resolved mass spectra obtained show that these solid energetic material reactions, under a rapid heating rate, can occur on a time scale of milliseconds or less. While the data sampling rate of 10000 Hz were used in the present experiments, the instrument is capable of a maximum scanning rate of up to ~30 kHz. The capability of high speed time resolved measurements offers an additional analytical tool for characterization of the decomposition, ignition, and combustion of energetic materials

In chapter 6, heterogeneous nanocomposite thermite reactions in Al/CuO and Al/Fe_2O_3 systems were investigated using the T-Jump/TOF mass spectrometer. Ignition experiments with time-resolved mass spectrometric measurement of reaction species were performed at heating rate in the range of ~10^4 K/s to ~10^6 K/s. As a complement of T-Jump/mass spectrometry method, optical emission measurement were also conducted and compared with time-resolved mass spectra signal. Species of Al, Al_2O, and Cu/Fe species were identified in mass spectra as reaction products, and O_2 species which released from decomposition of oxidizer particles was also

observed during the course of the thermite reactions. A heat transfer model was also developed to determine the onsite temperature of thermite powders. Based on this model, the ignition temperatures for Al/CuO and Al/Fe_2O_3 systems were obtained as function of heating rate from our experimental data. The mass spectra analysis and ignition temperature data suggest that the formation of oxygen from oxidizer particles may be the important factor for reaction of nanocomposite thermite mixtures for the heating rates investigated in this work. The metal oxide particles behave as an oxygen storage device in the thermite mixture, and can release oxygen very fast to initiate the reaction. The role of oxygen specie is not only an oxidizer but also an energy propagation media that carries heat to neighboring particles. We also compared the experimental observation with prediction from thermal equilibrium calculation, the results suggest the species distribution of observed in T-jump experiments are in a highly non-equilibrium state.

Chapter 2

Size Resolved Measurements of the Reactivity of Metal Nanoparticles: Nickel nanoparticle Oxidation Kinetics

2.1 Introduction

Recent advancement in so called "nanoenergetic" materials are focused on either enhancing or tuning reactivity. On one level this issues reduces to a length-scale argument, whereby smaller fuel/oxidizer combinations result in smaller diffusion lengths and therefore higher reactivity. On another level, this discussion leads to choices of different thermite formulation. Although there have been considerable successes in enhancing the energy release rate of thermite systems, the goal of tuning the reactivity is still a subject for further research. In one of previous works, our group reported a method to control the energy release rate of energetic nanoparticles by creation of a core shell nanostructure on the oxidizer particle.[15] Similarly, the reactivity of nanoenergetic material can also be controlled by modifying the structure of the aluminum fuel.[37] More recently we have seen that mixtures of nanoaluminum and nanoboron outperform either material on their own.[14] Those results suggest both material choices (e.g. Ni, Ti, etc.) and nanoarchitecture as means to tune the energy release profiles of materials beyond aluminum. The application of those materials would take the form of composite materials e.g. Al/Ni alloy, or metal particles with a different morphology such as aluminum core with nickel coating.

While considerable opportunity exists for improvements, in actuality very little attention has been paid to the kinetics of reactivity of small metal particles beyond nanoaluminum. The oxidation of metal in form of bulk sample or thin films has been studied for over a century,[38-60] however, there are only a few studies on the oxidation of metal nanoparticles.[39, 61-65] Carter developed a solid state kinetic model based on a diffusion controlled mechanism, for oxidation of ~100 micron particles using a microbalance.[55] Fromhold obtained the same oxidation rate law using a coupled current approach with the assumption of zero space charge.[40] Karmhag and Niklasson explored the oxidation kinetics of micron size nickel particles using thermogravimetric measurements, and obtained a lower activation energy than bulk nickel.[64, 65] As particle size decreases into the nano-scale, the mass transfer limitations should be reduced and we should expect to see an enhancement in reactivity. Previous work from our group on the oxidation of nanoaluminum particles shows that both the overall rate constant and activation energy are size dependent.[4, 28] Karmhag et al. studied the oxidation of nano sized nickel particles at low temperatures (135^{o}C-235^{o}C) using thermogravimetric measurements, and suggested that nonlinear diffusion resulting from space and local charging occurs in this case, and results in a higher rate constant and lower activation energy.[62] The same group also probed the size dependent oxidation kinetics, and found that the rate constant roughly goes as the square of the inverse of particle diameter.[63] They further proposed a phenomenological model to consider the nonlinear effect in oxidation of nano scaled particles.[61]

All the above studies were carried out using conventional dynamic thermal techniques such as thermogravimetry. It is well known that those methods are greatly influenced by heat and mass transfer effects such that the results are biased by experimental artifacts.[4-6] In this chapter, we present the application of aerosol based ion-mobility spectrometry for the study on the reactivity of metal nanoparticles. Our previous results on the study the solid-gas phase reaction kinetics show that the reaction rate obtained using aerosol based techniques, are much higher than conventional methods, which may represent the intrinsic reactivity of nanoparticles.[4, 5] The method developed here provides a generic approach for characterizing the intrinsic properties of nanoparticles. This chapter illustrates the application of this approach toward the characterization of nickel nanoparticle oxidation kinetics, and this work was done along with Dr. Ashish Rai, Nicholas Piekiel, and Xiaofei Ma, and it has been published by our group.[66]

The basic idea of the experimental approach is to prepare Ni particles of characterized size/shape (i.e. Monodisperse), and monitor changes during oxidation in free-flight (i.e. no substrate). This study consists of two experiments, both of which rely on ion-mobility separation. A Tandem Differential Mobility Analyzer (DMA) system[26, 27, 67] is used to measure the size change after oxidation, while the mass change is tracked by a DMA-APM (Aerosol Particle Mass Analyzer) system.[28, 29, 68, 69] The mass and size changes of nanoparticles are studied from room temperature to 1100 ^{o}C. The average density obtained from mass and size measurements show the nickel nanoparticle oxidation process can be correlated to the formation of both NiO and Ni_2O_3 ($4Ni+3O_2 \rightarrow 2Ni_2O_3$, $2Ni+O_2 \rightarrow 2NiO$) and a phase

change region where both the oxidation of nickel and thermal decomposition of Ni_2O_3 to NiO ($2Ni_2O_3$->$4NiO+O_2$) occur simultaneously. The reaction rates were then extracted from the experiment data as a function of particle size.

2.2 Experimental Approach

The experiment system consists of three components. Preparation of monodisperse nickel particles, second, exposure of size selected nickel particles into a controlled oxidation region, and third, measurement of the size and mass change resulting from reaction. A complete schematic of the experimental setup with temperature and flow rate control is shown in Figure 2.1.

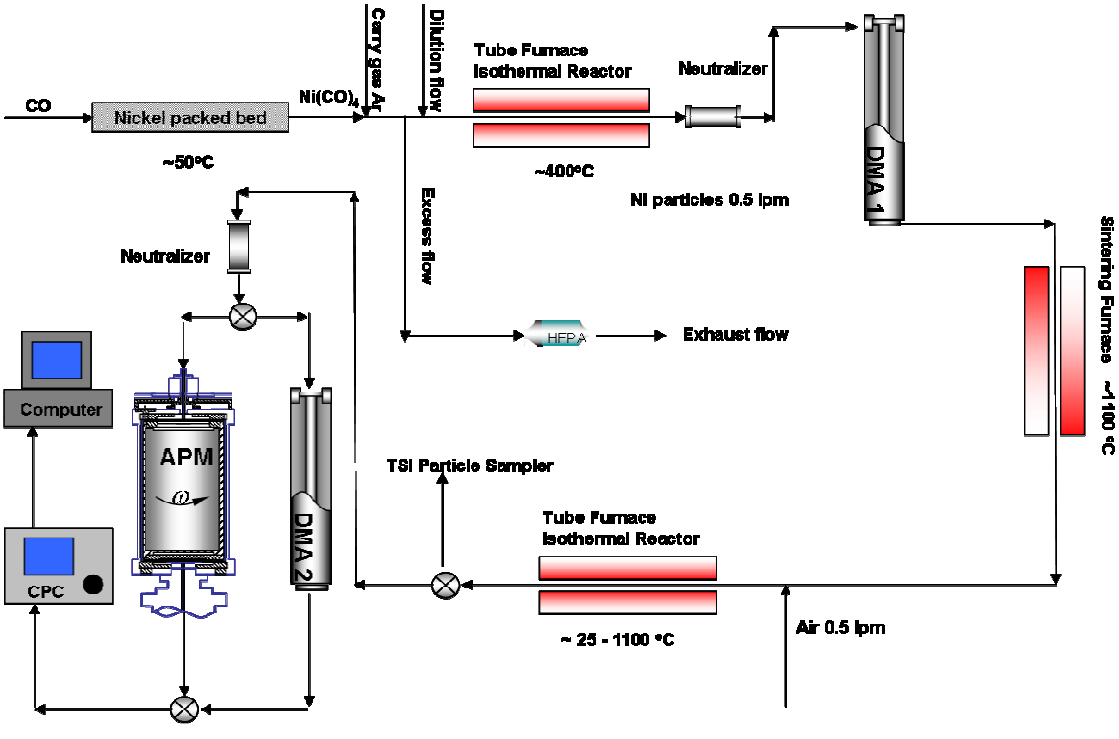

Figure 2.1: Schematic of Ni generation and oxidation experiment.

2.2.1 In-situ Generation of Nickel Nanoparticles

In this work, high purity nickel nanoparticles was prepared in an oxygen free environment using gas-phase thermal pyrolysis of nickel carbonyl.[70, 71] Because of the high toxicity of nickel carbonyl, it was generated in-situ by flowing of a small amount of carbon monoxide (99.5%) through a nickel powder bed (3 um, 99.7% Sigma Aldrich), which was placed immediately upstream of an isothermal tube reactor to thermally decompose $Ni(CO)_4$ so as to form nickel particles as shown in Figure 2.1. Before each experiment, the nickel bed was heated to ~350^oC with a hydrogen flow (99.5%) for about 4 hours to clean the surface of the nickel powder. After the hydrogen pre-treatment, activated nickel powder is reacted with CO at ~50^oC to generate $Ni(CO)_4$. The generated $Ni(CO)_4$ was mixed with a flow of Ar (industrial grade) and passed to the cracking reactor held at ~400^oC, to create nickel particles ($Ni(CO)_4$->Ni + 4CO). Since the resulting particles are agglomerated and our experimental protocol requires individual primary particles, the generated nickel particles were size selected by the first DMA (to be described below), and subsequently heated to 1100^oC to form spherical particles, so as to prepare monodisperse particles for the oxidation step.

2.2.2 Differential Mobility Analyzer (DMA) and Aerosol Particle Mass Analyzer (APM)

The primary analytical tools employed in the experiments were a tandem differential mobility analyzer system (TDMA)[26, 27, 67, 72, 73] and DMA-APM (aerosol particle mass analyzer) systems.[28, 29, 68, 69] In these experiments, particles were first charged with a Boltzmann charge distribution by exposing the

aerosol to a Po-210 source, before the first DMA. The average charge state of sample particles under Boltzmann distribution is roughly neutral, with most of particles uncharged and equal amount of particles carry +/- 1 charge and +/-2 charges, etc. For example, in case of 50 nm particles, 60.2% particles will be neutral, 19.3% carry +/-1 charge, 0.6% carry +/- 2 charges, and higher charge state would be even less.[2] Considering the small percentage in the multiple charged states, we ignore multiple charged particles and assume the charged particles are all singly charged. Both the DMA and APM are configured to classify positively charge particles for these experiments.

The TDMA system setup was similar to that in our previous work.[26, 67, 72, 73] The DMA consists of an annular region between two concentric cylinders, with the center cylinder held at high voltage and the outer one at ground. The schematic of DMA is shown in Figure 2.2 (a), when charged particles flow between the cylinders the electric force on the particle is balanced by the drag force, the balance of two opposite forces result a constant drifting velocity at the radial direction. The electrical mobility, Z, of a single charged particle is given by[1]

$$Z = \frac{V_r}{E} = \frac{eC_c}{3\pi\eta D_p} \tag{2.1}$$

where V_r is particle radial velocity, E is the electric field, e is charge on the particle, D_p is particle diameter, η is the viscosity of carry gas and C_c is the slip correction factor given by

$$C_c = 1 + \frac{2\lambda}{D_p}\left[A_1 + A_2 \exp\frac{-A_3 D_p}{\lambda}\right] \tag{2.2}$$

here λ is the mean free path of the gas molecules and A_1, A_2, A_3 are constants based on experimental measurements.[1] Since the particle mobility is size dependent, particles of small size (trajectory 1) and large size (trajectory 2) have different trajectories as shown in Figure 2.2 (a). At a fixed voltage, we obtain particles of same mobility size exiting the instrument (trajectory 3). As shown in Figure 2.1, DMA-1 is used to selecting particles all with the same electrical mobility size and functions as a source of mono-area particles.[74] However, since DMA-1 selected particles are aggregates, a sintering furnace was placed after DMA-1 to form individual spherical particles for the oxidation step. A second DMA was operated in voltage-step mode with a condensation particle counter (CPC) as a particle size distribution measurement tool to track the size change after the reaction process. A second Po-210 neutralizer was placed between the reactor, and DMA-2 to re-charge the particles. This was necessary as the high temperature treatment (sintering or high oxidation temperatures) would cause the particles to lose charge. In summary the TDMA experiment tracks changes in physical size as a result of oxidation.

In a parallel experiment the change in particle mass after oxidation was measured by an aerosol particle mass analyzer (APM) coupled with a CPC. The APM is a relatively new technique that can determine the particle mass distribution based on particle mass to charge ratio.[29] The schematic of AMP is shown in Figure 2.2 (b), it consists of two concentric cylindrical electrodes that rotate together at a controlled speed. An electrical field is created by applying high voltage on the inner electrode while the outer one is held at ground. Charged particles flowing within the concentric cylinders experience opposing centrifugal and electrostatic forces as

shown in Figure 2.2 (b) and particles exiting the instrument at fixed voltage and rotation speed all have the same nominal mass:

$$m = \frac{eE_{APM}}{r\omega^2} \tag{2.3}$$

Here E_{APM} is the electrical field between the two cylinders, ω is APM rotation speed and r is the distance between particle and the center of the cylinders. By scanning either the voltage or the rotation speed, the particle mass distribution (independent of particle shape) can be determined. Our previous experiments have used the DMA-APM technique to measure the inherent density of nanoparticles, as well as to study the mechanism of aluminum oxidation.[28, 68]

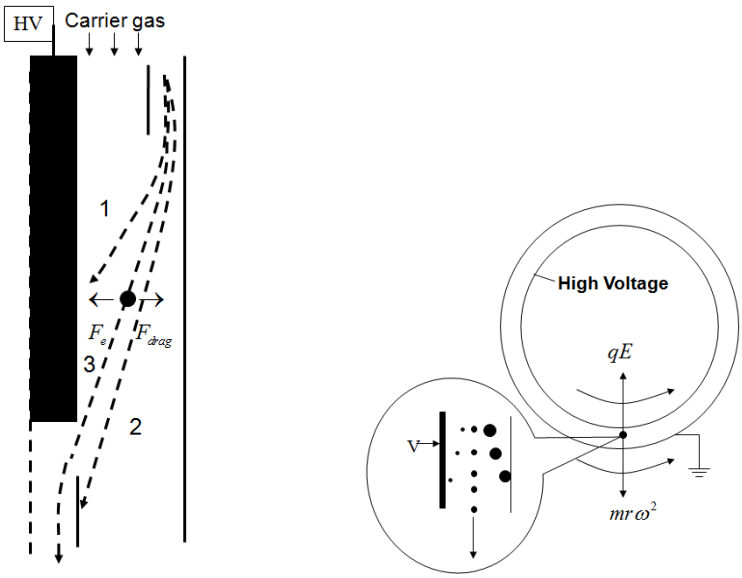

(a) (b)

Figure 2.2 Schematic of (a) DMA, and (b) APM

Before the oxidation study, the DMA and APM were first calibrated using the NIST standard PSL particles. The PSL particles have a nominal size of 100.7 nm and the DMA measured size distribution suggest a peak size of 105.1 nm as shown in figure 2.3 (a). Known the particles density, the APM measured mass distribution can be converted to size distribution and is shown in figure 2.3 (b). The APM measured a peak particle size of 105.8 nm, agree with the DMA result well. On the basis of operating conditions for the DMA and APM we estimate uncertainties as follows. For the DMA operating conditions the uncertainty is based on the theoretical transfer function, which will give an uncertainly in the peak particle size of ±4%. We then use Gaussian fit to determine the peak size, which would have a precision uncertainty of no more than 1%. A similar result can be obtained for the APM; however, the uncertainties are not due to the transfer function but uncertainties in the step voltage, which has a resolution of only ±0.5 V, which gives an uncertainty in mass of ~4%. Using the root-sum-square (RSS) method, we can estimate the uncertainty of density calculation at ~5%. This is consistent with prior work (unpublished) using combined DMA/APM on reference aerosols (NaCl and DOP) which gave an experimentally determined uncertainly in density of 4%.

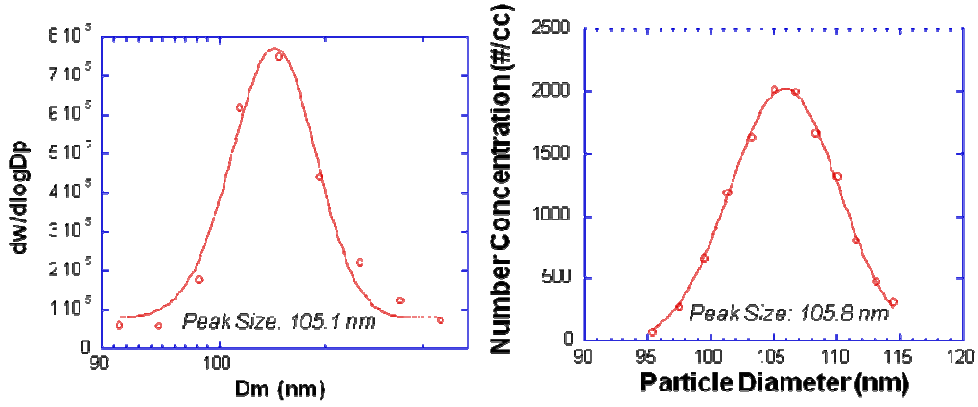

(a) (b)

Figure 2.3 PSL particle size distribution measured by (a) DMA and (b) APM assuming the density of PSL is 1.05 g/cc

2.2.3 Nickel Nanoparticles Characterization, Sampling and Oxidation

In this study, nickel nanoparticles with mobility sizes of 70, 135, 200 and 240 nm were selected using the first DMA. To successfully measure the size and mass change resulting from oxidation using Tandem DMA and DMA-APM system, the particle number concentration in the selected size range must be tuned. This is accomplished by varying the concentration of $Ni(CO)_4$, in the various dilution steps used. The Ar carrier gas flow varied from 2 LPM (Liter Per Minute) to 10 LPM, and the dilution Ar flow varied from 0.2 LPM to 0.45 LPM. Figure 2.4 shows an example size distribution taken before the sintering furnace. The system in this case was tuned to create a peak mobility size of about 120 nm, with sufficient particles for further measurement at the size range from 70 to 240 nm.

Size selected nickel particles coming from DMA-1 were subsequently sintered at 1100°C to form monodisperse spherical particles, whose size and mass can be

measured by DMA-2 and APM, under condition of no-oxidation. The size of particles shrink to a mobility size of 40, 62, 81, and 96 nm after sintering, and are thus the initial particle size before oxidation. The sintered particles were then mixed with dry air with 1:1 ratio, and enter a well characterized tube reactor for oxidation at a controlled temperature (25~1100°C). The oxidation rector consisted of a quartz reactor tube of 1 cm i.d. and 120 cm long with a heated length of 36 cm. The axial temperature profiles along the quartz tube were measured at each selective temperature using a thermocouple, and are shown in Figure 2.5. For the normal operating condition of 1 LPM through the oxidation furnace, the residence time estimated from the measured temperature profiles, give ~1.3 seconds for room temperature to ~0.3 second at 1100°C. A more detailed discussion for the measurement of temperature profile in the tube furnace and calculation of the resident time can be found in our previous work.[26, 73]

Finally the reacted particles are directed to the second DMA, or the APM, for the size and mass measurement. Transmission Electron Microscopy (TEM) was also used to examine the structure of nickel nanoparticles before and after sintering to evaluate the sintering process. An electrostatic precipitator was used after the reaction furnace to collect particles on Formvar coated 200 mesh copper TEM grids. TEM characterization was performed with a Zeiss EM10 TEM (accelerating voltage: 80 kV and magnification: 100x-200000x)

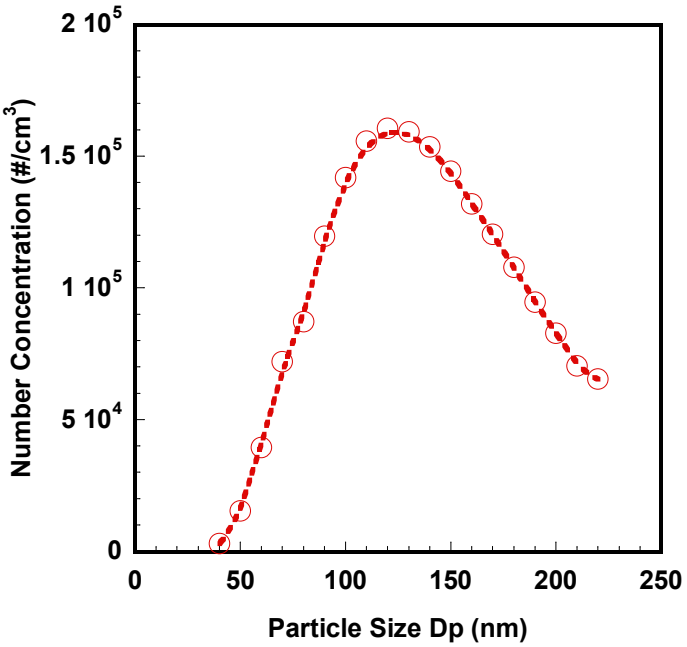

Figure 2.4: Single DMA scan of the overall nickel particle size distribution sampled before sintering. (The circles are the data points and the dash line is the smooth fit to the data).

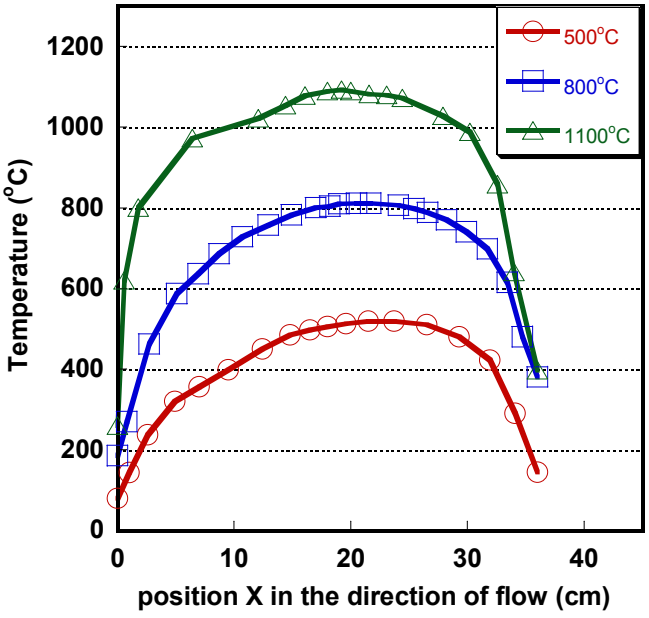

Figure 2.5: Temperature profile within the quartz flow tube for furnace settings of 500°C 800°C and 1100°C.

2.3 Results and Discussion

2.3.1 Size and Mass Measurements of Nickel Nanoparticle Oxidation

The morphology of nickel nanoparticles as they exit the generator are shown in Figure 2.6 (a) and indicate the particles are highly aggregated with primary particles sizes less than 5 nm. At the high oxidation temperatures, oxidation and sintering (which decreases surface area) would occur simultaneously for such small primary particle size, and make the measurements and subsequent data analysis too ambiguous. For this reason we choose to sinter the aggregates to spheres. TEM images of the polydisperse particles sampled after the sintering furnace is shown in Figure 2.6 (b) and confirms that the aggregates were successfully sintered to form spheres. Note that the TEM sample was prepared by sintering polydisperse particles without DMA-1 selection, although the sintering process would result in perfectly spherical particles without any aggregate structure,[75] the high number concentration of generated particles leads to re-aggregation. This re-aggregation can be prevented by first size selecting particles with DMA-1. Mobility sizes of 70, 135, 200 and 240 nm aggregate particles were selected, their size and mass after sintering were subsequently measured using DMA-2 and APM and the results are show in Figure 2.7. The particle sizes shrink to 40, 62, 81, and 96 nm after sintering and the measured mass (APM) and size (DMA) show a relationship of mass $\sim Dp^{3.006}$, implying that individual spherical nickel particles were obtained for the subsequent oxidation step.

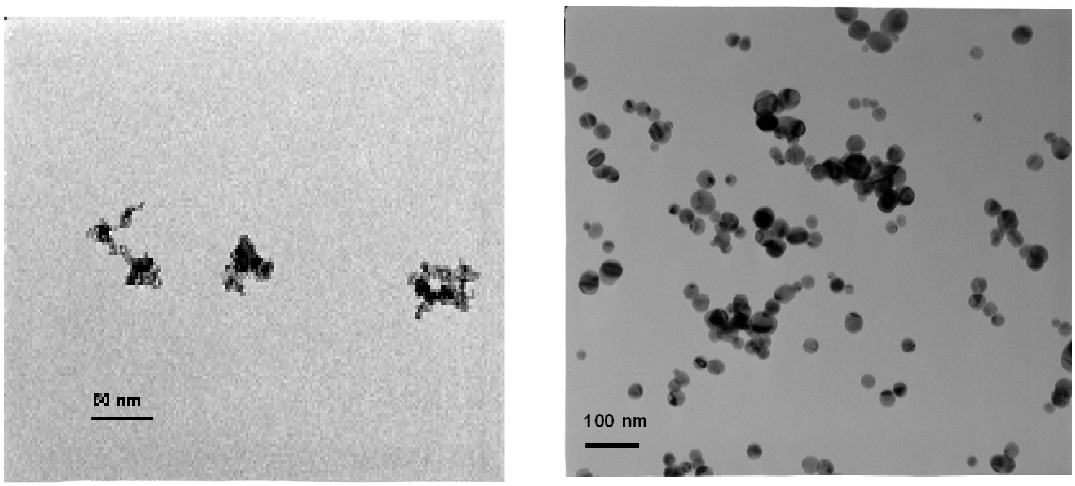

(a) (b)

Figure 2.6 TEM micrographs of Nickel samples: (a) before sintering (b) after sintering

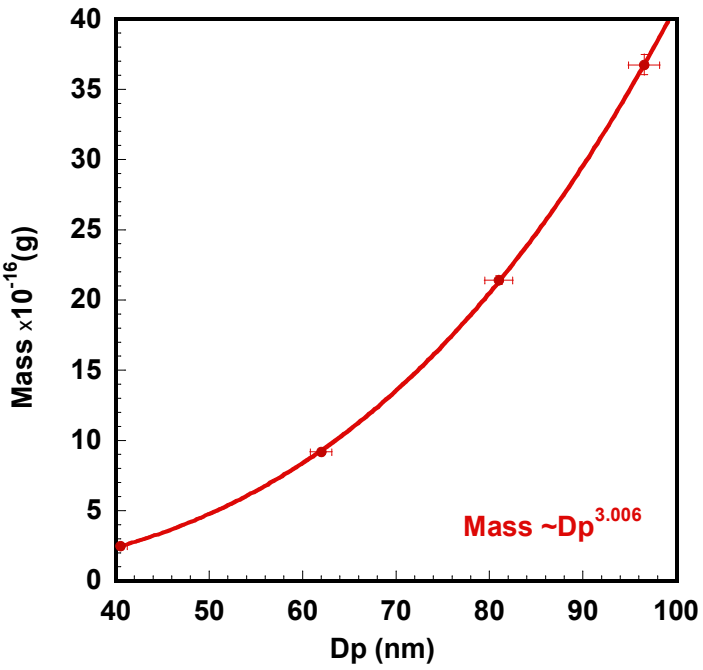

Figure 2.7 APM measured mass (Y axis) and TDMA measured initial particle size (X-axis).

We now turn to the size selected measurements. Mobility size selected Ni particles of 40, 62, 81 and 96 nm (after sintering) were mixed with air and oxidized, following which the size or mass of the reacted particles is measured by a second DMA or APM.

Panels (a), (b), (c) and (d) of Figure 2.8 show normalized particle size distributions measured by DMA-2 at selected furnace temperatures for initial mobility size of 40, 62, 81 and 96 nm, respectively. The size distributions obtained for each furnace temperature were fit to a Gaussian distribution to determine the peak size. As mentioned above, the initial un-reacted particle size is determined from DMA 2 at 25°C. Furthermore measurements of particle oxidation at 200°C show no size change, indicating that reaction if there is any is below our detection limit, which we estimate from prior work to be ~0.3 nm in diameter.

The TDMA experimental results in Figure 2.8 show that the particle size first increases as we increase the furnace temperature, and reach a size maximum at 600°C (for particles with initial size 40 nm), 700°C (for particles with initial size 62 nm and 81 nm) and 800°C (for particles with initial size 96 nm). Further increases in the reaction temperature, result in decreases in particle size as the peak size decreased from a maximum of 51.3 nm to 49 nm, 81.4 nm to 77.5 nm, 106.9 nm to 102.5 nm and 124.8 nm to 121.8 nm, for particles with initial size 40, 62, 81 and 96 nm, respectively. The detailed particle peak size data are shown in Table 2.1, and the size change ΔDp as function of furnace temperature is shown in Figure 2.9.

Table 2.1: Change in particle size as a function of oxidation temperature

Furnace Setting (°C)	particle size (nm)			
	40	62	81	96
25	40.0	62.0	81.0	96.6
200	40.0	62.0	81.0	96.6
300	40.2	62.5	81.3	96.9
400	41.5	63.6	81.8	97.5
500	45.9	67.0	87.1	101.2
600	51.3	77.9	95.8	110.2
700	51.2	81.4	106.9	122.7
800	50.9	81.2	106.9	124.8
900	50.1	80.7	106.5	124.7
1000	49.0	78.7	104.8	123.8
1100	50.3	77.5	102.5	121.8

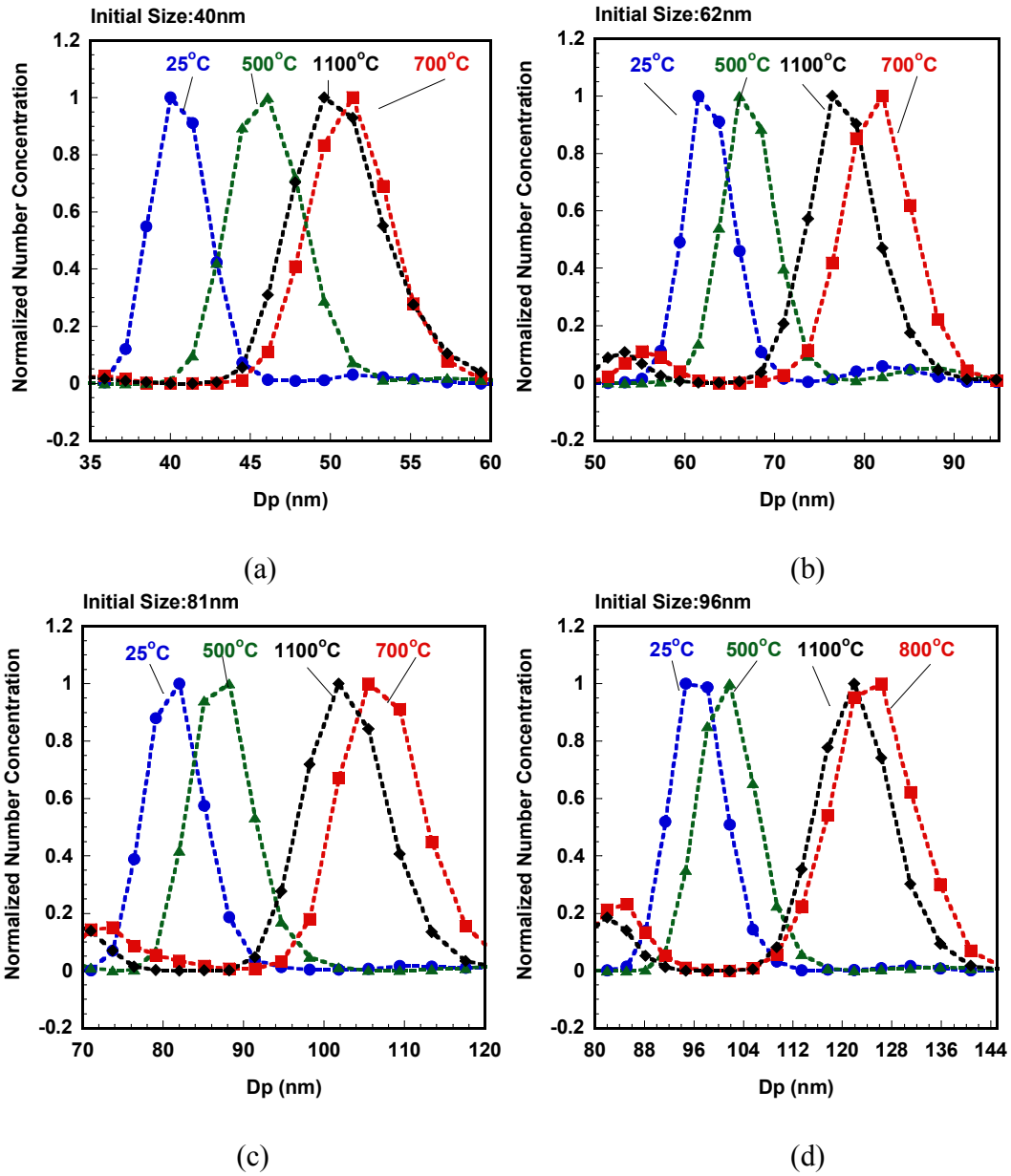

Figure 2.8 TDMA measured size distribution for initial size of (a) 40 nm, (b) 62 nm (c) 81 nm and (d) 96 nm nickel particles at different oxidation temperatures.

The TDMA experiment indicates that the oxidation starts at ~300°C as evidenced by an increase in particle size. This size increase results because nickel oxidation forms a lower density oxide than the zero valent metal. However, the size increase is not continuous in temperature and in the higher temperature regions (above 600°C), a significant size decrease is observed for all particle sizes. There are several possible reasons that can contribute to the shrinkage of particles at high temperatures. First, some particles are not perfectly spherical, and some may be slightly aggregateed, so that one may argue that what was seeing at these temperatures is really sintering or re-arrangement of particle morphology. However, as we have discussed above, this is an unlikely explanation considering the fractal dimension of the particles is ~3 based on the experimental result shown in Figure 2.7. As a result, any size change after particles pass through the oxidation furnace can be attributed solely to oxidation, e.g. not from the re-arrangement of particle morphology.

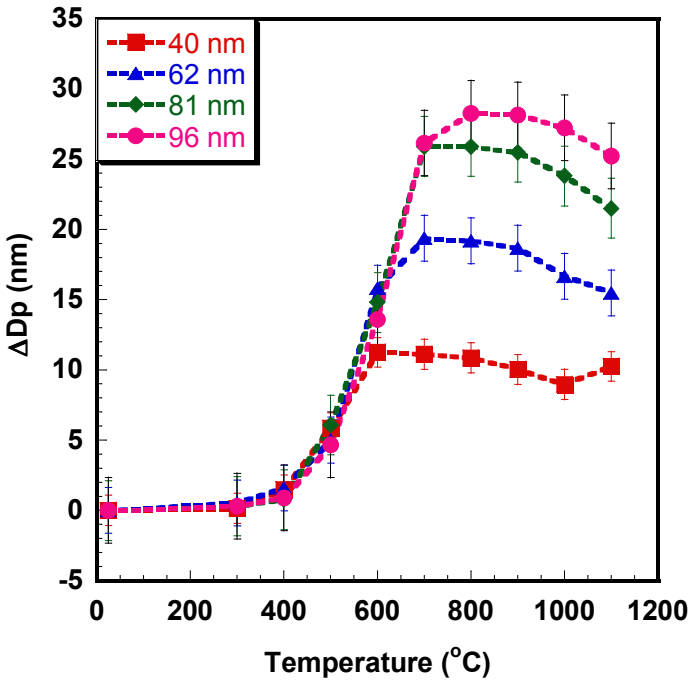

Figure 2.9 TDMA measured change of particle size as function of oxidation temperature.

The most likely explanation for our experimental observation (and consistent with APM results to be presented later) would be the formation of an intermediate phase of the oxide, Ni_2O_3, at low temperatures, and further decomposition of Ni_2O_3 to NiO at higher temperatures. This is consistent with the fact that Ni_2O_3 is the thermodynamically favorable phase at low temperature, and decomposes into NiO and oxygen at temperatures above 600°C.

The reacted particle size can be estimated by assuming spherical particles of Ni completely covert to Ni_2O_3 or NiO. Our experimental values fall within this calculated size range. For example, for an initial 40 nm and 96 nm Ni particle, the particle size should increase to 55.6 nm and 132.6 nm for complete conversion to Ni_2O_3, and then decrease to 48.3 nm and 115.2 nm upon forming NiO, while our experimental value for an initial 40 nm particle increases to 51.3 nm at 600°C, and

then shrinks to 49 nm at 1000°C. For an initial size of 96 nm particle the size is 124.8 nm at 800°C and 121.8 nm at 1100°C. Also these results show that the smaller the initial particles size, the closer we achieve to full conversion, while larger particles require a higher temperature to achieve full conversion.

To further investigate the oxidation of nickel nanoparticles and evaluate the phase behavior observed in the TDMA experiments, we substitute the APM for the second DMA in order to track particle mass changes due to oxidation. As discussed previously, the APM classifies particles by mass through a balance of electrostatic and the centrifugal forces. For each particle mobility size, the APM was operated at fixed rotation speed, and as such the applied voltage can be directly related to particle mass. Panels (a), (b) (c) and (d) of Figure 2.10 show the results of the APM measured mass distribution at selected furnace temperatures for initial mobility size of 40, 62, 81 and 96 nm, respectively. Figure 2.11 shows the mass change ΔM as function of furnace temperature. Because the APM has a broader transfer function compare to the DMA, especially at the low end of the APM range, a plot of the experimental data for each temperature would overlap, and would be difficult to read. For this reason, we only show the experimental results at furnace temperatures of 25°C and 700°C. The particle peak mass distribution data at each furnace temperature were fit to a Gaussian function to obtain the peak mass and are shown in Table 2.2.

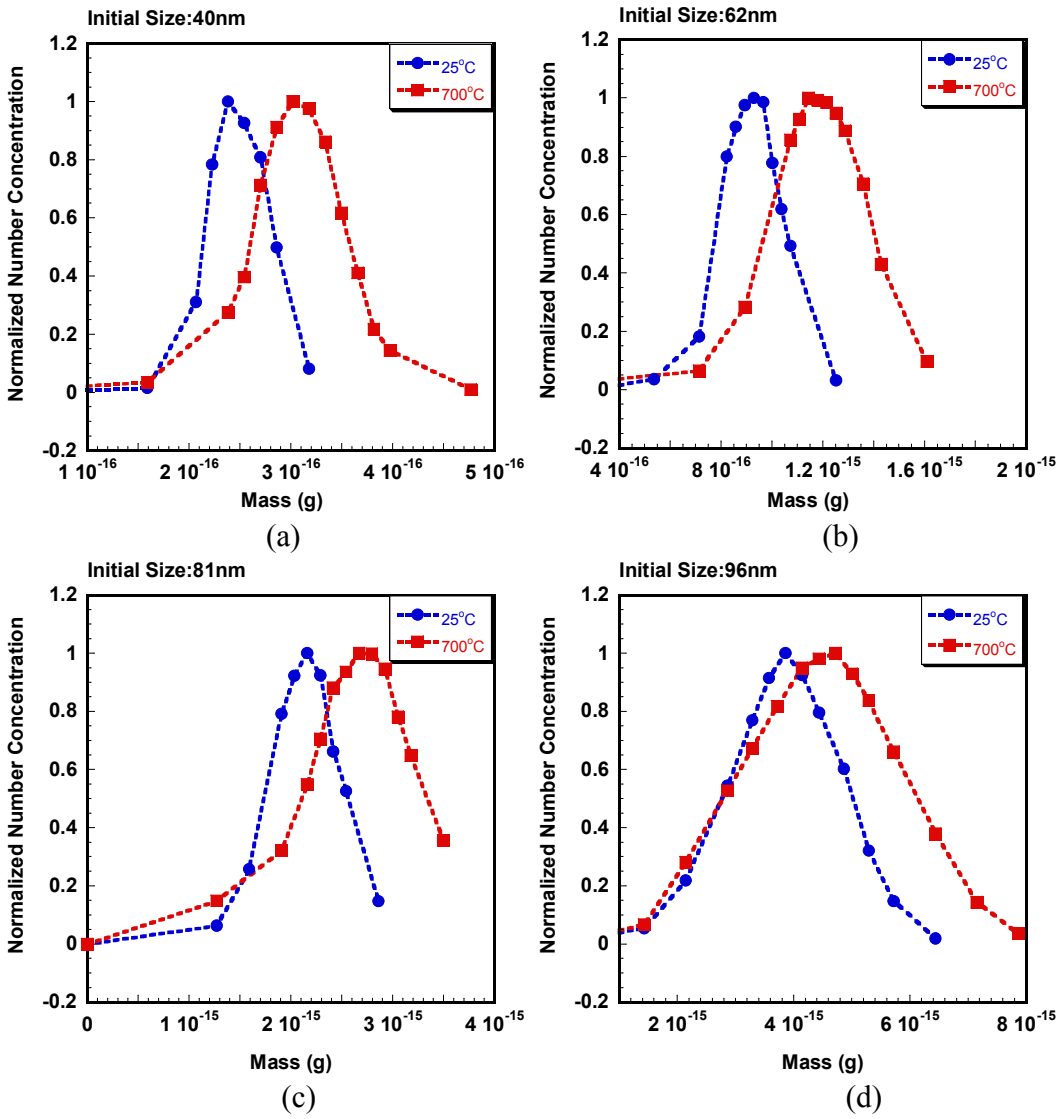

Figure 2.10 APM measured mass distribution for initial size of (a) 40 nm, (b) 62 nm (c) 81 nm and (d) 96 nm nickel particles at different oxidation temperatures.

It is clear from Figure 2.10 and Table 2.2 that there is a mass increase, with increasing furnace temperature, which reaches a maximum at above 600°C. On the other hand, from Figure 2.11, we can see in the hypothesized phase change region, the measured value for the mass fluctuates within the experimental uncertainty for initial 40, 62, and 81 nm particles, and increases slowly with increased temperature for the initial 96 nm particle. As we discussed above, the theoretical particle size

should grow to 55.6 nm and 136.6 nm for an initial 40 nm and 96 nm nickel particle, if we assume complete conversion, while the DMA measured value is 51.3 nm and 124.8 nm. This suggests that the nickel particle could as a multi-component oxide during the oxidation process.

Table 2.2: Change in particle mass as a function of oxidation temperature.

Furnace Setting (°C)	particle mass ($\times 10^{-16}$g)			
	40	62	81	96
25	2.48	9.19	21.43	36.81
300	2.50	9.40	21.44	37.25
400	2.65	9.73	21.93	37.40
500	2.82	10.29	23.10	38.30
600	3.03	11.42	25.12	41.15
700	3.08	11.89	27.12	44.85
800	3.11	12.03	27.21	46.34
900	3.10	11.98	27.39	47.28
1000	3.10	11.94	27.15	47.88
1100	3.11	12.23	28.16	48.40

Presumably the particle would have a nickel core with an outer oxide layer which contains both NiO and Ni_2O_3. Both the oxidation of the nickel core and decomposition of the outer Ni_2O_3 layer could occur simultaneously and result in a roughly constant particle mass as observed for small particles, and slow mass gain for large particles.

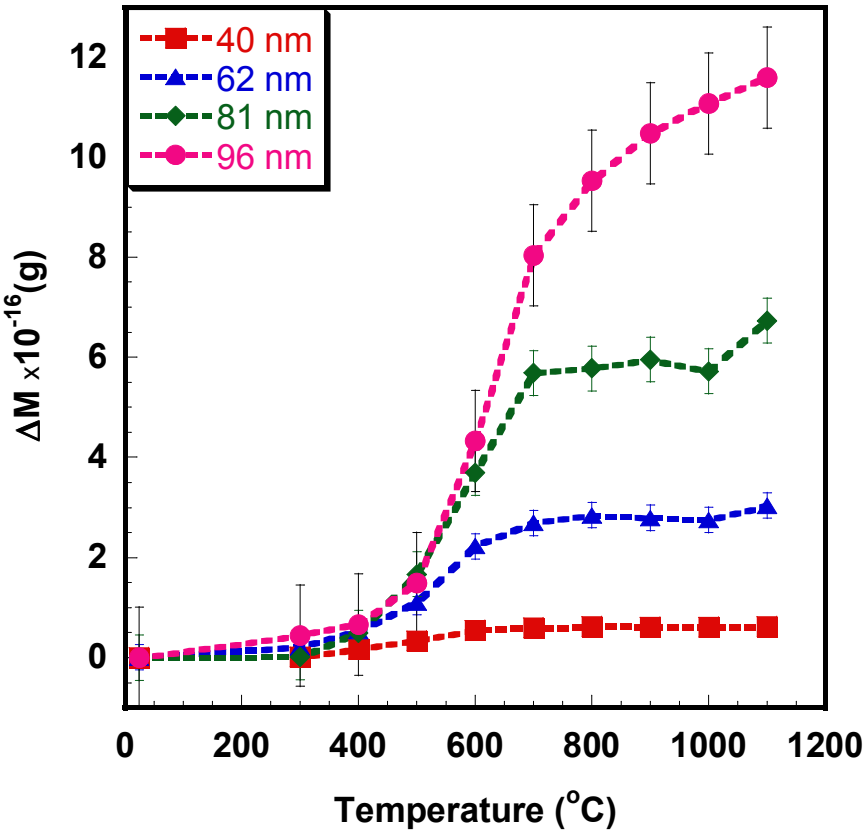

Figure 2.11 DMA-APM results for change of particle mass as function of oxidation temperature.

Our previous work showed that the APM when combined with TEM image analysis can accurately determine particle density.[68] More recently, the DMA-APM technique was used as an online measurement tool to obtain the particle density in understanding aluminum oxidation.[28] In this work, the average density profiles of reacted particles are calculated using the TDMA and APM measured particle size and mass, and shown in Figure 2.12. We find that as the furnace temperature increases, the average density of the reacted particles decreased monotonically to 4.7-5.0 g/cm^3, consistent with the density of Ni_2O_3 (4.84 g/cm^3).[7, 76] At higher temperatures the particle density increases to 5.5-5.7 g/cm^3 and at the highest temperature investigated

is roughly at a density half way between NiO (6.67 g/cm^3) and Ni_2O_3 (4.84 g/cm^3). The oxidation to form Ni_2O_3 should be dominant in the low temperature region while the process of formation of the two types of oxides, and the phase transition are coupled at higher temperatures.

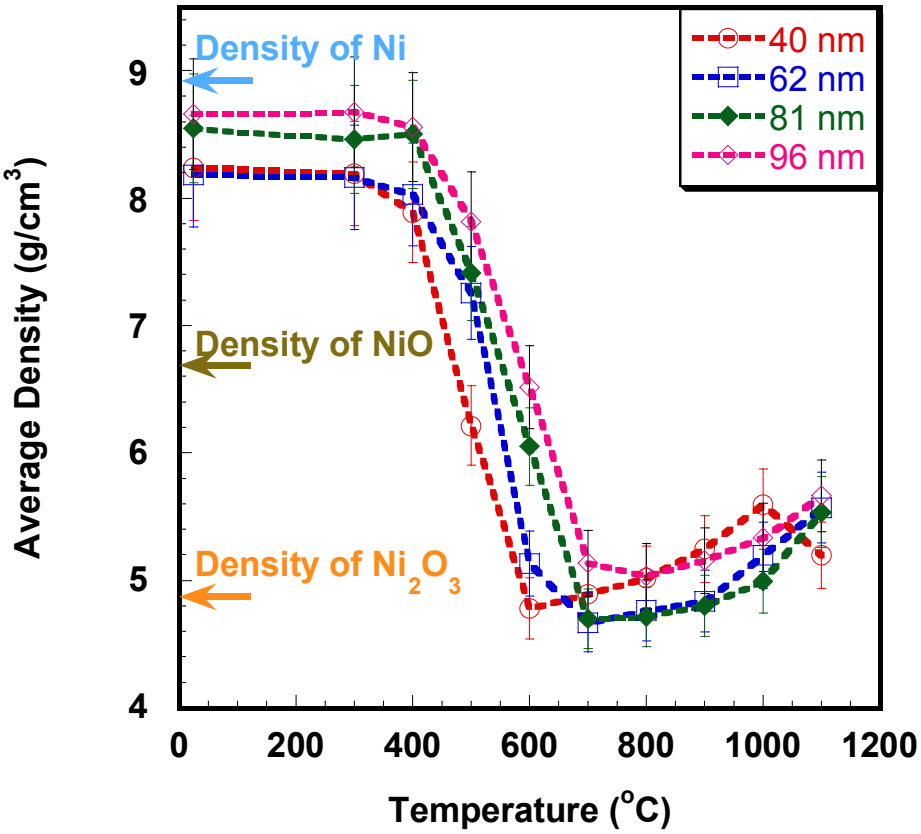

Figure 2.12 Average density measured using DMA-APM combined experiment.

2.3.2 Size Resolved Oxidation Kinetics of Nickel Nanoparticles

Metal oxidation theories and the transport properties of the oxides have been studied for several decades. It is believed that the diffusion of ionic vacancies and electron holes is the dominant transport process for nickel oxidation.[41] Thus, the well known diffusion controlled shrinking core model[77, 78] can be employed to extract the reaction rate constant. The theories proposed by Wagner for thick film

growth are based on conditions of charge-neutrality, and diffusion of ions and electrons being the rate-limiting step, lead to a parabolic rate law for a planar geometry.[60] Carter later applied the same assumptions to the shrinking core model for a spherical geometry, and derived an oxidation rate law for metal particle oxidation.[55] However, Wagner's theory is restricted to thick films in which the characteristic length is given by the Debye –Hückel length, which is probably on the orders of hundreds of nanometers.[41, 42, 45] Given the particle sizes we are studying, many of the assumptions of the theory would likely be invalid. For example, the charge-neutrality condition of Wagner's theory would no longer hold due to the space charge effects. Cabrera and Mott's, on the other hand, describe the thin film growth assuming thermal electron emission and tunneling of electrons, to be easier then ionic diffusion, so that an electric field is developed across the thin film to assist the transport of the ions.[59] The electric field caused by the surface-charge could be on the order of ~10^7 V/cm such that a nonlinear behavior has to be considered. The rate law for thin films was derived and a characteristic length L_{crit} was suggested, below which the field is so strong that the drift velocity of ions is not proportional to the field but has an exponential dependence, and this nonlinear effect should be consider when $L(t) < L_{crit}$. The upper limit for Cabrera and Mott's theory is ~10 nm for nickel, and L_{crit} is as small as 2 nm. No analytical result has been developed for the spherical geometry.

Fromhold and co-workers had given a more general theoretical model for metal oxidation.[42, 45, 48, 50, 53] However, the equations can only be solved numerically. In our case, the particle sizes falls in the range between the Wagner's

theory and Cabrera and Mott's theory. Nickel nanoparticle oxidation is most likely in a low-field region where surface-charge and space-charge should be considered. Fromhold and Cook had evaluated the space-charge and surface-charge modification on the oxidation kinetics with a coupled current approach based on the idea that the diffusion currents are in the steady state in the presence of surface/space charge, the growth kinetics was obtained by summing the ionic and electronic diffusion currents of all the species.[48] The results can only be solved numerically and no results are available for spherical particle oxidation.

More recently Fromhold has developed a model focused on the oxidation rate of spherical metal particles in the low space charge limit using the coupled current approach for oxide thicknesses below 100 nm.[40] Only surface charge and linear diffusion were considered in their study, and a same rate law similar to Carter's work was obtained. This suggested to us that the diffusion controlled shrinking core model could be applied to our study as a relatively straightforward way to process our experimental results.

Following Carter's analysis at steady state, the diffusion flux through the oxide shell can be related to the reaction rate of reactant, by

$$\frac{dN_{O_2}}{dt} = -4\pi DeCo_2 \frac{r_1 r_2}{r_2 - r_1} \tag{2.4}$$

In equation (2.4) r_1, r_2 are the radius of the nickel core, and the reacted particle radius. Co_2 is the oxygen molar concentration in gas and No_2 is the moles of oxygen in oxide layer. De is the diffusion coefficient for ion diffusion in the oxide layer:

$$De = A_m \exp(-\frac{E_a}{RT}) \tag{2.5}$$

Here A_m is the pre-exponential factor, E_a is reaction activation energy, and R is the gas constant. Equation (2.4) immediately leads to the mass change rate for the reacted nickel nanoparticle, as

$$\frac{dM}{dt} = 4\pi M_{O_2} DeCo_2 \frac{r_1 r_2}{r_2 - r_1} \tag{2.6}$$

where Mo_2 is the molecular weight of oxygen. Knowing the furnace temperature profiles from figure 2.5, the particle mass change, Δm can be obtained by integrating equation (2.6) as the particle travel down the oxidation furnace. However, as we discussed above, the nickel nanoparticle oxidation should be a composite between formation of NiO and Ni_2O_3, and the phase transition. Therefore the relative concentration of NiO and Ni_2O_3 within the oxide layer is temperature dependent. As a result, the instantaneous mass changing rate *dM/dt* can not be determined with our current experimental approach.

Considering the exponential temperature dependence of the rate constant and the fact that most of the reaction would occur at the center of the furnace at the peak temperature, we approximate the instantaneous mass changing rate *dM/dt* in equation (2.6) with the average mass changing rate to get

$$\ln \frac{\Delta M}{\tau} = -E_a / RT + \ln(4\pi M_{O_2} Co_2 A_m \frac{r_1 r_2}{r_2 - r_1}) \tag{2.7}$$

Here the peak temperature determined from figure 6 is used, and by using the mass change measured from the APM, the average mass change rate can be calculate for each furnace temperature. The size-resolved activation energy can be obtained from an Arrhenius plot as shown in Figure 2.13.

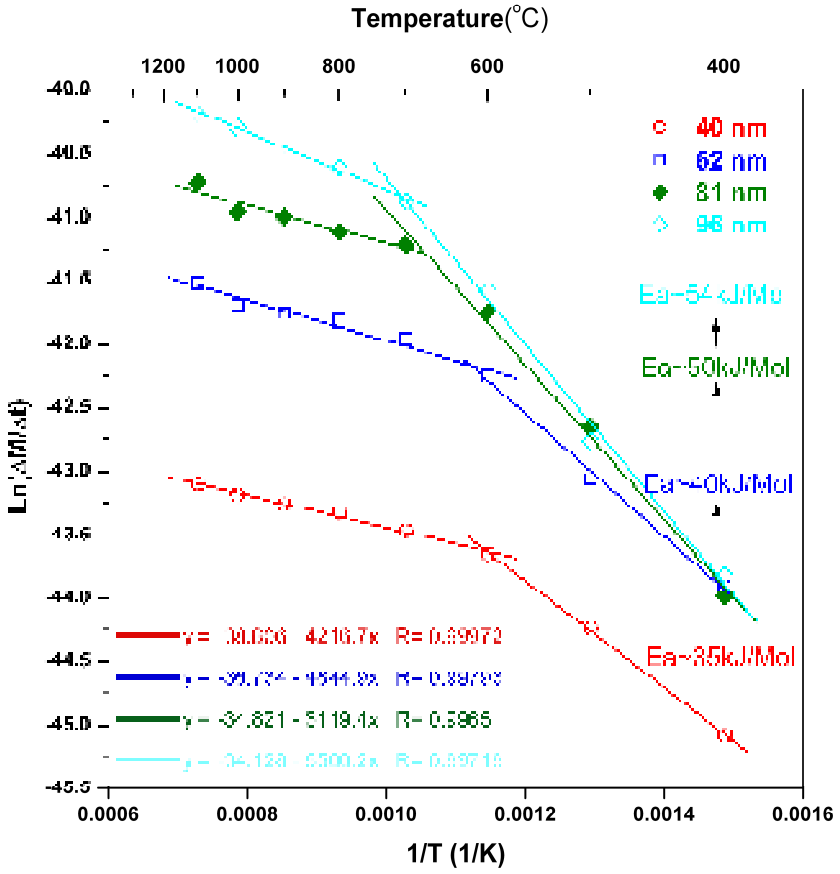

Figure 2.13 Arrhenius plots of average mass changing rate as a function of inverse temperature. The calculations for activation energy are only for the low temperature region.

Table 2.3: Summary for Arrhenius parameters for nickel nanoparticle oxidation.

Particle Mobility Size (nm)	Temperature range (°C)	Curve fit parameters ($Y = aX + b$)		Activation energy (KJ/mol)	Effective Diffusion Coefficients (10^{-9}cm^2/s)
		a	b		
40	400~600	4216.7	-38.8	35.0 ± 0.8	0.56~4.64
62	400~600	4844.9	-36.7	40.3 ± 2.6	1.02~17.0
81	400~700	6119.4	-34.8	50.8 ± 3.0	0.27~33.7
96	400~700	6566.2	-34.1	54.6 ± 2.9	0.18~35.4
40	700~1100	1267.7	-42.2	10.5 ± 0.5	NA
62	700~1100	1336.9	-40.6	11.1 ± 1.5	NA
81	800~1100	1479.8	-39.7	12.3 ± 2.2	NA
96	800~1100	2085.3	-38.7	17.3 ± 0.4	NA

Considering that only very small mass changes were observed at 300°C, we do not use results from that temperature to process the data. Two different regions can be distinguished from the Arrhenius plot, as the oxidation process transitions to a phase change region at ~600-700°C. The kinetic parameters for both regions can be determined using linear fit. The curve fit parameter as well as the size-resolved activation energies obtained are summarized in Table 2.3 and the results for the low temperature region are also shown in Figure 2.13. The calculated activation energies in the low temperature region decrease from 54 KJ/mol to 35 KJ/mol as the particle mobility size decreases from 96 nm to 40 nm. The activation energies are significantly lower in the phase transition region, and further investigation is needed to understand this phase behavior. The activation energy obtained here (~0.4 eV) are considerably smaller than the value of 1.5 eV reported by Karmhag et. al. for micro size Ni particles oxidation and 1.34 eV for nano size Ni particles oxidation,[62, 64] and also smaller than 1.78 eV for grain boundary diffusion limited thin film oxidation reported by Atkinson.[41] This difference between conventional methods and our approach has been consistently observed in previous work.[4, 5] Moreover, the

activation energy obtained here are much closer to the value of 0.6~0.9 eV for electron transport in single crystal nickel oxide,[78] and consistent with the reported activation energy of 0.3 eV for single crystal Ni oxidation in the early film-thickening stage.[79] It is well known that there are significant drawbacks of the conventional methods associated with the influence of experimental artifacts.[6] In those methods, usually milligrams of bulk sample are needed, while the sample mass of our aerosol based techniques is ~ 1 fg. For a highly exothermic reaction such as metal oxidation process, the large exotherm in a bulk sample will corrupt the observed onsite temperature, and the rapid reaction will lead to heat and mass transfer effect for bulk sample. As a consequence, the kinetic parameters extracted from the conventional methods are obscured. The TDMA and DMA-APM techniques employed here allow a direct measure of mass and volume change of individual particles thus enables us to explore the intrinsic reactivity of nanoparticles with minimizing the sampling error introduced by mass and heat transfer.

The effective diffusion coefficient is determined by calculating the unreacted nickel core radius r_1. Although the oxide layer contains both NiO and Ni_2O_3, and their relative concentration can not be determined, the oxygen concentration is roughly uniform for NiO and Ni_2O_3. Calculation shows that the relative oxygen density in NiO is 1.42 g/cm^3 and in Ni_2O_3 are 1.40 g/cm^3. The uniform oxygen density enables us to estimate the nickel core radius using the mass change of particle measured by the APM. Therefore the effective diffusion coefficient can be calculated from equation (2.6). Since the shrinking-core model used here can only count for the oxidation process, the phase transition in high temperature region will corrupt the

calculation of the effective diffusion coefficient. As the consequence, the calculation is only valid in the low temperature region and the results are shown in Figure 2.14.

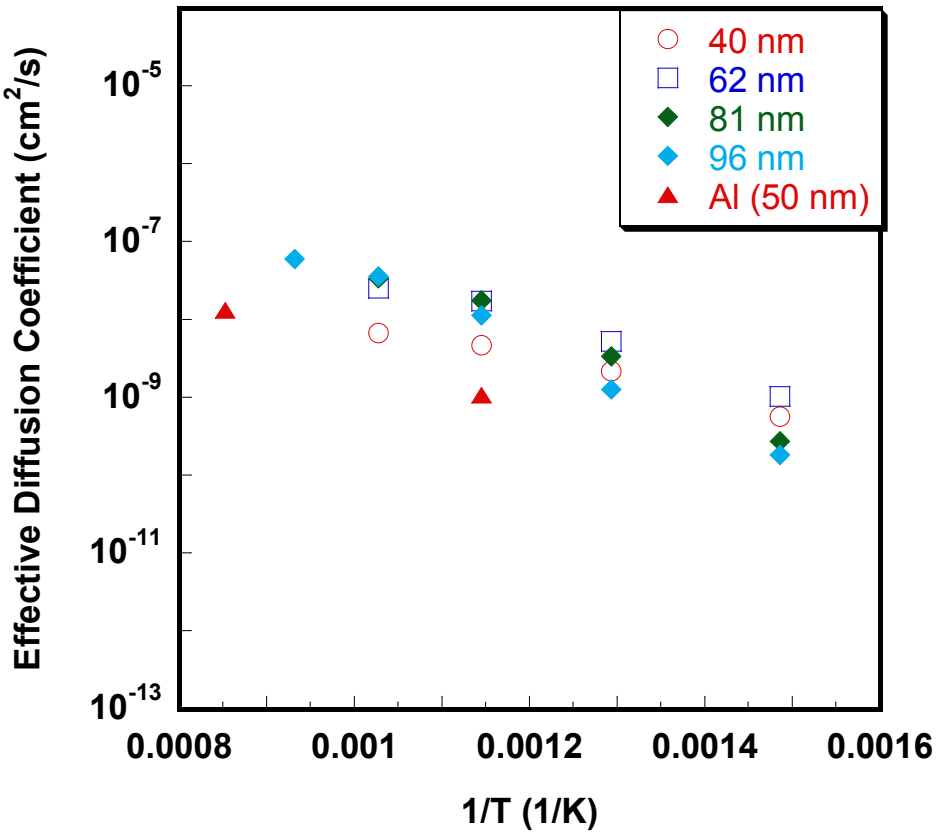

Figure 2.14 Arrhenius plot of effective diffusion coefficients in the low temperature region for Ni and Al.

Due to the well known kinetic compensation effect, although the activation energy is considerably smaller than the value measured by the conventional offline methods, the measured diffusion coefficient are within the range of reported values.[41] Since aluminum has been well studied and has been used extensively as a primary thermite based material, the effective diffusion coefficients for aluminum oxidation obtained from our previous work is also plotted in the figure for comparison.[4] Surprisingly to see that that nickel is actually more active than

aluminum although it should be pointed out that the aluminum measurements were made with a totally different experimental approach. However despite the apparent faster kinetics of Ni, the higher enthalpy of aluminum oxide (-1675.7 kJ/mol vs. -489.5 kJ/mol for Ni_2O_3 or -239.7 kJ/mol)[7, 8] implies aluminum is still a more promising energetic material that nickel. Nevertheless, Ni might find applications as an ignition source for example, or in tuning the reaction profile in mixed metal nanocomposites.

Particle burn time for different initial particle size at different temperatures was also calculated using the burn rate and the total mass change measured from the APM. These results are plotted on a log scale in Figure 2.15, and show for all temperatures a diameter dependence well less than 2 ($\sim Dp^{1.4}$). For large size particles (micron size), the diffusion controlled reaction would lead to a $\sim Dp^2$ dependence,[77] and a $\sim Dp^{1.8}$ dependent is reported experimentally.[80] For nano size particles, however, a much weaker size dependent has frequently been observed.[16, 80, 81] A melt dispersion mechanism for very fast reaction of nano thermites were recently proposed to explain this observation.[81] Fast heating creates huge thermal stresses between the metal core and oxidation shell and results in the spallation of the shell and complete explosion of the core, the oxidation of dispersed metal clusters, is much faster than diffusion and is independent of particle size. However, this mechanism is valid for particles with a melting core and a solid shell, and is expected only for fast heating rate ($\sim 10^7$ $^oC/s$) as compared with our $\sim 10^3$ - 10^4 $^oC/s$ heating rates. A phenomenological model was developed for aluminum oxidation in our previous work which indicated that due to the internal pressure gradient in the particle, a

~$Dp^{1.6}$ dependent was found. More generally, for the oxidation of metal, Fromhold shows that a space charge layer in the growing oxide could has significant effects on the oxidation process for particles in the range of 10 nm ~ 100 nm, which can either retard or enhance the diffusion flux through the oxidation shell depending on ionic or electronic species as rate limiting. Our results for particle burn time suggested that a model that includes both the pressure gradient and space charge effect would be worthy of investigation.

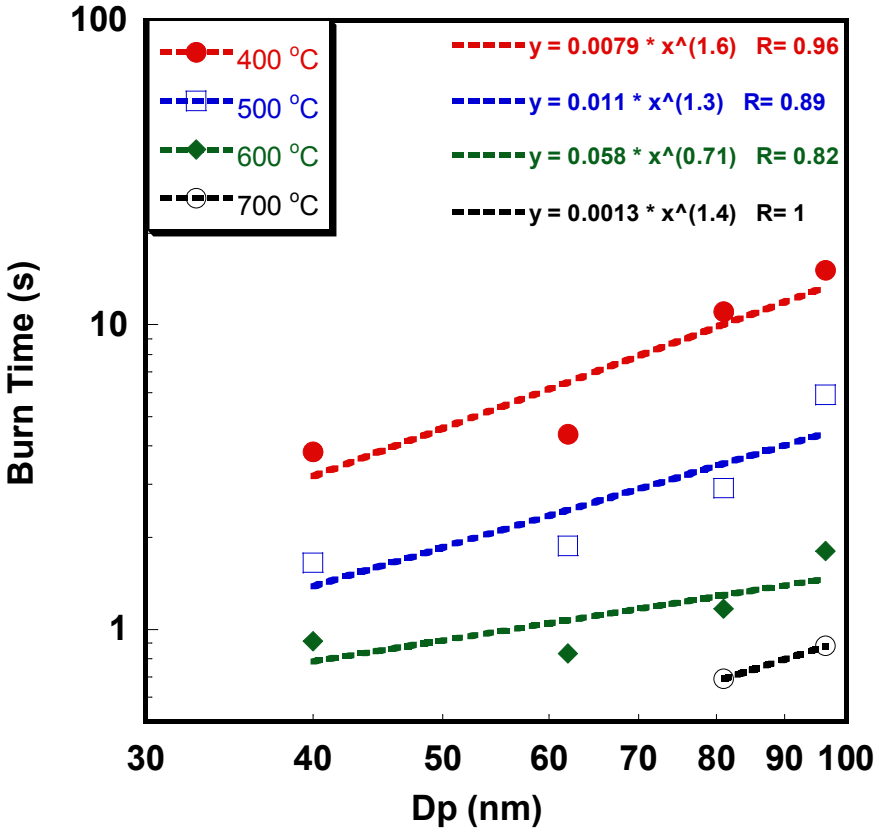

Figure 2.15 Particle burn time at different temperatures as a function of initial particle size

2.4 Conclusions

We applied online aerosol ion-mobility based methods to study oxidation and reactivity of nickel nanoparticles. The nickel nanoparticles were generated in-situ during the oxidation experiments using gas-phase thermal pyrolysis of nickel carbonyl. Particles of well controlled sizes and structure were generated and subsequently size selected using a DMA. The mass and size changes of reacted particles were measured using an APM and a second DMA. The experimental data can be divided into an oxidation region and a phase transit region. Based on the diffusion-controlled rate equation in the shrinking core model, we found that the activation energy of oxidation decreased from 54 KJ/mol to 35 KJ/mol as the particle size decrease from 96 nm to 40 nm at low temperatures. The absolute burning time and the effective diffusion coefficient were also determined.

Chapter 3

Understanding the Interaction of an Intense Laser Pulse with Nanoparticles: Application to the Quantification of Single Particle Mass Spectrometry

3.1 Introduction

In the preceding chapter, we illustrated the application of ion-mobility spectrometry to the study of the reactivity of metal nanoparticles. The advantage of the ion-mobility approach is the capability of conducting measurements without any substrate. Another approach that has the similar capability is Single Particle Mass Spectrometry (SPMS), furthermore, SPMS can provide both particle size and composition information simultaneously in a qualitative or even quantitative way. These advantages promote SPMS to a unique position for tracking the change of an individual nanoparticle upon reactions. Previously, our group has utilized SPMS to characterize the intrinsic reactivity of aluminum nanoparticles.

Many advances in single-particle mass spectrometry for quantitative characterization of size and composition of particles have been made in the last decade.[3, 5, 30-35] Typically for these experiments a pulsed laser is used as the ionization source, from which time-of-flight mass-spectrometry can be used to deduce composition. The common practice is to use some other method such as light scattering to deduce the size of the particle just prior to ionization, thereby obtaining a measure of both size and composition.[35] While the technique has proven itself to be highly reliable, it suffers from the limitations inherent to all light scattering, namely the high power dependence on particle size, which has generally limited the technique

to particles greater than ~200 nm. More generically a light scattering, or other particle selection approach however, (e.g. mobility selection, size selective aerodynamic focusing, etc) does not take advantage of the inherent capability of the mass spectrometer, to not only provide composition information, but total mass as has been attempted by our group and the work of Reents.[32, 82]

Recently, we and others, with the use of a highly focused pulse laser, determined both total particle mass (i.e., size) and composition quantitatively using only the ion signal from a laser ionization time-of-flight mass spectrometer.[4, 5, 32, 82] The quantification of composition and size of nanoparticles can be achieved with reasonable accuracy when two primary conditions are met. One is near complete atomization/ionization of the particle constituents (i.e., all neutral atoms are converted to ions with few molecular species), and two, ions produced from the particle should be detected independent of composition and size, or with a known relationship.[82] Typically a strong laser peak fluence (~10^{11} W/cm^2) that is several orders of magnitude higher than the theoretical energy to atomize and singly ionize all atoms in the particle has been employed. On the other hand, the detection efficiency of ions in the single particle mass spectrometry is highly sensitive to their properties (e.g., kinetic energy) and the laser parameters (e.g. pulse width). The strong laser pulses might produce highly energetic ions so that their transmission efficiency to the detector in the aerosol mass spectrometry (usually through the time-of-flight tube) would be degraded.[82] This suggests if size-dependent or composition-dependent energetic ions are formed, and their relationships are not understood, it will degrade our ability to quantify the composition and size of particles.

The objective of this chapter is to understand in greater detail the interaction of a laser pulse with a nanoparticle so as to determine the characteristic properties of ions produced from the particle. In the present study, we employed a modified 1-D hydrodynamic model based on prior work of Milchberg et al.[36] to simulate the temporal evolution of ionization state, and energy as a function of particle size of aluminum that was heated and ionized by a nanosecond 532nm Nd:YAG laser. The effects of the laser pulse width (i.e. laser intensity) on the ion properties produced after laser-particle interaction were also examined. The simulation results are compared to measurements obtained with a well characterized single particle mass spectrometer that developed in our lab.[5, 82] This work was done along with Dr. Kihong Park using the hydrodynamic code developed by professor Howard Milchberg, and the results are published.[83]

3.2 Particle Size and Mass Measurement by SPMS

The SPMS consists of an aerodynamic lens inlet, three stage differential vacuum systems, a free firing pulsed laser for particle ionization, a linear time-of-flight mass spectrometer, and a 500 MHz digital oscilloscope and PC for data acquisition, as shown in Figure 3.1. Detailed description of SPMS can be found in our previous publications.[5, 82] The aerodynamic lens system produces a narrow collimated particle beam and transports particles of 30 – 300 nm into the high vacuum system with a high transmission efficiency. The free firing pulsed laser (a frequency-doubled Nd:YAG laser operated at 10 Hz, 532 nm wavelength), through a spherical plano-convex lens, is tightly focused at the extraction field of the mass spectrometer and intersects the particle beam with a laser beam diameter of ~0.1 mm and a laser

pulse duration of ~5 ns. We have found that a pulse energy of ~100 mJ/pulse, corresponding to a peak laser power density at the focal point of approximately ~10^{11} W/cm^2, provided sufficiently high level of ion currents to provide quantitative composition measurement. When the laser hits a particle successfully, positive ions formed from the particle are accelerated along ~1 m time-of-flight tube and detected by microchannel plates (MCP).

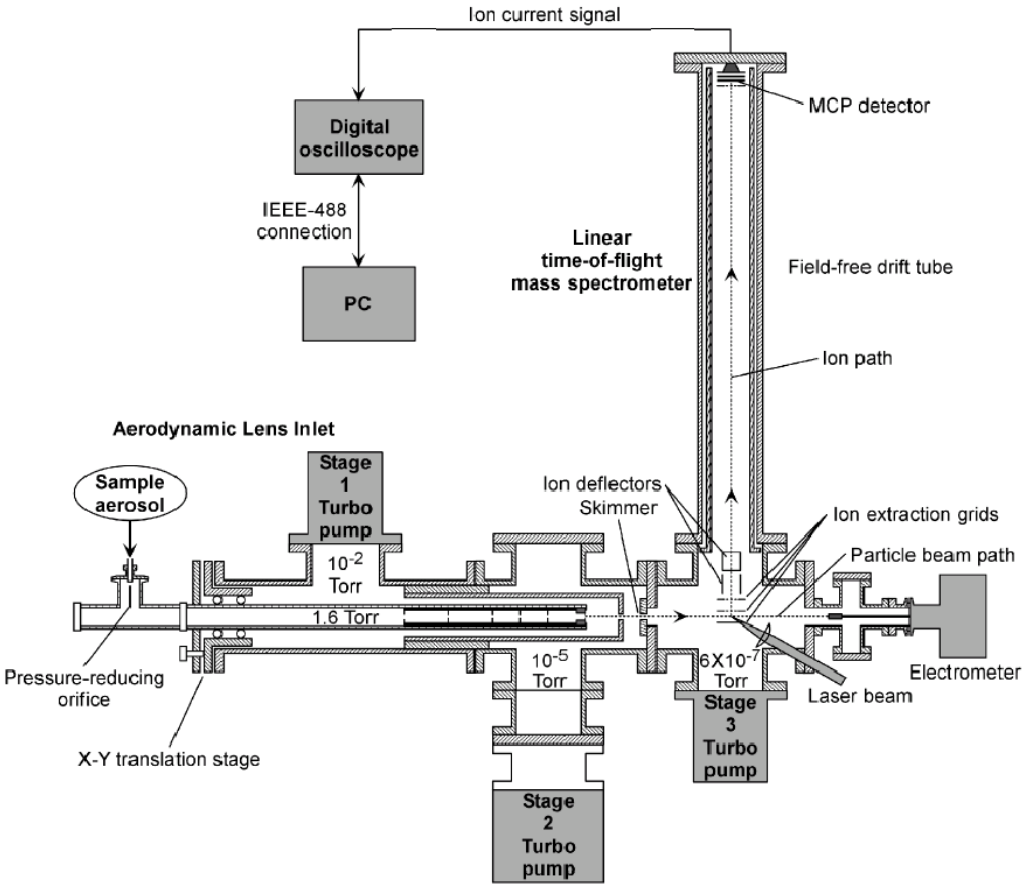

Figure 3.1 Schematic of single particle mass spectrometer (SPMS).

As we mentioned in the introduction, a complete ionization technique is employed in SPMS. The highly focused laser beam can completely ionized the atoms within particles, and only positively charged atomic ions are produced from laser-particle interaction. The nature of complete ionization enables us to extract quantitative information about the stoichiometry of individual aerosol particles. The elemental composition of the particle can be obtained by integrate the ion peak signal in the mass spectra. In our previous work, we have demonstrated the elemental composition measurement by SPMS for various types of particles, and the results are summarized in Table 3.1.[5] These results show that the elemental stoichiometry measurement of individual particles by SPMS can be achieved within 15% of the theoretical values.

Table 3.1 Summary of elemental ratio measurement by SPMS

Particle	Ratio Considered	Experimental Value	Theoretical Value	% Error
Aluminum nitrate	N:Al	3.08	3.00	2.7
Aluminum oxide	O:Al	1.47	1.50	-2.0
Sodium chloride	Na:Cl	1.14	1.00	14.0
	^{35}Cl:^{37}Cl	3.00	3.13	-4.2
Strontium nitrate	N:Sr	1.95	2.00	-2.5
Pure silver	^{107}Ag:^{109}Ag	1.12	1.08	3.7
Ammonium sulphate	N:S	2.27	2.00	13.5

In addition to elemental measurement, the mass spectra obtained from SPMS also contain particle mass information because of the complete ionization. The total ion peak area can be directly related to particle mass, e.g. total peak area ~ particle total mass ~ particle size^3. Therefore, both composition and particle size distribution can be measured simultaneously from SPMS mass spectra. In our previous work, we have accomplished the particle size measurement using SPMS.[82] A size distribution of laboratory prepared polydisperse NaCl particles measured by SPMS is compared with the size distribution measured by the DMA, as shown in figure 3.2. The results agree with each other well.

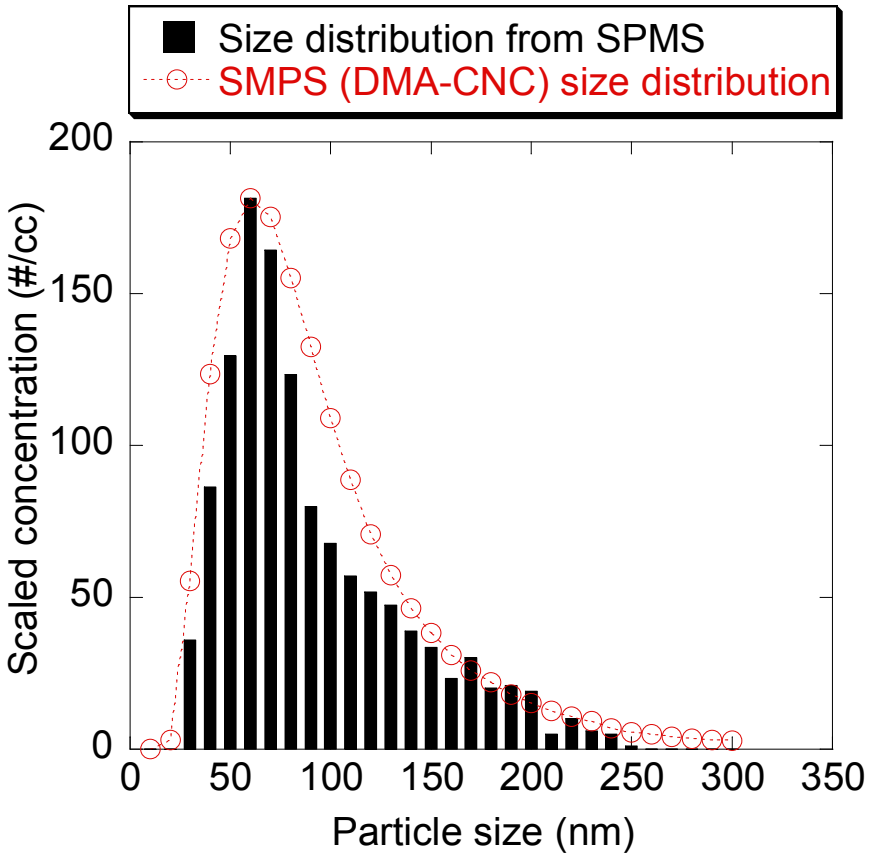

Figure 3.2 Particle size distribution measured by SPMS and compare with DMA measurement.

As we can see from the results shown in table 3.1 and figure 3.2, the Single Particle Mass Spectrometry is a powerful tool for nanoparticles characterization. It has the capabilities of conducting quantitative measurement on particle composition and mass/size without any substrate, which allow us to probe the reactivity of nanoparticles on individual particle level. In our previous work, we have employed SPMS to study the reactivity and oxidation kinetics of aluminum nanoparticles.[4] Similar to the ion-mobility approach discussed in the previous chapter, aluminum nanoparticles were generated *in-situ* for the oxidation study. These aluminum nanoparticles were mixed with air and subsequentially sent to a reaction furnace, and the oxidized particles were measured using SPMS. Figure 3.3 (a) is a typical mass spectra obtained for a bare aluminum nanoparticle prior to oxidation and figure 3.3 (b) is mass spectra for an oxidized nanoparticle. Here in figure 3.3 (b) the O/Al ratio of 1.47 suggest this particle is fully oxidized and converted Al_2O_3. This results show that our SPMS can track the oxidation process of individual nanoparticles. Furthermore, since the mass spectra already contain the particle total mass/size information, the size dependent kinetics study can be conducted by SPMS even without DMA size-selection. This example illustrates the application of SPMS to probe the reactivity of nanoparticles. Here is this thesis, we will focus on the improvement of SPMS by understand the laser-particle interaction processes (this chapter), as well as experimentally examine the limitations of the complete ionization technique on characterizing multi-component nanoparticles (chapter 4).

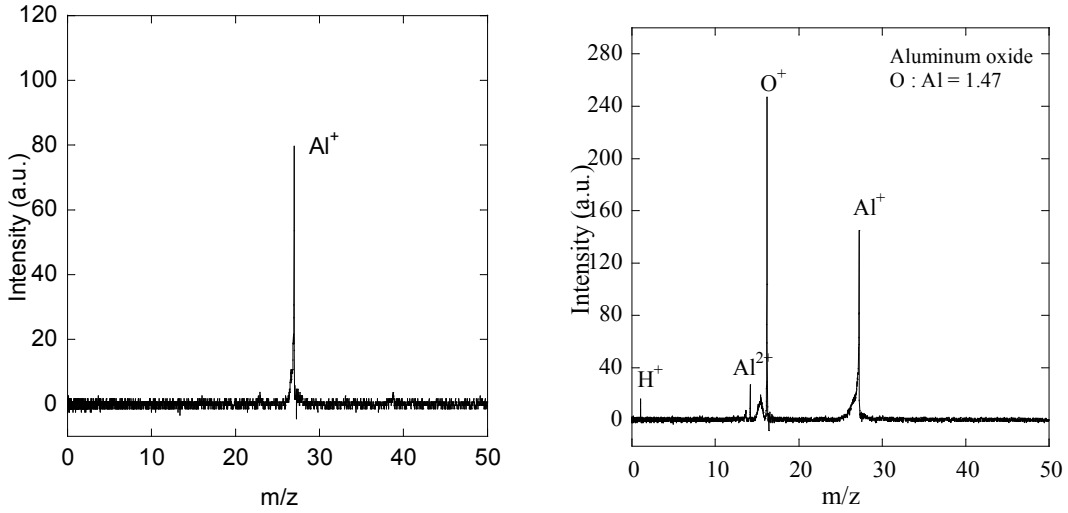

Figure 3.3 Using SPMS to track the oxidation of Al particles (a) mass spectra of an aluminum nanoparticle before oxidation and (b) mass spectra of an aluminum nanoparticle after oxidation and form Al_2O_3

3.2 Model Description

Several models to describe the interaction of clusters with a laser pulse have been developed.[36, 84, 85] In the coulomb explosion model, laser-heated electrons can escape the cluster early in the laser-cluster interaction, leading to a charge buildup in the cluster. This charge buildup will lead electrostatic forces to be dominant in the cluster expansion, resulting in a so called coulomb explosion. On the other hand, in the hydrodynamic model, the plasma dynamics are driven in response to hydrodynamic forces rather than electrostatic forces. Milchberg et al. showed that the hydrodynamic forces dominate electrostatic forces for clusters larger than 5 nm, and a laser peak intensity of $>10^{14}$ W/cm^2. However, for typical single particle mass spectrometry operation the situation is typically more complicated. For a peak intensity $\sim 10^{11}$ W/cm^2, and particles of 20 - 400 nm, a purely hydrodynamic model is only valid after sufficient laser heating has taken place to overcome the cohesive

energy of the solid. Essentially we can think of the laser interaction process as taking place in two steps. First a rapid laser heating, with evaporation of neutrals from the particle surface followed by a second step of resonant absorption and hydrodynamic plasma expansion.

In a previous work, we developed a phenomenological model to study the mass and energy transfer processes for the combustion of aluminum nanoparticles.[28] In this study, a similar model was employed to account for the laser-particle heating, and particle evaporative cooling, and integrated into a one-dimensional hydrodynamic model to derive ion properties resulting from laser-particle interaction.[36] While our calculations are focused on aluminum, because of our experimental measurements and because modeling a mono-atomic particle are considerably easier, the results on the features of laser-particle interactions are expected to be qualitatively generic, and should lead to a greater mechanistic understanding, and as a guide for future experimental developments.

3.2.1 "Soft" Particle Heating

During the early stages of the laser pulse, the laser intensity is relatively low, such that the amount of energy absorbed is below the cohesive energy, so that the particle experiences a "soft" heating and results in neutrals being evaporated. The particle temperature and radius are determined by a coupling of laser heating and evaporative cooling. The effect of vaporization was examined by solving the energy balance in the free molecule regime.[28, 36] The energy absorbed from the laser, q_{abs} is balanced with the energy used to evaporate aluminum from the particle, q_{evap} and the energy used to heat the particle, as follows:

$$q_{abs} = q_{evap} + \frac{d}{dt}\left(m_p c_p T_p\right) \tag{3.1}$$

$$q_{abs} = \frac{1}{2}\omega \,\mathrm{Im}(\gamma)\left|E\right|^2 \tag{3.2}$$

$$q_{evap} = L_{vap,Al} \times w_{Al} \times 4\Pi r^2 \tag{3.3}$$

Here m_p is the mass of aluminum particle, c_p is the specific heat of aluminum, r is the radius of particle, and T_p is the temperature of particle. q_{abs} can be calculated using laser angular frequency ω, the imaginary part of particle polarizability Im(γ) and the electric field generated by the laser E, $L_{vap,Al}$ is latent heat of vaporization for aluminum, w_{Al} is the free molecular evaporation flux of aluminum atoms, and is given by

$$w_{Al} = \frac{P_d}{\sqrt{2\Pi RTM}} \tag{3.4}$$

R is the gas constant, and P_d is the equilibrium vapor pressure of aluminum as determined by the Kelvin equation:

$$P_d = P_0 \times \exp\left(\frac{4\sigma v_1}{T(ev)d \times 1.6 \times 10^{-19}}\right) \tag{3.5}$$

Here P_0 is the vapor pressure over a flat surface at temperature T, σ is the surface tension of aluminum, v_1 is the monomer volume, and d is the diameter of the drop. Vapor pressure P_o and surface tension σ can be calculated by equation (3.6) and (3.7).

$$P_0 = \exp\left(13.07 - \frac{3}{T(ev)}\right) \times 1.01 \times 10^6 \text{ Dyne/cm}^2 \tag{3.6}$$

and

$$\sigma = 948 - 0.245 \times 10^4 T(ev) \text{ Dyne/cm}^2 \tag{3.7}$$

The use of equation (3.7) is only valid to approximate 0.5 ev, at which point

the surface tension becomes negative implying that the particle is mechanically unstable. In such a case, the free molecular evaporation rate w_{Al} is obtained from the effective equilibrium condensation rate and detailed balancing[1]

$$w_{Al} = \frac{P_0}{\sqrt{2\Pi RTM}} \tag{3.8}$$

The energy balance is solved to obtain a temporal profile of particle size and temperature, and the results are used as input parameters for the hydrodynamic model.

3.2.2 Hydrodynamic Model

The hydrodynamic simulation is based on a one-fluid two temperature (i.e., electron and ion temperature) model, which includes thermal conduction, and a collision-radiative model for the ionization dynamics, the complete details for which are presented elsewhere.[36] Briefly, the laser's electric field (= *E(r)*, 1-D solid angle averaged electric field) is used to heat, and ionize the particle, and to advance the non-equilibrium time-dependent plasma hydrodynamics of the heated particle. The electric near field is described by, $\nabla \cdot (\varepsilon E) = 0$, where $\varepsilon(r)$ is the dielectric function, and is coupled to a 1-D radial Lagrangian hydrocode. A near field approximation is appropriate for the case when the product, $ka << 1$, where $k\ (= 2\pi/\lambda)$ is the laser wave number, and *a* is the particle radius. For example, for a 20 nm diameter particle, excited with a visible laser, $ka \sim 0.1$. The dielectric response ($\varepsilon(r)$) of the laser-heated plasma is taken to be a Drude form, which is appropriate for strongly heated near-solid-density plasmas with little electronic band structure.[86] The 1-D radial

Lagrangian hydrocode model is outlined below including the mass (3.9), momentum (3.10), and energy (3.11) equations.

$$\frac{\partial \rho}{\partial t} + \nabla \cdot (\rho \vec{v}) = 0 \tag{3.9}$$

$$\frac{\partial \rho \vec{v}}{\partial t} + \nabla \cdot (\rho \vec{v}\vec{v} + P) = 0 \tag{3.10}$$

$$\partial(\rho e + \frac{1}{2}\rho v^2) \Big/ \partial t + \nabla \cdot ((\rho e + \frac{1}{2}\rho v^2)\vec{v} + P\vec{v} + \vec{q}) = S_{laser} \pm S_{\text{ionization/recombination}} \tag{3.11}$$

where ρ is the mass density, v is the fluid velocity, P is the pressure, taken to be isotropic, e is the internal energy per unit mass of the fluid, q is the heat flux, S_{laser} is the energy deposition rate by the laser per unit volume, and $S_{ionization/recombination}$ is the energy stored in the ionization state of the plasma, and the plasma internal energy. The rate equation for the ion species, which includes collisional ionization, recombination, and field ionization, are as follows:

$$\frac{dN_j}{dt} = S_{j-1}N_{j-1}N_e - (S_j + \alpha_j)N_jN_e + (\alpha_{j+1})N_{j+1}N_e + w_{j-1}(|E|)N_{j-1} - w_j(|E|)N_j \tag{3.12}$$

where N_j is the number density of ion at the ionization state j, S_j is the collisional ionization rate, α_j is the recombination rate, N_e is the electron density, E is the laser electric field, and w_j is the field ionization coefficient.[87] At each time step, the electric near field is solved using the density and temperature profiles of neutrals, ions, and electrons of the previous time step. The resulting electric field ionizes, and heats the plasma, temporally evolving the density and temperature profiles. Field and collisional ionization, recombination, and thermal conduction either gradient based or

flux limited are taken into account in the calculation as shown in the above equations. The ideal gas equation of state is used to relate the plasma temperature and pressure.

3.3 Experimental

In order to experimentally determine the relationship between particle size and the amount of ions detected with the single particle mass spectrometer (SPMS), we first need to generate aerosols and transport them to the SPMS. For generation of aerosols, we dispersed commercial aluminum nanopowders (Aveka Inc.) in methanol, and silver nitrate and sodium chloride in deionized water, and suspended them in the air using a collison atomizer. These particles were passed through several aerosol diffusion driers to remove the solvent. The aerosol was then passed through a differential mobility analyzer (DMA)[27] to select particles of known size for direct delivery to the inlet of the SPMS.

3.4 Results and Discussion

In our present (experimental) study, aluminum nanoparticles are irradiated with a 532 nm, 5 ns FWHM 100 mJ Gaussian pulse (Nd:Yag laser) with a peak laser intensity of $\sim 1.55\times10^{11}$ W/cm^2. As mentioned above, the particle first undergoes a soft heating process to overcome the cohesive energy of aluminum and then transitions to a hydrodynamic plasma expansion. The temporal and spatial profiles (1-D) for density, temperature, and velocity of electrons and ions from the laser-particle interaction can be obtained by a complete simulation of both models.

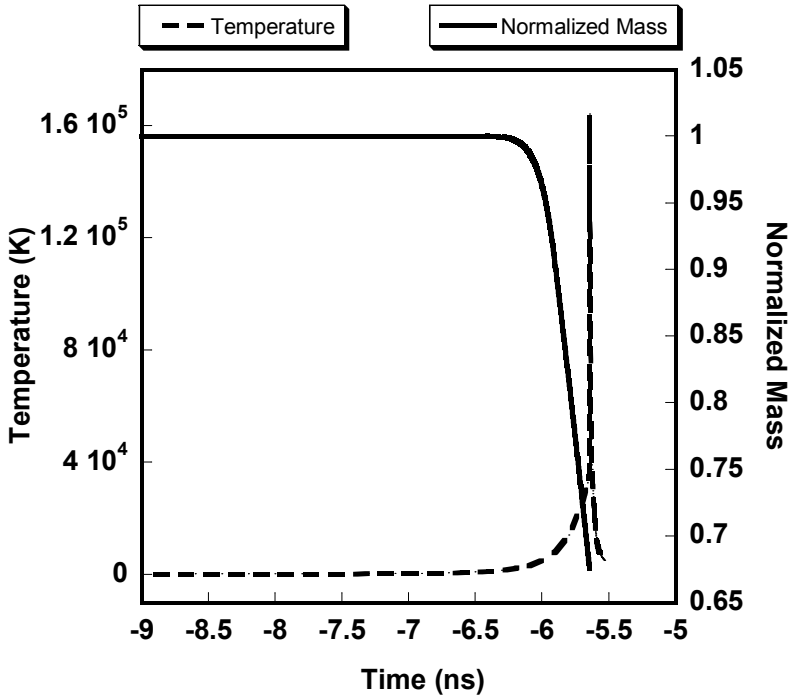

Figure 3.4 Simulation of soft laser heating of 100 nm Aluminum as a function to time. Time=0 corresponds to the peak in the 532 nm, 5 ns FWHM 100 mJ Gaussian laser pulse.

Figure 3.4 shows results for the temporal variation in temperature and particle mass, for the early stage of particle heating for aluminum of 100 nm diameter. The laser peak is at t = 0 and the interaction between laser and particle is observed from t = -9 ns. As discussed above, the cohesive energy of aluminum will delay the hydrodynamic expansion of the particle in the early stage of the laser-particle interaction, until the temperature reaches the cohesive energy threshold (~ 3 eV). After the particle temperature reaches the cohesive energy threshold, electrons and ions energies are high enough such that the particle rapidly transitions into a dense plasma and expands in response to hydrodynamic forces, where the high-density collisional processes are dominant in particle ionization and heating. During hydrodynamic expansion, the particle is rapidly heated to a very high temperature (>

10^5 K) and then cools rapidly due to expansion cooling as shown in Figure 3.4. It is also interesting to note that the temperature increases so rapidly that particle heating is much faster than the ability to evaporate mass, as evidenced by the very small evaporation loss from the particle during the soft heating.

The normalized electron density and electric field for a 100 nm diameter particle during the hydrodynamic expansion are presented in Figure3.5 (a) and (b). The initial electron density of aluminum is 6.026×10^{22}/cm3**.** In Figure 3.5 (a) the electron density (N_e) is normalized by the critical plasma density ($N_{cr} = m_e\omega^2/4\pi e^2 = 3.95\times10^{21}/cm^3$) where m_e is the electron mass, ω is the laser frequency, and e is electron charge. Results are presented from the point in time when the temperature reaches the cohesive energy threshold, at -5.644 ns. The critical plasma density defines the point below which the plasma becomes transparent to the laser beam, and no further energy deposition takes place. Figure 3.5 (a) indicates that the electron density profile is non-uniform during the expansion, and that there is a critical density surface (i.e., $N_e \sim N_{cr}$) where resonant laser light absorption occurs, and is maintained from -5.644 ns to -5.634 ns, about ~ 10 ps. Figure 3.5 (b) presents the vacuum level normalized electric field during the hydrodynamic expansion as a function of radial location and time. Near the region of the critical density surface (radial location) the corresponding electric field is significantly enhanced with respect to its vacuum value as shown in figure 3.5 (b). This time (~ 10 ps) can be defined as the critical density lifetime (τ_{cr}), which is the time for a laser heated cluster to expand to a local electron density, which is below the critical density (i.e., $N_e < N_{cr}$). At times greater than the critical density lifetime (τ_{cr}), laser light absorption will decrease significantly.

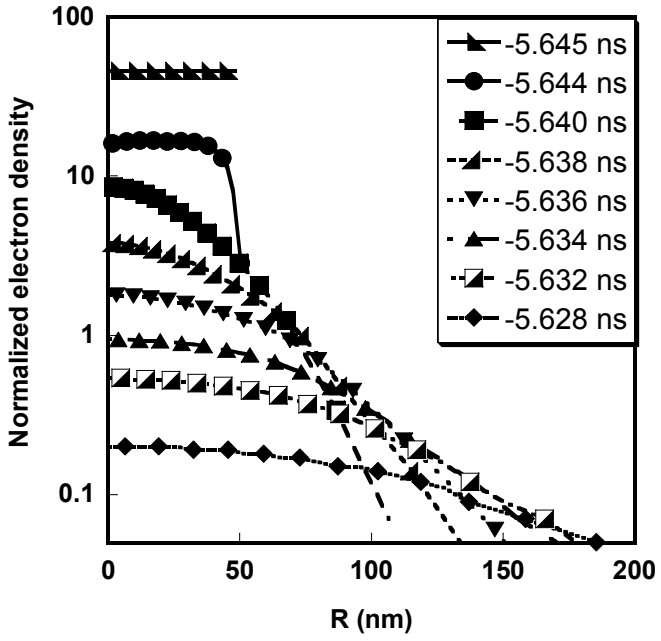

Figure 3.5 (a) Temporal and radial spatial variation of normalized electron density.

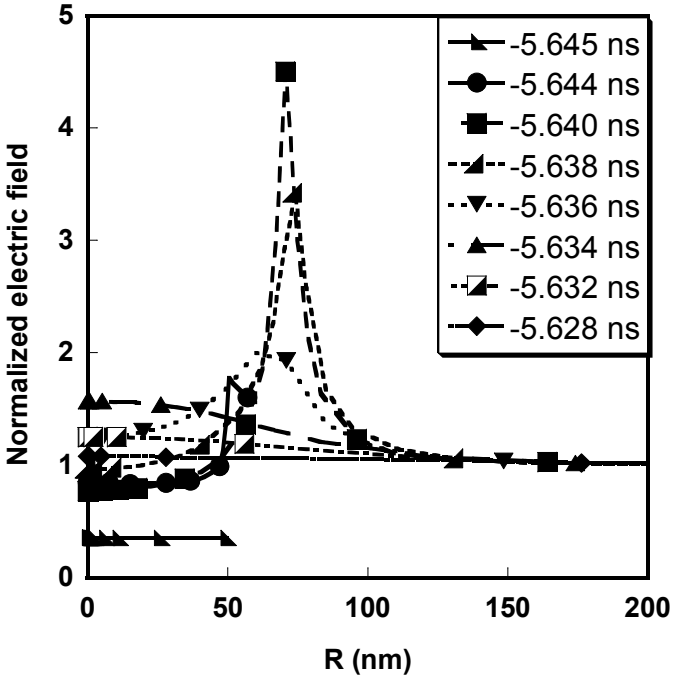

Figure 3.5 (b) Temporal and radial spatial variation of the normalized electric field.

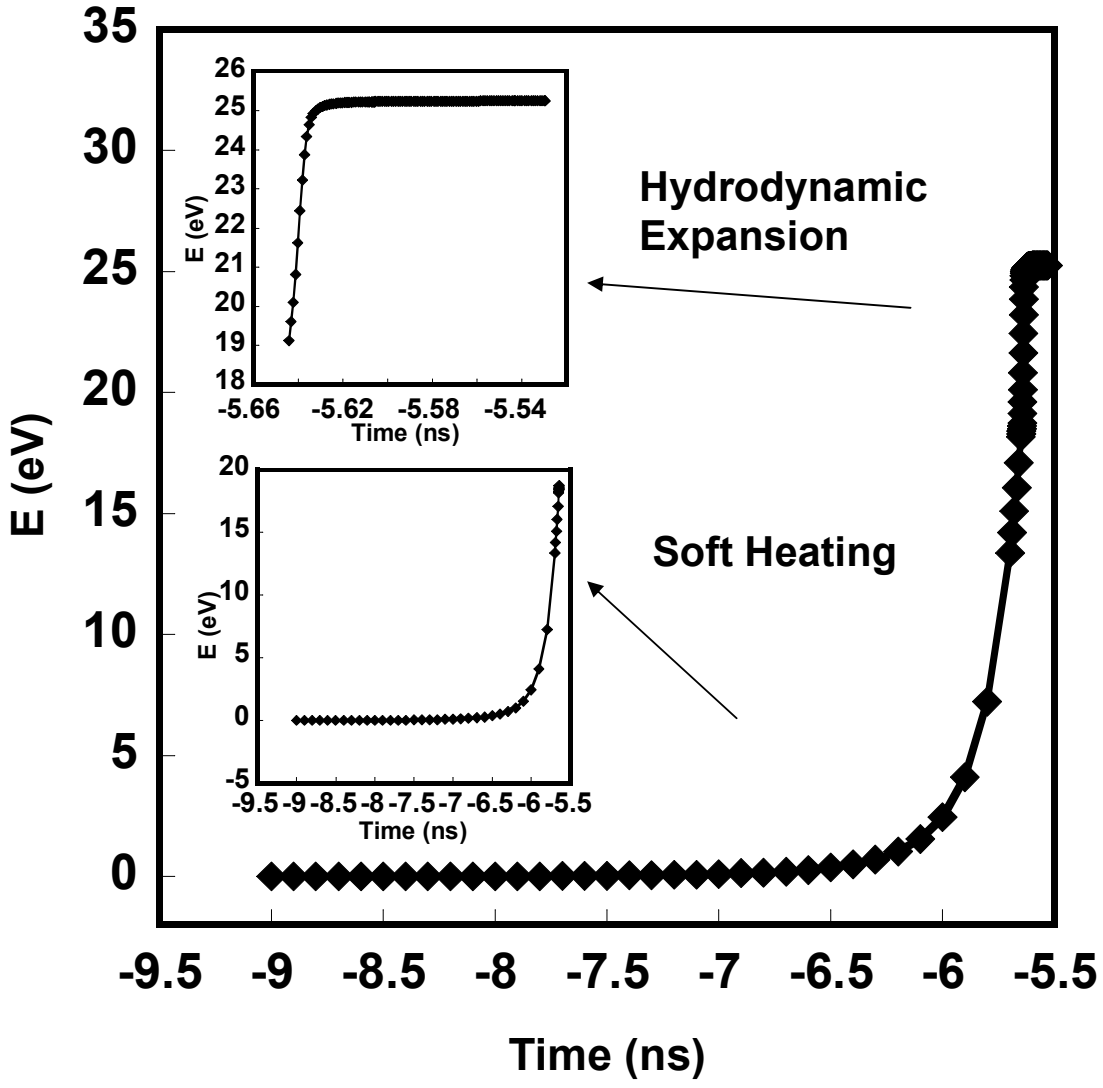

Figure 3.6 Total absolute energy deposited to the particle during the laser interaction.

The results from Figure 3.5 (a) and (b) indicates that the laser-particle interaction occurs over a period of ~ 3ns (from -9 ns to -5.6 ns) for the Gaussian 5ns FWHM laser pulse, and that most of the time is spend to overcome the cohesive energy threshold. On the other hand, if we look at the absolute energy deposited to the particle during the interaction (Figure 3.6), it is clear that although the hydrodynamic plasma expansion occurs over a very short time (~10ps), the energy

deposition rate is much faster (~10^{12} eV/sec) than in the "soft heating" regime (18eV in 3 ns). Figure 3.6 also shows that the energy deposition is completed after the critical density life time, which is consistent with the discussion above.

Thus, in our nanosecond laser pulse, the energy absorption of the particle only takes place during the leading edge of the pulse, and after τ_{cr}, the coupling is no better than in a gas. In other words, the ablation/ionization is over well before a nanosecond laser ever reaches its peak intensity. This observation is qualitatively consistent with previous results for the interaction of the laser pulse (peak intensity >10^{14} W/cm^2) with argon clusters.[86]

As mentioned early, the SPMS can be used to estimate particle size using the predetermined relationship between the ion signal (i.e., the amount of ions detected in the measured mass spectrum) and particle size. However, the formation of energetic ions will affect the transport efficiency through the SPMS time-of-flight tube and therefore sensitivity. In our previous study,[82] we can defined the detection efficiency (*DE*) as

$$\mathrm{DE} = \frac{\text{number of ions detected by SPMS}}{\text{total number of ions}}$$

the ion trajectories in the TOF tube were simulated using SIMION,[88] and the detection efficiency was calculated as a function of initial ion kinetic energy. The result shown in Figure 3.7 demonstrates that the detection efficiency for ions in the SPMS depends strongly on the ion-kinetic energy:

DE (%) (detection efficiency) ~ $E_k^{-0.99}$;

i.e. as the kinetic energy of ions increase, the detection efficiency decreases.

Clearly, the initial kinetic energy of ions plays an important role in the application of SPMS: ions with high kinetic energy are harder to collimate with the extraction fields and as a consequence, both the detection sensitivity, and the ability of quantitatively characterize single nanoparticle are degraded. Thus we are especially interested in the kinetic energy of constituent ions produced from the laser pulse. The remainder of this paper explores the influence of the laser pulse intensity on the kinetic energy of ions produced from the laser-particle interaction, as well as the particle size dependent energetic ion formation.

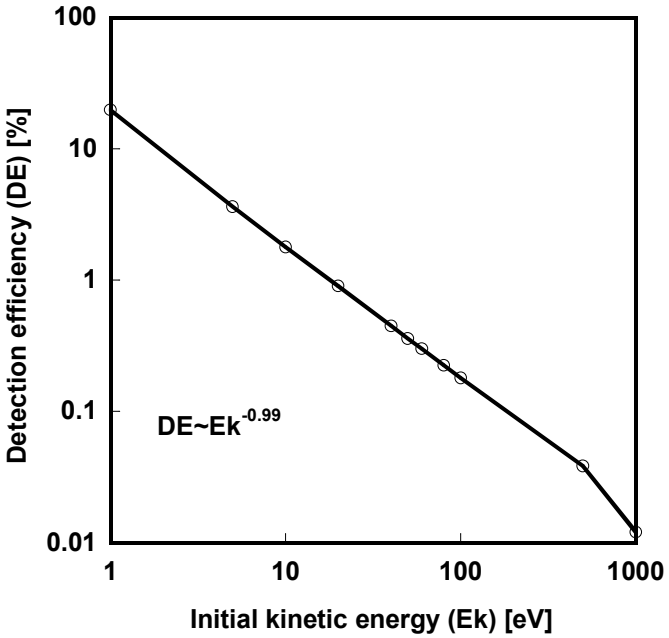

Figure 3.7 Calculated effect of initial kinetic energy on detection efficiency of the SPMS.

The kinetic energy of ions was computed using the velocity profiles obtained from the simulation results. Figure 3.8 (a) shows the kinetic energy (= $1/2mv^2$) profiles as a function of radial distance at various times, for an aluminum particle of initial diameter of 100 nm. Evidently the ions at the surface of the expanding plasma

cloud have the highest kinetic energy. From the practical point of view a bias to higher kinetic energy for the surface atoms will lead to lower detection efficiency as shown in Figure 3.7 and therefore a bias against surface species. We have also plotted the number weighted average kinetic energy (i.e., $E_{k\_mean} = \Sigma E_k(r) * N_i(r) / \Sigma N_i$) where r is the radius and N is the ion number, and its maximum value are plotted against time in Figure 3.8 (b). Note that the kinetic energy increases rapidly initially, but reaches an asymptotic value after ~-5.634 ns. This occurs because most of laser energy is absorbed onto the particle during the leading edge of the pulse till we achieve τ_{cr} (~10 ps).

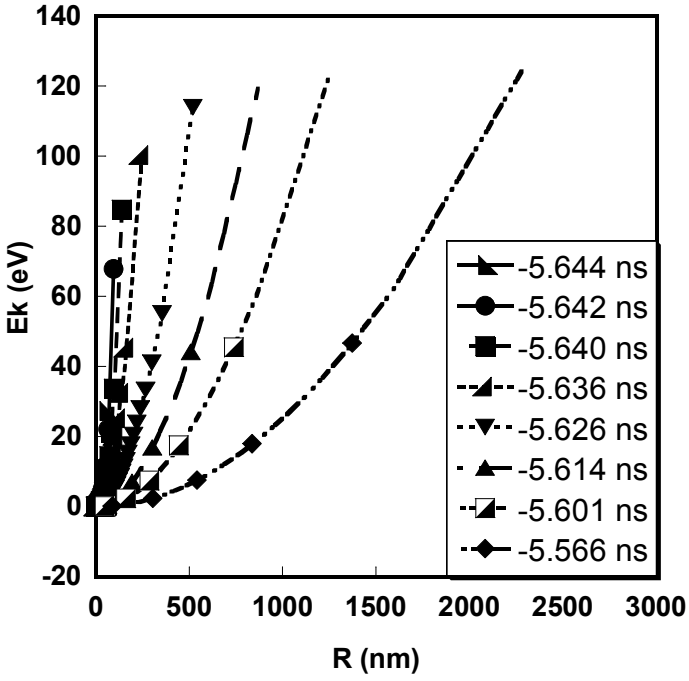

Figure 3.8 (a) Kinetic energy profile as a function of radial distance at various times for an aluminum particle of initial diameter=100 nm.

The hydrodynamic simulation results suggested that most of the laser energy is not deposited into the particle because of the poor coupling between laser pulse and

the plasma. Obviously, for the single particle mass spectrometer, a hot plasma is preferable to ensure complete ionization, which can be achieved by employing a higher laser intensity or absorption efficiency. However, a hotter plasma should produce more energetic ions, which will result in greater ion loss during the transport in the TOF. In other words, too intense a photon flux or too much absorption may decrease the overall ability to quantify SPMS data, by possible species biases in the detection efficiency of ions, while too weak a laser cannot ensure complete conversion of constituent atoms to ions. Ideally one would like to understand where the optimum lies.

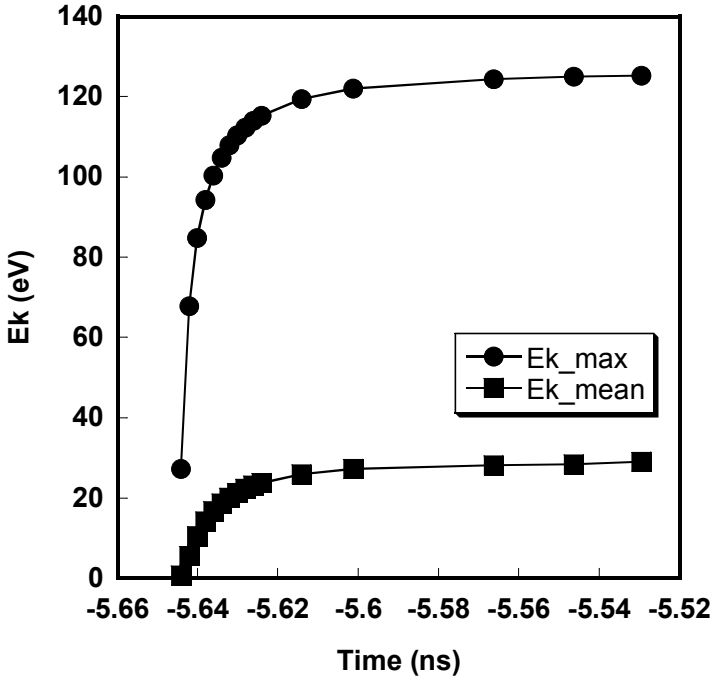

Figure 3.8 (b) Temporal variation of the average and maximum kinetic energy for an aluminum particle of initial diameter =100 nm.

Based on the above discussion, we conducted simulations to investigate ion formation from a 100nm aluminum nanoparticle after their interaction with laser light

of varying pulse widths (10 ps ~ 10 ns). The motivations are based on our previous discussion that indicated that the critical plasma density is achieved well before a nanosecond laser reaches its peak intensity. Furthermore all experimental work on particle mass spectrometry to date, at least to our knowledge has employed nanosecond lasers. To explore the role of pulse width we used the following conditions for our simulation; 10 ps (7.75×10^{13} W/cm^2), 100 ps (7.75×10^{12} W/cm^2), 0.5 ns (1.55×10^{12} W/cm^2), 5 ns (1.55×10^{11} W/cm^2), 10 ns (=7.75×10^{10} W/cm^2), Figure 3.9 plots the number weighted average kinetic energy and average ionization state of ions for different laser intensity. The results show a monotonic increase in both the mean kinetic energy and average charge of ions as the pulse width is decreased. The results indicate that going to a shorter laser pulse creates a much more aggressive laser interaction. If we consider the nano-second laser sources as our base case condition, it is quite clear that a longer pulse laser would be the wrong direction to go to ensure the complete ionization approach. The next question is if pico-second lasers which are readily available offer some advantages. The results suggested that for a pico-second laser, the mean kinetic energy and average ionization state of ions could be very high, such that complete ionization criterion can be guaranteed, however, the higher kinetic energy of ions will result in a low detection efficiency given standard ion optics employed in TOF systems. On the other hand the pico-second laser has the highest likelihood that poor absorbers of surface coated material that might preferentially be blown-off without being ionized may be detected with a shorter pulse laser providing a more aggressive ionization.[89]

The above result invites the question, would a lower pulse energy for pico-second lasers have some advantages for SPMS application. Further simulations for 100 ps and 10 ps pulses were carried out with laser pulse energy of 50 mJ and 10 mJ. As one would expect, the simulations give lower mean ion kinetic energy and average charge of ions with the decrease of laser pulse energy, but in general is seen to be a an insensitive parameter, likely because the absorption time is shorted than the pulse duration in any case. Thus once a threshold energy is achieved the resulting ionization process becomes relatively insensitive to pulse energy. For example, as the laser pulse energy decreases from 100 mJ to 10 mJ, the resulting ions mean kinetic energy decreases by a factor of 1.3 (from 517 eV to 395 eV), and 1.04 (from 20762 eV to 19826 eV) for 100 ps and 10 ps lasers, respectively. This also implies that a pico-second laser with near threshold energy would provide enough ionization with low ion kinetic energy. Simulations on a 10 ps pulse with lower pulse energy, show that the threshold energy is on the order of hundreds of microjoules. So a 1 mJ pulse would give a kinetic energy of 18186 eV while the resulting ions mean kinetic energy of a 0.5 mJ pulse is only 226 eV and the interaction takes place over the whole laser pulse. Further decrease of the pulse energy to 0.1 mJ, results in insufficient energy absorbed to overcome the cohesive energy threshold, and as a result no hydrodynamic plasma formation.

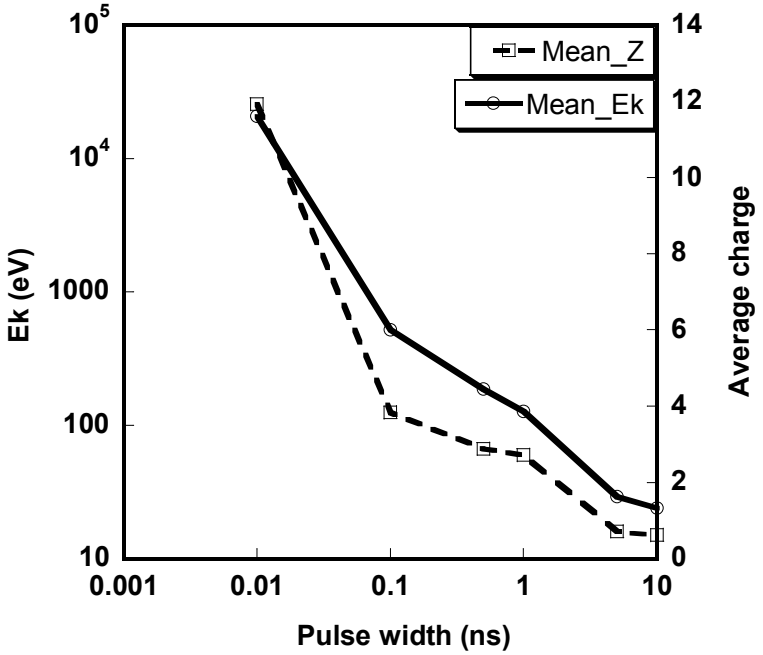

Figure 3.9 Effect of laser pulse width on average kinetic energy and average ionization state for an aluminum particle of initial diameter =100 nm.

The present results suggest that a nano-second laser may in fact provide the optimal laser source, for the present design of time-of-flight optics. However experiments on pico-second laser are warranted. In the latter case, other configurations, such as a high pressure ionization region where the kinetic energy of ions can be absorbed may offer interesting avenues for exploiting pico-second lasers.[90]

To further illustrate the effect of laser pulse width on the laser-particle interaction, the normalized Gaussian laser pulses are plotted in Figure 3.10 (a). For each laser pulse, we also define the temporal regions that correspond to the "soft heating" and hydrodynamic expansion, and the fraction of laser energy absorbed as a function of pulse width plotted in Figure 3.10 (b). Note that in Figure 3.10 (a), we should compare the relative fraction of "soft heating" and hydrodynamic expansion

time in each pulse rather than the absolute interaction time. We can see that the hydrodynamic interaction regime become significantly longer as the laser pulse width is decreased. Considering that the energy absorption during this part of the interaction is much more aggressive, the result shown in Figure 3.10 (a) implies that there is more energy deposited onto the particle for a shorter laser pulse, which is manifested as an increase in ion energy and ionization state. This conclusion is confirmed by the calculation of energy absorption efficiency shown in Figure 3.10 (b), which indicates a monotonic increase in absorption efficiency as the pulse width is decreased.

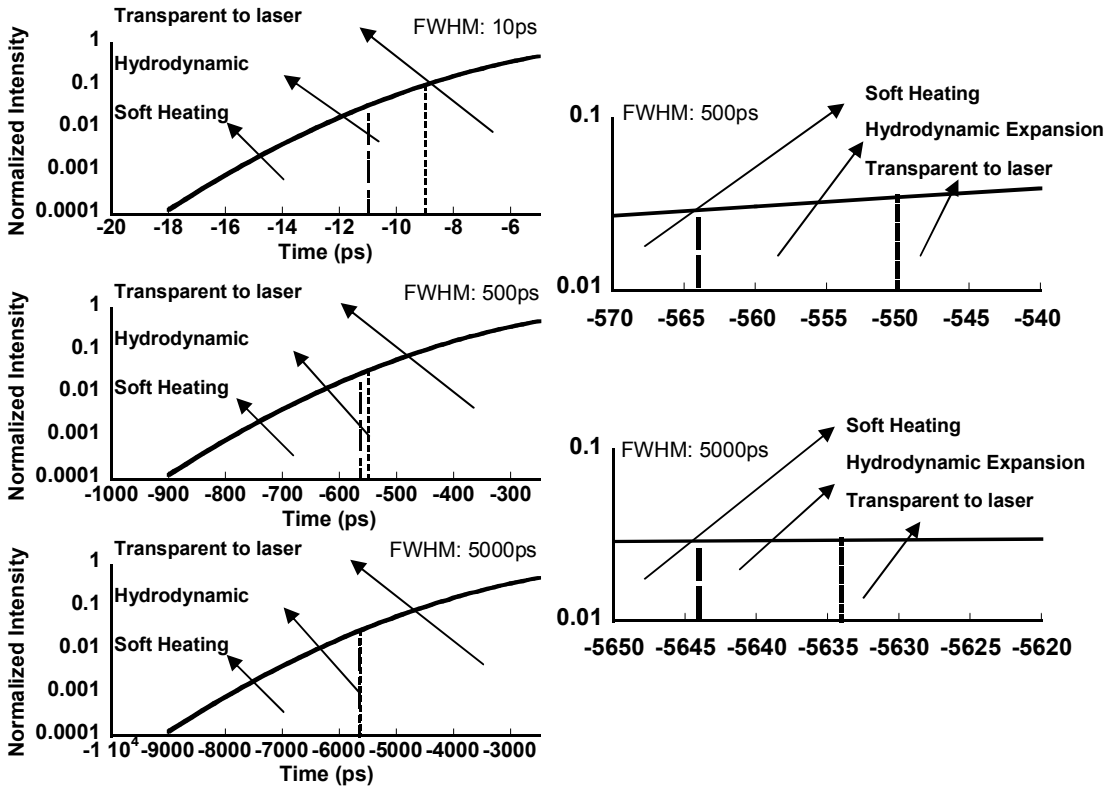

Figure 3.10 (a) Left: Gaussian laser pulses of various width overlayed with the "soft-heating" and hydrodynamic expansion regions for an aluminum particle of initial diameter =100 nm. Right: Detailed view of "soft-heating" and hydrodynamic expansion regions for FWHM 5000ps and FWHM 500ps laser pulses

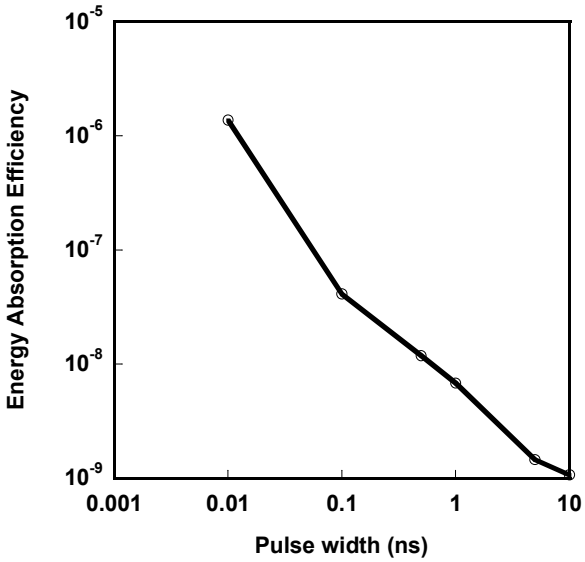

Figure 3.10 (b) Calculated fraction of laser energy absorbed in a 100nm aluminum particle as a function of pulse width.

Next we turn our attention to the effect of particle size on the kinetic energy of ions produced. In our previous work, we hypothesized that the non-linear relationship between the ion signal and particle size observed in our experiment is due to the formation of size-dependent energetic ions.[82] In this work, simulations of laser interactions with particles in size range of 20 ~ 400 nm were carried out and the resulting ions energy were examined to understand their size dependence.

The number weighted average kinetic energy for particles in the 20-400nm range are shown in Figure 3.11. We found that as size increases, the average kinetic energy of ions increases, and for particle size ~100 nm and larger, the kinetic energy follows a power law relationship in particle diameter ($E_k \sim D_p^{1.43}$). One possible explanation for the size-dependent kinetic energy formation is that with increasing particle size, the critical density lifetime increases (i.e., it takes longer for the average density of the larger particle to drop below the critical density), and therefore the particle absorbs energy for a longer period of time. Increased absorption time results

in greater heating, leading to a higher initial kinetic energy and charge state for larger particles.

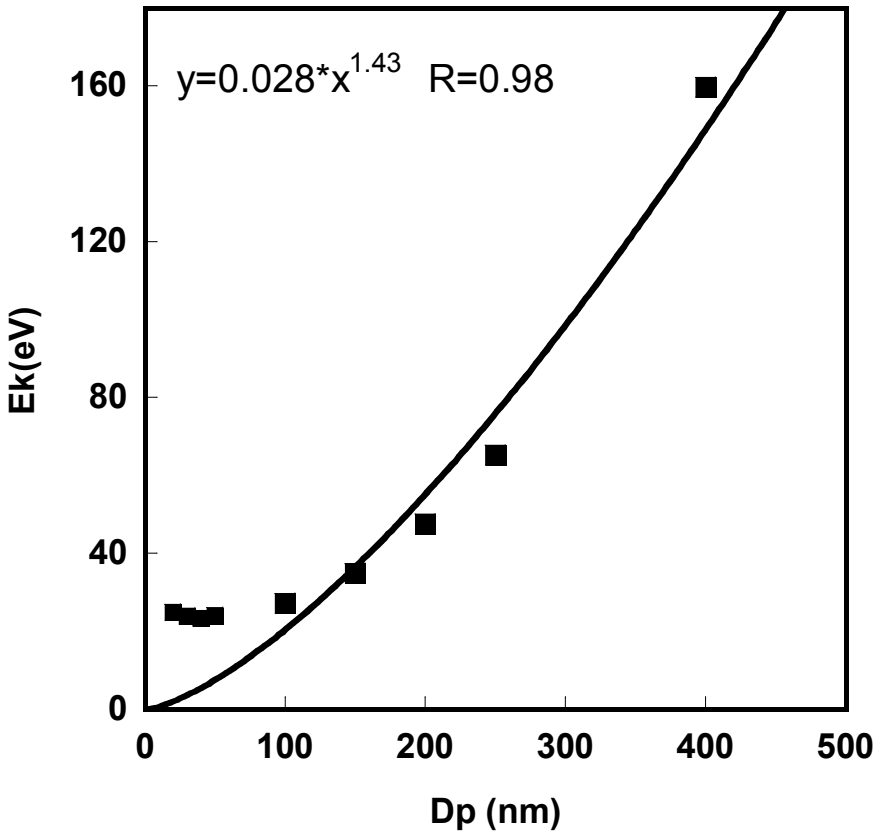

Figure 3.11 Mean kinetic energy of ions as a function of particle diameter.

We are now in a position to compare the simulation results with our experiment. In our previous study, we simulated the detection efficiency (*DE*) of ions traveling through the time-of-flight tube in the single particle mass spectrometry, and showed that the *DE* depends on their initial kinetic energy (E_k), providing the relationship DE (%) ~ $E_k^{-0.99}$.[82] This indicates that *DE* decreases with higher kinetic energy ions. In that study, we hypothesized that the non-linear relationship between ion peak area, and particle size was caused by the more energetic ion formation from

larger particles. Our current simulation results ($E_k \sim D_p^{1.42}$) qualitatively showed that this should be true.

By employing the relationship ($E_k \sim D_p^{1.43}$) from the current simulation results, and the DE (%) ~ $E_k^{-0.99}$ from the previous ion trajectory simulation, we obtain DE (%) ~ $D_p^{-1.42}$. Since the DE is related to the integrated peak area in a single particle mass spectrum by the equation of

$$Peak\ Area = C \times DE \times total\ number\ of\ ions$$

where C is the proportionality constant between detector signal (peak area) and the number of detected ions. Thus, we can obtained the relationship between the integrated peak area and particle size, giving peak area ~ $D_p^{1.58}$, or peak area$^{1/3}$ ~ $D_p^{0.53}$, and the proportionality constant C can also be determined by fitting the above relation to the experimental data of aluminum. Now we compare the above relationship (peak area$^{1/3}$ ~ $D_p^{0.53}$) with experimental measurements with the single particle mass spectrometer for aluminum particles. The comparisons shown in Figure 3.12 clearly indicate that the simulation correctly captures the basic trends observed in the experiment. The power dependence from the theoretical calculations for aluminum particles is 0.53, while the experimental values are 0.58. The experimental results for a variety of materials are also shown in Figure 3.12. The power dependence between peak area$^{1/3}$ and particle size is 0.45, 0.30, for sodium chloride and silver nitrate, respectively. Based on the data presented in Figure 3.12 it is quite reasonable to assume the proportionality constant C between signal and number of ions detected is material independent, so that with the value obtained for aluminum, we can estimate the KE of other materials. Our estimate yields a value for mean KE

of about 5.13 eV and 19.3 eV for ions generated from a 100 nm sodium chloride and silver nitrate particle, respectively. Compared to the mean *KE* of 29 eV for 100 nm aluminum, our experimental results suggest that even though particles of different materials would have different *KE*'s, the MS signals are remarkably similar. This should be expected because the experimental result is mass based, (peak area corresponding to mass of particle) which is $\sim Dp^3$. So the peak area obtained from experiment is less sensitive to *Dp*, and hence not as sensitive to *KE*. In fact, this is one of the potential advantages of using SPMS to determine particle size: with a pre-determined power dependence, we can quantitatively determine particle size within a reasonable accuracy regardless of particle composition.

It is also interesting to note that for smaller particles, there is a discrepancy between the average kinetic energy and the power law relationship, $E_k \sim D_p^{1.43}$, obtained above, the kinetic energy for particles in small size range have a relative higher value. The high kinetic energy suggests a relatively more aggressive energy absorption and particle ionization for a smaller particle. This result is consistent with a recent experimental observation by Wang et al. who developed a nanoaerosol mass spectrometer (NAMS) using the complete ionization technique.[90] Quantitative chemical characterization for a particle with diameter ~ 10 nm was achieved with a quadrupole ion guide and quadrupole ion trap system. In their work, multiple charged ions peaks (+4) were frequently observed in the spectra, which imply highly ionization states were achieved for particle sizes < ~10 nm.

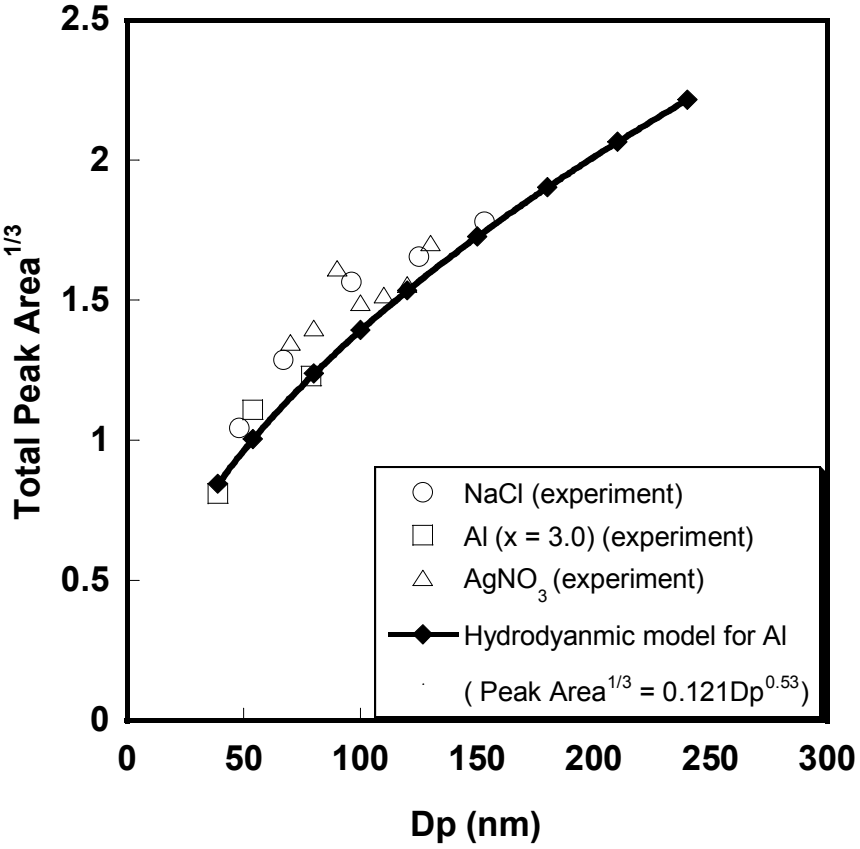

Figure 3.12 Comparison of the relationship between ion peak area and particle size from simulation results, and experimentally determined by the single particle mass spectrometer.

3.5 Conclusions

The objective of this chapter was to understand pulsed laser interactions with small particles as it applies to the implementation and quantification of single particle mass spectrometry. In this study we applied a one-dimensional hydrodynamic model to determine the characteristic behavior of ions produced from aluminum nanoparticles as a result of interaction with a strong laser pulse. During the early stages of interaction, the particle experiences a "soft heating" regime to overcome the cohesive energy of solid. Subsequently, the laser-particle interaction transitions to a

resonant absorption and hydrodynamic plasma expansion. The effect of laser parameters such as pulse width, energy, and particle size were investigated in this work.

Our simulation results showed that the ablation/ionization process is finished well before the laser ever reaches its peak intensity. We found that shorter laser pulses lead to greater energy absorption and produce a more intense plasma, which will result in higher ionization state and higher ion kinetic energy. However the higher kinetic energy of the shorter pulse lasers will likely lead to a significantly degraded detection efficiency for ions in traditional TOF ion optics. The simulations suggested that nano-second lasers may in-fact provide an optimized solution for SPMS application.

We also found particle size-dependent energetic ions are formed from the laser-particle interaction, and the kinetic energy of ions is proportional to the particle size with a power law relationship ($E_k \sim D_p^{1.42}$). This result is show to be consistent with our experimental observation, and suggest that particle size-dependent energetic ions led to the power-law relationship between peak area and particle size observed in a single particle mass spectrometer.

Chapter 4

Component and Morphology Biases on Quantifying the Composition of Nanoparticles Using Single Particle Mass Spectrometry

4.1 Introduction

Single Particle Mass Spectrometry has been widely studied and used in the past decade as a tool for real-time elemental characterization of individual particles.[5, 30, 32, 33, 91-94] In this method, an aerosol sample is continuously introduced into the ion source region of a mass spectrometer using a high throughput source such as an aerodynamic lens system. Subsequent, laser ablation/ionization and Time-of-Flight (TOF) analysis are used to obtain single particle mass spectra. The ultimate goal of this method is to quantitatively characterize the size, elemental composition, and gas-particle reactivity of aerosols.[4, 5, 91, 92]

In principle, the mass spectrum should provide quantitative information about the particle composition and size, however, due to the complexity of the transport and ion-generation/detection, quantitative interpretation is normally not achieved. In their study of the oxidation state of chromium in aerosol particles, Neaubauer et al. showed that the distribution of ions in the corresponding mass spectra is influenced by many factors including particle size, composition, laser irradiance, wavelength and mass spectrometer operating conditions.[95] Moreover, the study of atmospheric aerosols by Zelenyuk et al. suggests that there are significant limitations in laser ablation technique, namely the highly nonlinear nature of the ablation process, which makes quantitative calibration of mass spectra extremely difficult to realize.[91] They also

suggested that the mass spectrum was dominated with the low ionization potential species. Reilly et al. have studied the charge-transfer-induced matrix effects in the laser ablation process for micron-sized environmental aerosols.[96] Their results suggest that for multi-component particles, the species with low ionization potential is easily detected in most matrices, and species with high ionization potential may only be detected in matrices with higher ionization potential. Ge et al. have used single particle mass spectrometry to study micron-sized multi-component particles with different chemical morphology.[97] Their results show that particles were partially vaporized/ionized during the ion formation process, so that only the surface layer of the particle can be explored. They further studied the size and composition biases for ultrafine particles, and showed that the ion yields vary with different species, and the detection efficiency is a strong function of size and composition of nanoparticle due to the inlet transmission characteristics and the intrinsic nature of the laser-particle interaction.[98, 99]

These results suggest that the detection sensitivity is strongly biased with species and the spectrometer operating condition. Thus, to achieve the goal of quantitative characterization of individual aerosol particles using single-particle mass spectrometry, it is becomes imperative that we understand the sensitivity biases in the spectrum. Efforts to overcome the limitation of laser ablation/ionization mass spectrometry, include a two-laser approach used by several researchers to optimize the vaporization and ionization steps.[100-102] In another approach Reents et al. used a highly focused laser to create an extremely hot plasma, such that all elements are converted to positive ions even for electronegative species.[32] This approach has

been used by other research groups as well. Wang et al. recently developed a nanoaerosol mass spectrometer (NAMS) that uses this complete ionization technique. Quantitative chemical characterization for particle with diameter ~ 10 nm was achieved with a quadrupole ion guide and quadrupole ion trap system.[90] A similar technique of using a very high fluency laser ($>10^{11}$ W/m^2) beam has also been employed in our group, and in our previous studies quantification of composition and size for various nanoparticles have been achieved with reasonable accuracy.[5, 82]

In the preceding chapter, we employed a hydrodynamic model to investigate the characteristic behavior of ions produced from the interaction of a high energy laser pulse with nanoparticles.[83] The simulation results are quantitatively consistent with experimental observed power law relationship between particle size and MS signal. The model present in the previous chapter is focused on mono atomic particle and can provide insightful information for future experimental development on SPMS. In this chapter, we take one step further and examine the effects of complex particle composition and morphology on the quantification of SPMS using complete ionization technique. We conducted experimental work and show that although this complete ionization technique can accurately characterize single component particles, the situation becomes more complex when one is dealing with multi-component particles whose composition is not homogeneous within the particle. Essentially we want to explore the relationship between how the elemental components are mixed within a particle, and the resulting mass spectrum. The study is conducted by generating coated and composite particles, and correlating the results to the relative absorptivity of the coating material relative to the core. To explore and explain these

effects, several different types of composite particles were studied in this work: (i) aluminum particles coated with sodium chloride, (ii) aluminum oxide particles coated with sodium chloride, (iii) aluminum oxide and sodium chloride matrix particles, and (iv) aluminum oxide particles coated with nickel. A summary of the morphology and component properties of testing particles are shown in Table 4.1. We show that the nature by which the constituents of the particle are assembled, and the relative absorptivity of the constituent materials to the laser, has a profound influence on the resulting mass spectrum. The mass spectra of these particles were evaluated to understand the component/morphology biases of the spectrometer. To our knowledge, the work reported here is the first finding on the composition/morphology biases for single particle mass spectrometer (SPMS) using the complete laser ionization technique. We also develop a qualitative explanation for the observed behavior. The work present in this chapter was done along with Dr. Ashish Rai and has been publish by our group.[89]

Table 4.1 Summary of particle morphology and component properties

Particle component	Particle morphology	Component properties		
		Core	Shell	
Sodium chloride	Single component	N.A.	N.A.	Fig.4.3
Aluminum/Sodium chloride	Core-Shell	Absorbing (Al)	Transparent (NaCl)	Fig.4.4
Aluminum oxide/Sodium chloride	Core-Shell	Transparent (Al2O3)	Transparent (NaCl)	Fig.4.5
Aluminum oxide/Sodium chloride	matrix	N.A.	N.A.	Fig.4.6
Aluminum oxide/Nickel	Core-Shell	Transparent (Al2O3)	Absorbing (Ni)	Fig.4.8
Aluminum/Carbon	Core-Shell	Absorbing (Al)	Absorbing (C)	Fig.4.9

4.2 Experimental

4.2.1 Single Particle Mass Spectrometer (SPMS)

The single-particle mass spectrometer used in this study is same as the one described in chapter 3. It consists of an aerodynamic lens inlet, a three-stage differential pumping system, a free-firing dissociation/ionization laser and optics system, a linear time-of-flight (TOF) tube with a cylindrical Einzel lens, and data acquisition system.[5, 82] The schematic of SPMS is the same as shown in Figure 3.1 and re-plotted here in Figure 4.1. The aerodynamic lens inlet is employed to produce a narrow collimated beam of particles that can be injected with high transport efficiency through differentially pumped chambers to the ionization region. The pressure in the ionization chamber which houses the time of flight tube is ~6×10^{-7} Torr when the aerosol inlet is open. The laser used in this system is a frequency-doubled Nd: YAG operated at 10 Hz in the internal Q-switch mode. The laser energy measured before the laser entrance window of the mass spectrometer was ~100 mJ/pulse, was focused with an in-chamber mounted 38 mm focal length focusing lens, to give a ~0.3 mm diameter beam. The laser power density of the 5 ns pulse at the focal point, is estimated to be approximately ~10^{11} W/cm^2. Positive ions formed during ionization of particle are accelerated along ~1 m long linear TOF tube, and are detected by a microchannel plate (MCP) detector.

4.2.2 Generation of Test Nanoparticles

The schematic of the experimental setup used to generated test particles is shown in Figure 4.2. Polydisperse droplets were produced from an atomizer that

contained a solution or suspension of known composition. Aerosol dryers filled with dry silica gel were used to control the water content of the test particles coming out of the atomizer. Subsequently, the particle stream was passed though a heated flow tube with a heated length of 30 cm, and then delivered to the SPMS inlet.

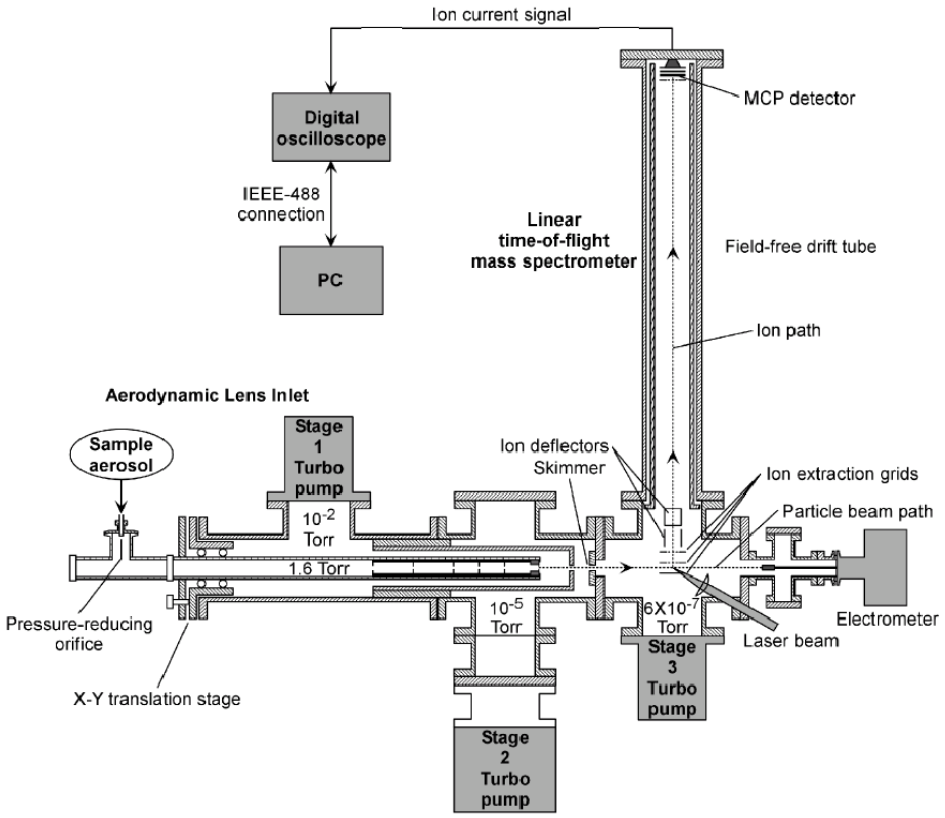

Figure 4.1 Schematic of single particle mass spectrometer (SPMS).

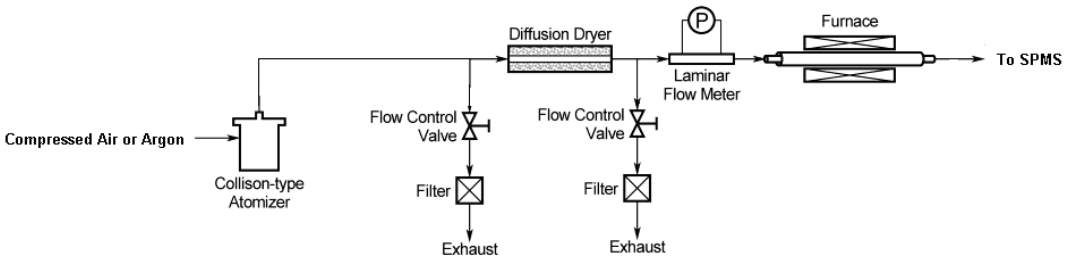

Figure 4.2 Schematic of the particle generation system.

This system was used to generate multi-component particles with different morphologies. Commercially available aluminum nanopowder from Aveka Inc. with primary particle size of 50 nm was mixed with NaCl and was dispersed in 100 mL DI water and atomized. After the removal of the solvent (water) by diffusion drying, salt coated aluminum resulted as verified by TEM. Aluminum oxide coated with NaCl was obtained in a similar way by dispersing aluminum oxide and NaCl in DI water. The aluminum oxide was first generated by spray pyrolysis of aluminum nitrate aerosols in the tube furnace at a temperature of 500 ^{o}C, and collected on a Millipore filter. Nanoparticles containing a matrix of Al_2O_3/NaCl were formed using an approach presented in our previous work.[103] A solution of aluminum nitrate and NaCl in DI water was atomized and passed through a tube furnace at 500 ^{o}C to decompose the aluminum nitrate to aluminum oxide. This resulted in the formation of a matrix of Al_2O_3/NaCl particle. To obtain aluminum oxide particles coated with nickel, aluminum oxide and nickel nitrate were dispersed in a solvent of 30% ethanol and 70% DI water and were aerosolized. This aerosol stream was then heated to a temperature of 900 ^{o}C in a tube furnace. At this temperature, nickel nitrate decomposes to nickel metal, and forms a coating on the aluminum oxide particles.[104]

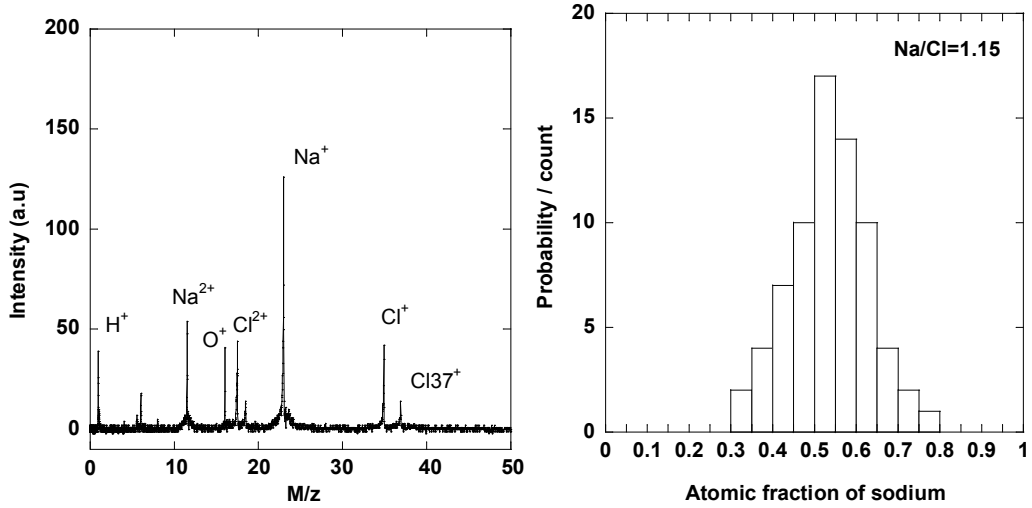

(a) (b)

Figure 4.3 (a) Typical mass spectrum of pure NaCl particles (b) probability distribution of measured stoichiometry ratios for 70 NaCl Particles

4.3 Results and Discussion

In our prior work, we employed a highly focused laser beam which enabled us to achieve high ionization for all elements in a single particle, enabling us to determine the elemental stoichiometry to within 15%.[5, 82] An example of a typical mass spectrum for a single sodium chloride particle is shown in Figure 4.3 (a). Figure 4.3 (b) presents the resulting probability distribution of measured stoichiometric ratios for 70 NaCl Particles. Considering the very large difference in the ionization potentials of Na and Cl, the results are an indication of the robustness of the quantitative nature of the total ionization method.

However these results beg the question as to whether it matters how the components are arranged within the particle. The most obvious controllable morphology is a coated particle. We begin with Al/Al_2O_3 particles coated with NaCl. An example of a typical mass spectrum for aluminum particle coated with NaCl is

shown in Figure 4.4 (a). The spectrum shown in the figure is for a coated particle which was obtained by aerosolizing a mixture of aluminum and sodium chloride such that the mol ratio of aluminum, $X_{Al} = 0.95$ ($X_{Al} = m_{Al}/(m_{Al} + m_{NaCl})$). A point of note is that the mass spectrum shows an abnormal behavior with strong peaks for Al and Na, but the absence of any chlorine peak. This is unlike the spectrum of pure salt particle (Figure 4.3 (a)), in which chlorine cations can be easily observed. This particular particle consists of a relatively large aluminum core with a small salt coating, however the sodium ion intensity is larger then the more abundant aluminum. Figure 4.4 (b) shows the variation of elemental composition as the mol fraction of aluminum is varied in the suspension. The relative peak areas of Al/Al+Na are plotted versus relative mol concentration of elemental aluminum X_{Al} in the suspension. Each data point is an average of 100 single particle mass spectrums. An ideal relationship should be a straight line with slope of 1 passing through the origin. What we observe however is that the Al/(Na+Al) ratio is much lower than the theoretical value at all mole fractions of aluminum. Additionally, no Cl signal was seen in any spectra, even at high salt concentration.

Similar experiments were repeated for aluminum oxide particles coated with NaCl. The mass spectrum collected for aluminum oxide particles coated with NaCl also shows a similar behavior. Figure 4.5 (a) shows a typical spectrum for an aluminum oxide nanoparticle coated with sodium chloride. This spectrum was collected for a particle which was formed by aerosolizing a suspension with mole fraction of elemental aluminum, $X_{Al} = 0.90$ ($X_{Al} = 2m_{Al_2O_3}/(2m_{Al_2O_3} + m_{NaCl})$). An important point to note from this figure is that although we do observe multiply

charged ions of aluminum (M/z = 13.5) and oxygen (M/z = 8), which would seem to indicate roust plasma formation, no chlorine peak was observed. The small N peak (M/z = 14) comes from the uncompleted decomposition of aluminum nitrate which was used to form the aluminum oxide particles. We also looked at the variation of elemental composition as measured by the SPMS by varying the elemental aluminum mole fraction, and these results are plotted in Figure 5 (b)). It can be seen that in this case as well, we are overestimating the sodium content in the multi-component particle, similar to the previous case of aluminum coated with NaCl.

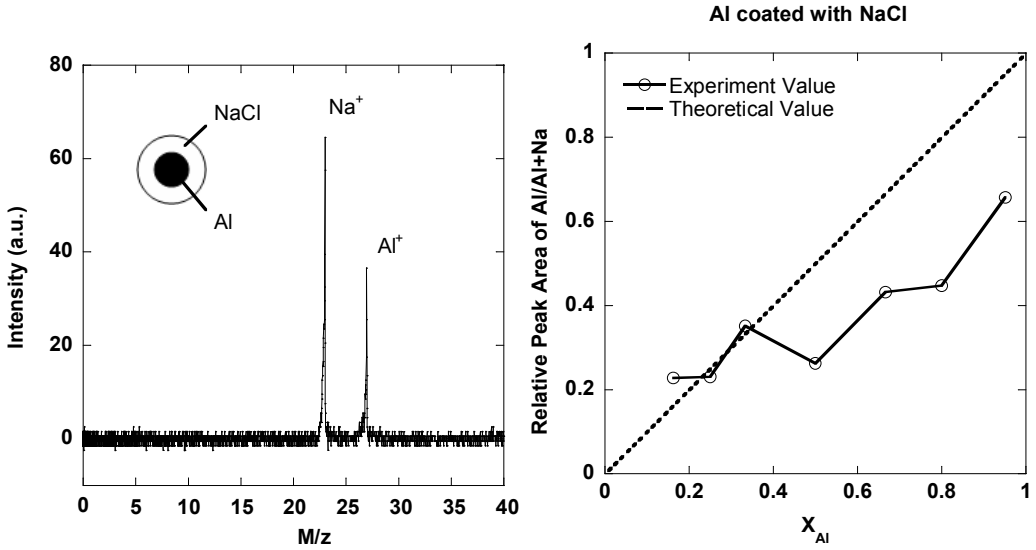

(a) (b)

Figure 4.4 (a) Typical mass spectrum of aluminum coated with NaCl (Aluminum elemental mol fraction of $X_{Al} = 0.95$) (b) Relative aluminum elemental mol fraction for aluminum particles coated with NaCl

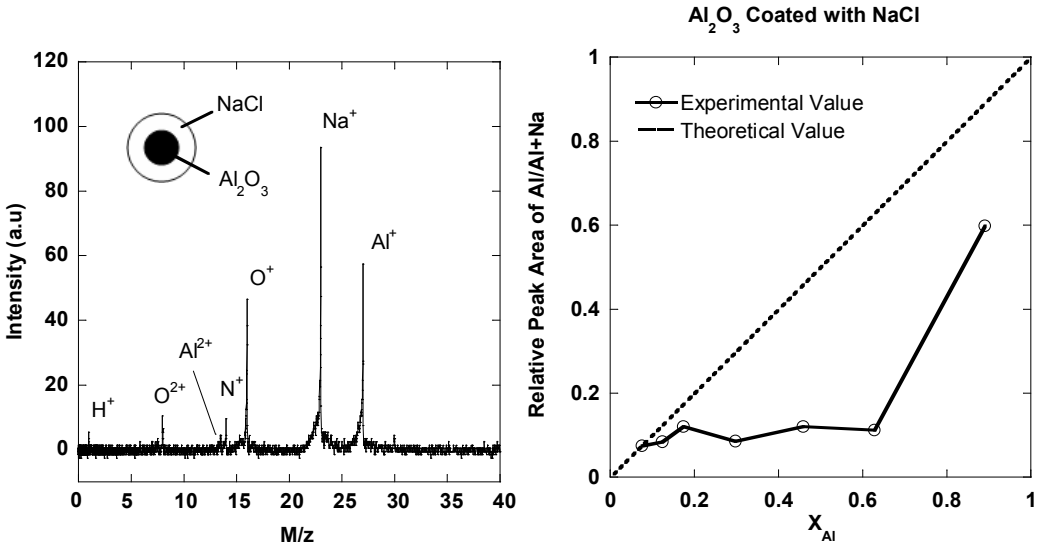

(a) (b)

Figure 4.5 (a) Typical mass spectrum of aluminum oxide coated with NaCl with aluminum elemental mol fraction of $X_{Al} = 0.90$ (b) Relative aluminum elemental mol fraction measurements for aluminum oxide particles coated with NaCl

However a quite different result is obtained if homogeneous particles of the components are prepared. Figure 4.6 (a) shows a spectrum obtained at $X_{Al} = 0.25$, which clearly shows that all the elements including Cl are observed in the spectrum, and multiple charged ion peaks suggest very aggressive plasma formation, and laser particle interaction. There does however seem to be a bias against Cl cation formation at high mole fraction of Al. A plot of the variation of relative elemental composition with change in elemental aluminum mole fraction is shown in Figure 4.6 (b). The plot shows that the measurement of the Al/Na ratio is considerably improved over that seen for the salt coated aluminum oxide (see Figure 4.5 (b)). In this plot we can see that the measured elemental ratio for aluminum and sodium matches closely to the theoretical value at all mole fractions of aluminum. However, unlike the pure salt case, the Na/Cl ratio is much larger than unity. Although we see chlorine in the spectrum, it is relatively weak as compared to the signals from other species.

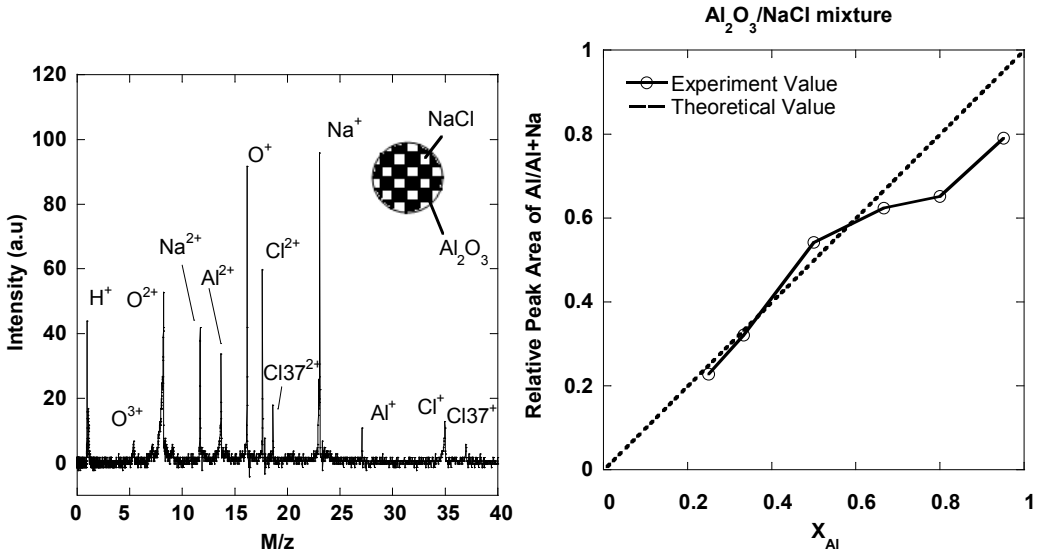

Figure 4.6 (a) Typical mass spectrum for aluminum oxide and NaCl matrix particle with aluminum elemental mol fraction of $X_{Al} = 0.25$ (b) Relative aluminum elemental mol fraction measurements for aluminum oxide and NaCl matrix particles.

As mentioned previously, we can determine the relative elemental concentration to within 15% for single-component particles.[5, 82] However, for particles with the core-shell structure, the measured composition shows considerable error. In the core-shell structure discussed above, Na is higher than the theoretical value, so that the measured mol ratio of Al/Al+Na is lower than the true value. On the other hand, for homogeneously mixed Al_2O_3/NaCl particles, we observe that the results show relatively good agreement

Our next task then is to attempt to resolve these observations. A particle undergoes three processes after it is delivered into the SPMS inlet: initially the particle is transmitted to the ion source region through an aerodynamic lens inlet. Subsequently in the ion source region, the particle is ionized by the focused laser beam. Finally these ions are extracted by an electrical field and are transported through the TOF region, and reach the detector. Kane et al. showed that the particle

transmission efficiency through the aerodynamic lens is biased by particle shape and size.[98] However, it is reasonable to assume that transport biases would not be significant for a homogeneous vs. a core shell structure, nor would they cause the errors in the measurement of elemental ratio for those particles that are ablated/ionized.

The other two possibilities are: (i) the ion formation/recombination process for these multi-component particles is component/morphology biased even at such high laser fluences. (ii) Ions are lost during transport in the TOF region of the mass spectrometer, and some species are selectively lost (e.g. ions with very high energy).

In our previous work, we evaluated ions transport losses in the TOF tube, and a model was developed to describe the preferential loss of the high kinetic energy ions.[82] This work indicated that one could, through the use of an Einzel lens system significantly increase the transmission (detection) efficiency of high kinetic energy ions. To explore this as a possible explanation of our observation we repeated the experiments with an Einzel lens voltage varied from 0~4000V. One such result is shown in Figure 4.7, for the salt coated aluminum oxide particles. While the use of the lens did change ion intensity, indicating that we could use the lens to transport more ions down the flight tube, Figure 4.7 clearly shows that the lens has no effect on the relative ion signal. This result would seem to indicate fairly convincingly that whatever the ion energy distribution might be, that all species would seem to have a similar distribution as produced in the laser induced plasma, and we should expect no transport biases in the flight tube.

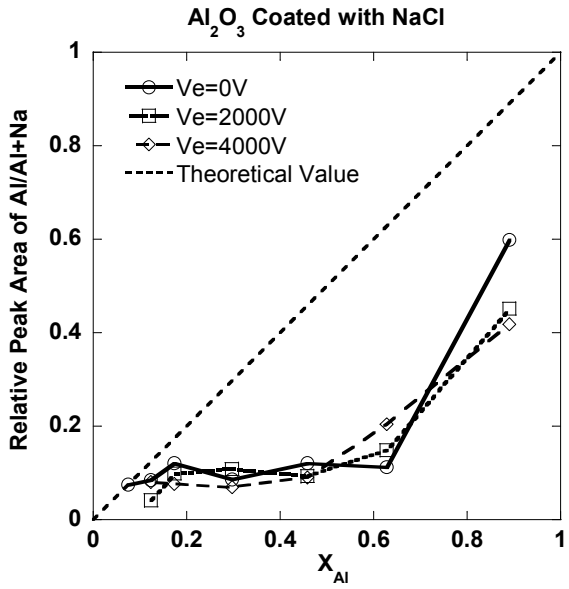

Figure 4.7 Effect of Einzel lens on relative aluminum elemental mol fraction measurements for aluminum oxide particles coated with NaCl.

Based on the above observations, the most likely explanation of the experimental results would involve the interaction between particle and laser pulse. Considerable research has been directed to investigate the mechanism of the laser-particle interactions[36, 105, 106] which involves the process of energy absorption, particle heating, melting/evaporation, and subsequent fragmentation/ionization of the particle. These highly nonlinear processes are very complex, and are influenced by both the laser beam parameters, and the particle optical/thermal properties. Clearly particles with different morphology, and/or composition will have different optical/thermal properties, which may influence the interaction process, and thus the resulting ion distribution. In the previous chapter, we applied a hydrodynamic model to explain the laser-particle interaction.[36, 83, 86] For the laser intensity used in this study (~10^{11} W/cm^2), the particle is first heated by the laser beam, and subsequently

ionized by a hydrodynamically controlled ionization process. The heating rate of the particle is given by

$$Heating\ rate\ =\ \frac{1}{2}\omega\,\mathrm{Im}(\gamma)\left|E\right|^2 \tag{4.1}$$

where ω is laser frequency, E is the electrical field generated by the laser beam and $\mathrm{Im}(\gamma)$ is the imaginary part of particle polarizability, which is given by

$$\mathrm{Im}(\gamma)=\frac{6a^3nk}{\left|N\right|^4+4(n^2-k^2)+4} \tag{4.2}$$

where a is the particle radius and $N = n + ik$ is the complex refractive index of particle. For the laser frequency used in this work, aluminum has a complex refractive index of $N = 0.15 + 5.35i$, and aluminum oxide is $N = 1.77 + 10^{-6}i$ indicating that aluminum is a much stronger absorber than aluminum oxide. For NaCl we found that $N = 1.54 + 0i$, which indicates that NaCl is virtually transparent to the laser beam. When we have pure salt, presumably the threshold before heating and ionization takes place is much higher than that for pure aluminum. For aluminum particles coated with sodium chloride, the coating is, relative to the core transparent to the laser beam, and thus the laser beam should first interact with the core of the coated particles. This could cause local heating and subsequent plasma formation of the core, with energy conduction to the shell. In this case our observed results are consistent with the idea that the heating from the core is sufficient to just blow the shell-off but not intense enough to cause significant ionization of the shell material as evidenced by the lack of signal for Cl. We will defer for the moment an explanation for why the Na signal is actually higher than expected relative to Al.

For aluminum oxide particles coated with NaCl, although we believe that aluminum oxide can absorb more laser energy during the laser-particle interaction as compared to NaCl, the above analysis is hard to validate because the imaginary part of the refractive index for Al_2O_3 is also small. Thus it may take a longer time for the Al_2O_3 core to absorb sufficient energy to create a plasma. During this heating period, their is also thermal conduction between the Al_2O_3 core and the NaCl coating due to the temperature inhomogeneity between the two phases.

We begin with a comparison of the characteristic times for laser heating vs. intra-particle conduction. The characteristic time for conduction τ_s can be estimated as:

$$\tau_s = \frac{a^2 \rho C_V}{\chi} \tag{4.3}$$

where χ is the thermal conductivity of the material, ρ is the density of the material and C_v is the specific heat of the material.

In the hydrodynamic model, it was demonstrated that the laser energy absorption is enhanced near the critical density surface.[36, 86] The critical electron density is given by

$$N_{cr} = m\omega^2 / 4\pi e^2 \tag{4.4}$$

Below this density, the plasma becomes transparent to the laser beam and does not absorb any further energy. In our previous chapter, we have shown that during the laser-particle interaction, the electron density profile in the plasma is non-uniform, and one can find a critical density surface where resonant laser energy absorption occurs. The electric field is also significantly enhanced in the regions close to the critical density surface. The time to achieve the resonant laser absorption in the

plasma can be defined as the critical density lifetime τ_{cr} after which the plasma no longer absorbs energy from the laser. The critical density life time τ_{cr} is given by[86]

$$\tau_{cr} = \frac{a}{c_s}\left(\frac{N_{e0}}{N_{cr}}\right)^{1/3} \tag{4.5}$$

where c_s is the plasma sound speed. For plasma temperatures of about 10 electron volts, c_s is estimated to be $\sim 3.6\times10^4$ m/s. N_{e0} is the initial electron density, $N_{cr} = m_e\omega^2/4\pi e^2$ is the critical density, and N_{e0}/N_{cr} is of the order of 10.

For a 100 nm diameter particle, we calculate the characteristic times for the two processes. For aluminum oxide $\tau_s \sim 10^{-8}$ *s* and $\tau_{cr} \sim 10^{-12}$ *s*, and for aluminum they are $\tau_s \sim 10^{-11}$ *s* and $\tau_{cr} \sim 10^{-12}$ *s*. The comparison between the two time scales suggests that the energy absorption by the core is fast relative to thermal conduction, and particularly so for the aluminum oxide coated case. So, for aluminum oxide particles with a NaCl coating, the core will absorb energy and reach the critical point before it can conduct the energy to the shell. This is consistent with our thinking that having a transparent medium as the shell will result in poor coupling of the laser energy into the shell and a weak plasma formation. In other words there exists a temperature gradient within the particle.

It is also interesting to note that at small X_{Al}, the composition of the particle is primarily NaCl with a small core of aluminum or aluminum oxide. So one would expect that the spectra obtained are similar to the spectra from pure salt particles. In fact the experimental observations imply that even a small change in the composition and structure of particles may influence the laser-particle interaction and may result in different ion distribution.

In contrast with the transparent coating, if the particle is coated with a light absorbing material, one would expect the laser to preferentially initially interact with the material on the shell. A significant difference for this morphology is that, even as the shell blows off as a dense plasma, the core can still be vaporized/ionized by the laser, although it might occur slightly delayed in time. As a consequence, the spectrum should show all the species present in the particle. Experiments were conducted to evaluate a more transparent material coated with a light absorbing material using aluminum oxide particles coated with nickel as a model system. Figure 4.8 (a) shows a typical spectrum obtained at mole fraction of aluminum, $X_{Al} = 0.90$, and it is clear that all the elements are detected in the spectrum in contrast to the salt coated case. Figure 4.8 (b) shows the measured relative ratio of Ni to Al, and clearly show that the SPMS does a reasonable good job of measuring the elemental ratios. This is also consistent with our previous work, where we created a core-shell structure of carbon coated aluminum.[37] In this case we have core-shell structure where both the core and the shell are highly absorbing. A typical mass spectrum obtained from experiment is plotted in Figure 4.9, and it also shows that both the material on the core (aluminum) and shell (carbon and hydrogen) were observed. We were able to show in this prior work that we could, when compared with TEM, measure the thickness of the carbon coating.

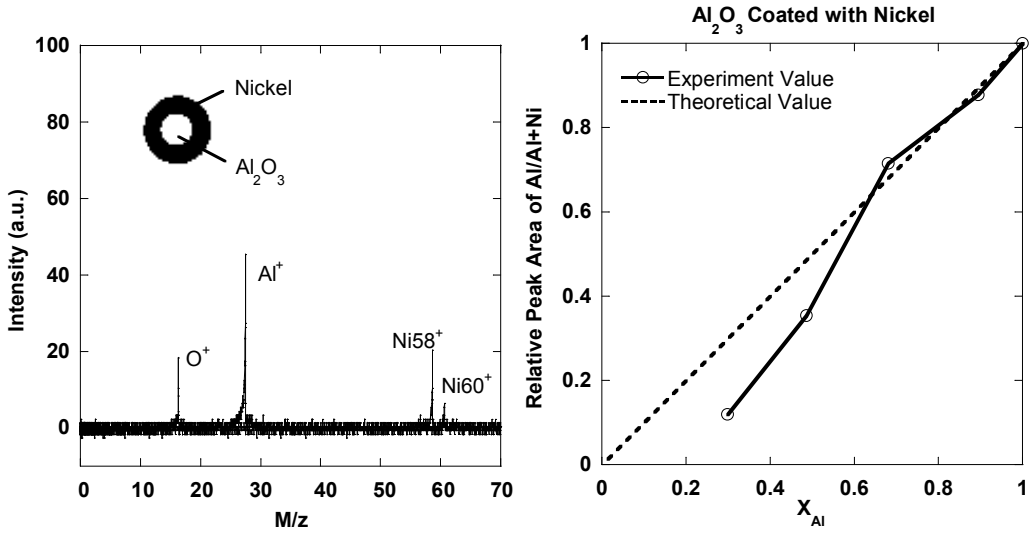

Figure 4.8 (a) Typical mass spectrum for aluminum oxide coated with nickel with aluminum elemental mol fraction of $X_{Al} = 0.90$ (b) Relative aluminum elemental mol fraction measurements for aluminum oxide particles coated with nickel.

We now turn our attention to multi-component matrix particles. The experimental observation suggests that the spectra obtained are also dependent on the relative concentration of each component. At high NaCl concentration, Cl can be detected. Also, although we can have a reasonable result for Al/Na ratio, the electro-negative specie Cl is still under-predicted in the spectra. This suggests that even for homogeneously mixed multi-component particles, there are composition biases for the laser ablation process. The possible reasons that may be responsible for these observations include charge transfer effects, and ion-electron recombination. Reilly et al.'s work showed that charge transfer in the laser ablation process has a significant influence on the resulting ion distributions, and lowering the detectability limits for electro-negative cationic species relative to electro-positive species.[96] Since Cl has a high ionization potential (IP), and high electron affinity, the positively charged Cl

ions are more likely to be neutralized by electron transfer from an electro-positive species, or from free electrons. For a particle with low NaCl concentration, it may be possible that most of the Cl ions generated by the plasma are neutralized so that we do not detect any Cl signal in the spectra. However, for a particle with high NaCl concentration, the abundant Cl ions present in the plasma may cause saturation in the charge transfer, and ion-electron recombination process to form Cl cations. To give a quantitatively explanation for the experimental observation, a complete understanding for the plasma formation/ion generation coupled with the charged transfer/ion-electron recombination process is required.

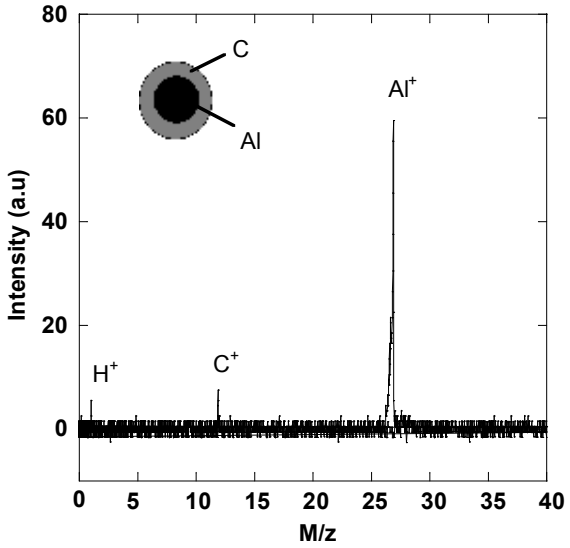

Figure 4.9 Typical mass spectrum for aluminum particle coated with carbon

The above experimental results and analysis suggests that:

a) *The total ionization approach should work well for a homogeneous dispersed mixture of materials comprising a particle regardless of their relative absorptivity. (e.g. Al_2O_3/NaCl matrix particle)*
b) *The total ionization approach should work well for a core-shell structure if both components are strong absorbers or if the stronger absorber is the shell. (e.g. carbon coated aluminum particle)*
c) *The total ionization approach does <u>not</u> work well for a core-shell structure in which a weak absorber surrounds a strong absorber. (e.g. NaCl coated aluminum or aluminum oxide particle)*
d) *The total ionization approach does <u>not</u> work well for quantitatively characterizing the electric-negative species in a multi-material particle regardless of the morphology. (e.g. Cl in Al_2O_3/NaCl matrix paritlce)*

There is one additional point to consider in class c) particles. Experimental results presented in Figures 4.4 (b) and 4.5 (b) show that the core material was under-represented relative to the shell in terms of Na, even though it was the stronger absorber, and over -represented relative to the shell in terms of Cl. The only plausible explanation for this observation is charge transfer. It is quite reasonable to assume that for the case of aluminum coated with salt that as the salt is being blow-off, and since it was not ionized directly from the laser, that charge transfer between elements in the core and shell material should take place. In this case Na which is easily ionized, and has a lower IP than Al, will donate an electron to Al, thereby neutralizing

it, and decreasing the relative Al signal. On the other hand chlorine has the highest IP, and a high electron affinity will, for the low temperature plasma shell, find itself certainly not forming cations, but possibly anions. Analysis of negative ions in the mass-spectrometer showed only an electron signal implying that the negative ion signal is too small to be detected.

The above discussion gives a qualitative explanation for the experimental observations. However, to achieve the goal of quantitatively characterizing nanoparticles by using SPMS, a more detailed explanation is needed to understand the mechanism of laser-particle interactions.

4.4 Conclusions

In this chapter we have reported our observations of morphology/component biases in characterization of multi-component particles using single particle mass spectrometry. We studied core-shell and homogeneously mixed multi-component particles to understand the morphology biases in particle characterization using the complete ionization technique. We observed that for a core-shell structure, with a strongly absorbing material in the shell, the complete ionization technique gives a good elemental ratio for the electropositive elements. On the other hand for a weakly absorbing shell, errors in the elemental composition measurement correlate with the ionization potential of the elements. Homogeneously mixed matrix particles generally should give quantitative ratios for electropositive elements. However, we always observe that electronegative species are under-predicted for a multi-component particle. A qualitative explanation for the observed behavior was developed in this work, and we believe that this behavior is strongly associated with the particle

thermal/optical properties, and the complicated nature of the laser-particle interaction process. The experiment results suggest that to overcome these limitations a detailed explanation of laser ablation/ionization process is need.

Chapter 5

Temperature Jump/Time-of-Flight Mass Spectrometry for Time Resolved Analysis of Energetic Materials

5.1 Introduction

In the preceding chapters we discussed the development and improvement of ion-mobility spectrometry and Single Particle Mass Spectrometry, and their applications toward characterization of the intrinsic reactivity of nanoparticles. This chapter and the next chapter, we turn our attention to the reactivity of nanocomposite materials, and present a mass spectrometric approach for probing the reactions between nanoparticles. In this work, a new Time-of-Flight mass spectrometer (TOFMS) with electron ionization (EI) source was developed, with the aim of obtaining time resolved mass-spectra during the ignition of energetic materials. The unique feature of this apparatus is a) implementation of TOFMS/EI with a Temperature Jump (T-Jump) technique to monitor highly reactive condensed state-samples at high heating and decomposition rates, and 2) measurement of the chemistry in a bi-molecular gas-phase-free kinetic environment. Due to its low detection limits and fast time response, the instrument developed here allows for a time resolved characterization of the decomposition, ignition, and combustion of solid energetic materials. This chapter is devoted to describe the operation of the T-Jump/TOF mass spectrometer and its example applications, while the next chapter present a study of nanocomposite thermite reactions using this instrument.

Quantitative measurements of the condensed phase reaction kinetics are usually performed using conventional thermal analysis techniques[107] such as TGA

(Thermogravimetric Analysis) and DSC (Differential Scanning Calorimetry). However, those methods fail in the measurement of fast chemistry processes such as rapid thermal decomposition, ignition and combustion of energetic materials where high heating rates are involved. It is well established that the high heating rates in those processes are critical and must be attained in order to study rapid condensed phase reactions.[108-110] In recent years, many experimental diagnostic methods have been developed to characterize rapid reaction processes.[5, 20, 107, 111-116] In particular, T-Jump (Temperature Jump)/FTIR (Fourier Transform Infrared Spectroscopy) was developed for studying reaction kinetics of condensed-phase propellants.[110, 117] In the T-Jump/FTIR the sample is placed on a Pt filament and rapidly heated to a chosen temperature and the gaseous species are detected and quantified using FTIR spectroscopy. The thermal decomposition behaviors of numerous energetic materials under isothermal conditions have been studied using this technique.[118-120] However, for rapid condensed phase reactions especially those associated with an ignition event, the relevant time scale can be on the order of milliseconds or less. The nominally low IR spectra scanning rate greatly limits the application of the T-Jump/FTIR spectroscopy in characterizing ignition, and combustion.

Mass Spectrometry (MS) is widely used to study condensed phase reactions.[5, 121] For decades, the use of MS alone or in conjunction with other techniques has become a powerful tool for thermal analysis.[4, 115, 122-126] Blais and co-workers developed a TOFMS/EI apparatus capable of measuring the intermediates and products of chemical reactions from detonation of explosives.[115,

127] The decomposition of thermite based aluminum/iron (III) oxide energetic material was also studied using the Matrix-Assisted Laser Desorption/Ionization (MALDI)-TOFMS technique, and the products of laser initiated thermite reactions were identified.[128, 129] Time resolved measurements for condensed phase reactions have also been conducted using MS techniques. Dauerman and co-workers developed a scanning sector mass spectrometer which directly attaches to a low pressure strand burner to study the thermal decomposition and combustion of nitrocellulose.[116, 126] The sample is heated by exposure to the radiation of an arc image furnace and the gaseous species as well as the surface temperature are continuously analyzed by a mass spectrometer and thermocouple as a function of time. Behrens developed a thermogravimetric modulated beam mass spectrometer that combine thermogravimetric analysis, differential thermal analysis, and modulated beam mass spectroscopy. This instrument is capable of quantitative measurement, and has been used to study thermal decomposition mechanisms and kinetics of many compounds.[130-132] Korobeinichev and co-workers developed a pulse heated mass spectrometer to study the high temperature decomposition of ammonium perchlorate.[133]

Common to all these methods has been that the studies were conducted at either slow heating rate, e.g. the thermal decomposition took place in minutes, or the mass spectrometer sampling rates were slow, e.g. ~ 0.1 sec. Recently, confined thermolysis FTIR spectroscopy with a TOFMS system has allowed for the gaseous products from a high pressure thermolysis chamber.[134] Although the time

resolution of the mass spectra measurement can be ~ 1 ms, the system time respond is limited by the slow sampling rate of the FTIR probe.

Despite the many efforts directed to characterizing condensed phase reactions, time resolved characterization of very rapid condensed phase reactions, particularly those associated with ignition and combustion have proved to be a formidable task. These processes, where the heating rates are usually of the order of 10^3~10^6 K/s, are beyond the limit of current thermal analysis techniques.[23, 111]

One additional consideration is that for many of the MS and FTIR studies, experiments were conducted in an open tube condition, such that much of the chemistry occurred in the gas-phase. However to gain a mechanistic understanding one would like to separate the condensed vs. gas phase contribution. Thus, in order to understand the decomposition mechanism or the combustion process of energetic materials, it is necessary to separate the primary and secondary processes, and investigate the condensed phase reaction under the condition of rapid heating.

Our objective in developing the T-Jump-MS system was first be able to characterize chemistry under high heating rate conditions (i.e. fast chemistry), and second to conduct the experiments under conditions where the secondary gas phase chemistry can be minimized. In the former case high heating rates correspond more closely to the environment usually encountered by energetic materials but more profoundly one should expect reaction channels to increasing favor the higher activation channels possessing the lowest entropy constraints. The later emphasis of minimizing gas-phase chemistry eliminates the possibility of bi-molecular gas phase reaction and likely much unimolecular decomposition. As a result the rapid pyrolysis

of energetic materials in vacuum should be dominated by condensed phase reactions, which should ultimately allow for a more direct probe of condensed phase chemistry. The essence of the experiment is that the T-Jump probe is directly inserted into the Electron Ionization chamber of the mass spectrometer, and the species from T-Jump excitation are monitored by the TOF mass spectrometer continuously. The time-resolved mass spectrometric capabilities of the instrument enable the characterization of rapid solid state reactions, which should provide an insightful complement to conventional thermal analysis. The purpose of this chapter is to describe the operation and capabilities of this new instrument. The development of T-Jump/TOF mass spectrometry was done along with Nicholas Piekiel and Snehaunshu Chowdbury, this work has been published by our group.[66]

5.2 Experimental Section

5.2.1 EI/TOF Mass Spectrometer

The EI/TOF mass spectrometer is comprised of a linear Time-of-Flight chamber, adapted from a previously developed Single Particle Mass Spectrometer (SPMS)[5, 82] as described in chapter 3 and chapter 4, and includes an electron gun for ionization, and the T-Jump probe with an electrical feedthrough, as shown in Figure 5.1. The sample loading chamber is separated from the ionization chamber by a gate valve, which enables the T-Jump probe to be rapidly changed without the need to break vacuum in the TOF chamber. An electron gun (R. M. Jordan Company, Grass Valley, CA, US) is mounted between the extraction plates of the TOF, and perpendicular to the orientation of the T-jump probe. The electron beam is nominally

operated at 70 eV, and 1 mA, with the background pressure in the TOF chamber at ~10^{-7} Torr.

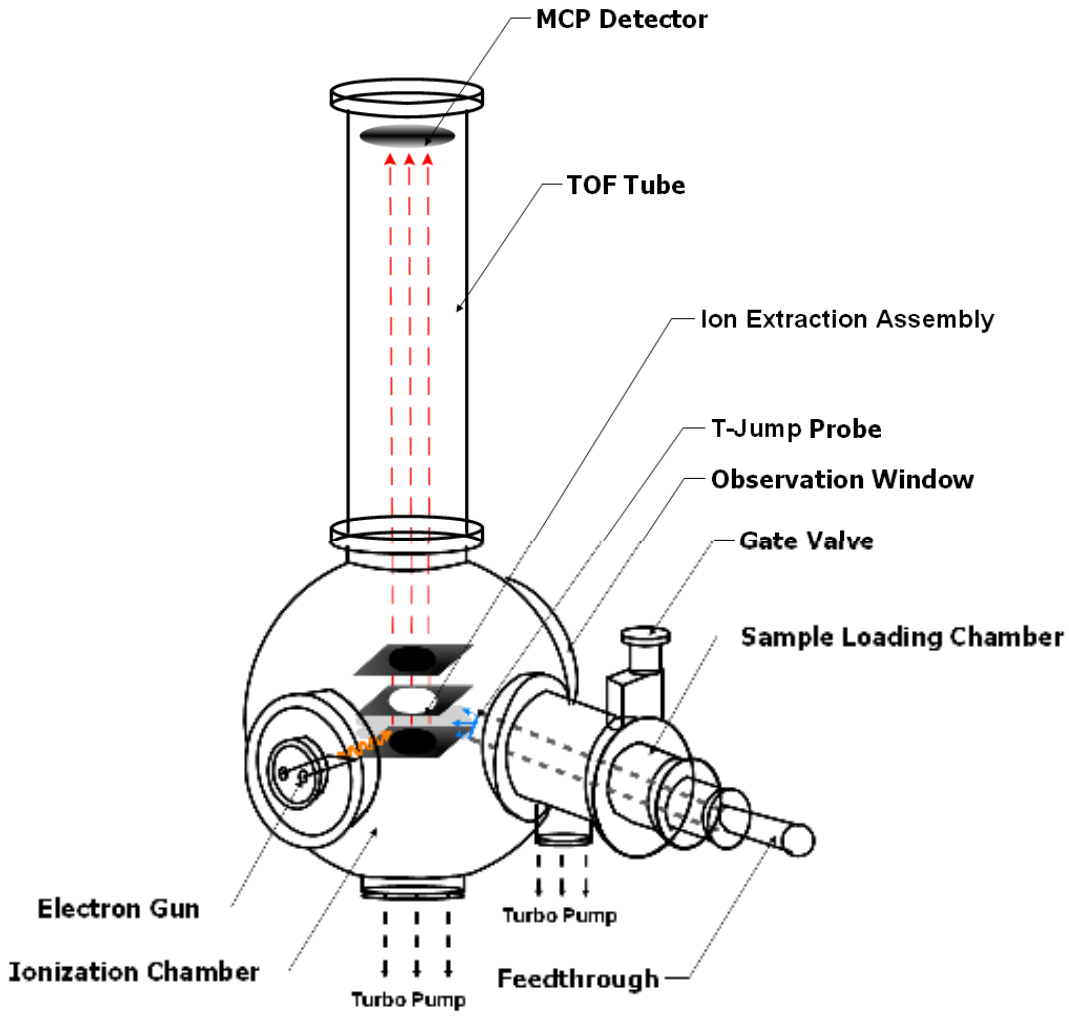

Figure 5.1 Schematic of T-Jump/TOF mass spectrometer.

5.2.2 Temperature Jump Probe

For the T-Jump we have primarily used a 76 m diameter platinum wire, with a total heated length of ~ 1 cm, which is replaced after each heating event. In each experiment, the wire is coated with a thin layer of either sample powder as in the case of particulates, or solution dipped to prepare organic coatings. Using an in-house built power source, the heating rate of the T-Jump probe can be varied by changing the pulse voltage or pulse width, at a rate of up to ~ 5 x10^5 K/s for the present filament configuration.

5.2.3 Control and Data Acquisition System

The schematic of the control and data acquisition system for the T-Jump/TOF mass spectrometer is shown in Figure 5.2. The present design is based on a previously developed Single Particle Mass Spectrometer (SPMS) which is configured for a standard laser ionization source.[5, 135] To ensure a field-free region for EI ionization, one DC high voltage power supply is used with a "T" splitter to bias both the repeller plate, and the extraction plate (V1 and V2 shown in Figure 5.2). In the presence of a field-free region, electrons are injected between the plates and ionization takes place. After a predetermined ionization period the voltage on the extraction plate is changed by a high voltage pulser, to create the field for ion extraction region between the plates. The extracted ions drift in the linear TOF tube, and are counted at the MCP (Microchannel Plate) detector. Following the ion extraction period, the voltage on the extraction plate is pulsed back, and a new ionization period begins. Serial pulses generated from a pulse generator (DG535, Stanford Research System, Sunnyvale Inc, CA, USA) are used to trigger the high

voltage pulser so that the ionization and extraction processes occur continuously. The pulse timing sequence of the high voltage pulse is also traced from the monitor signal output of the high voltage pulser. Both the detector signal and the monitor signal are recorded with a 500 MHZ digital oscilloscope and transferred to a PC for further analysis.

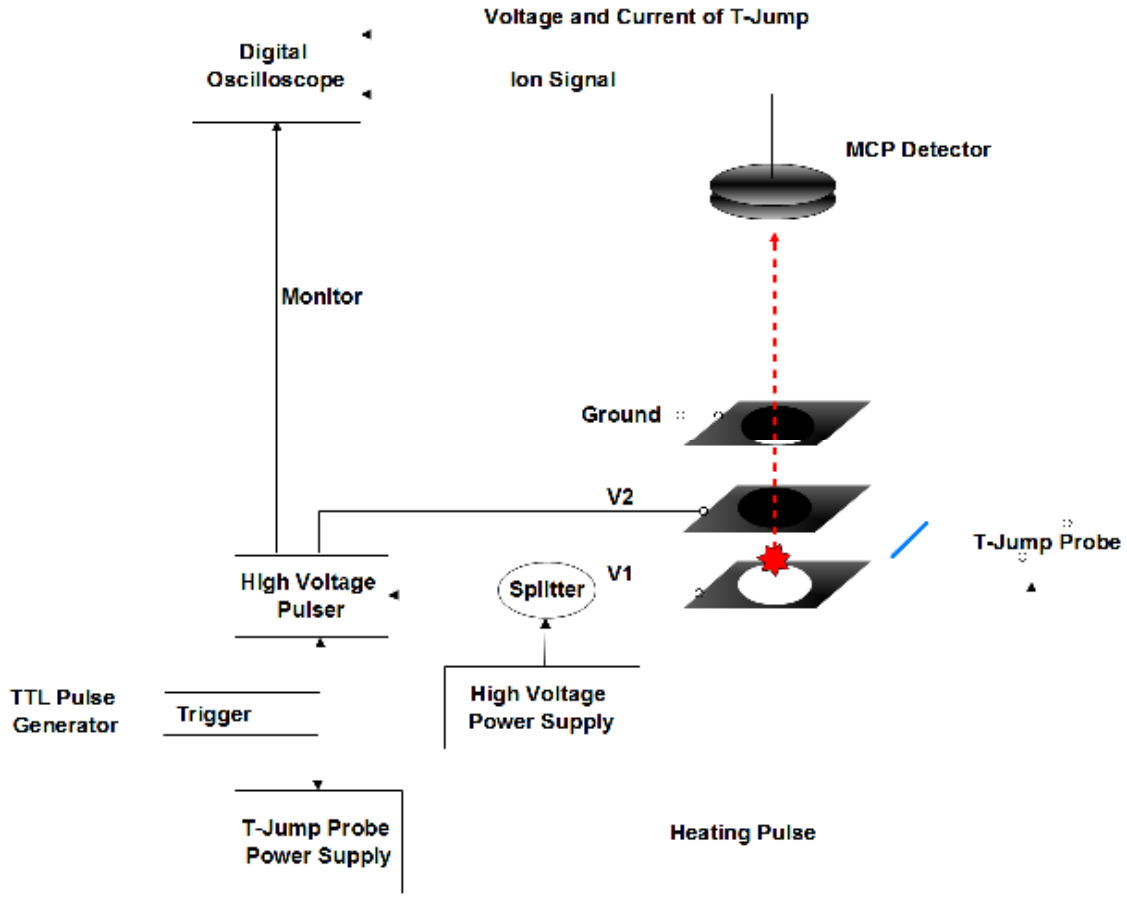

Figure 5.2 Schematic of the control and data acquisition system for the T-Jump/TOF mass spectrometer.

The heating of the T-Jump probe is also synchronized with the Time-of-Flight measurement system by triggering the probe power supply from the pulse generator as shown in the timing sequence diagram (There is ~2 s delay between trigger and monitor signal, for illustration purpose we show them as the same pulse in Figure 5.3). The temporal voltage and current of the T-Jump probe during the heating event is recorded, so that a resistivity measurement can be obtained, and related to the instantaneous temperature, which can be mapped against the mass spectra.

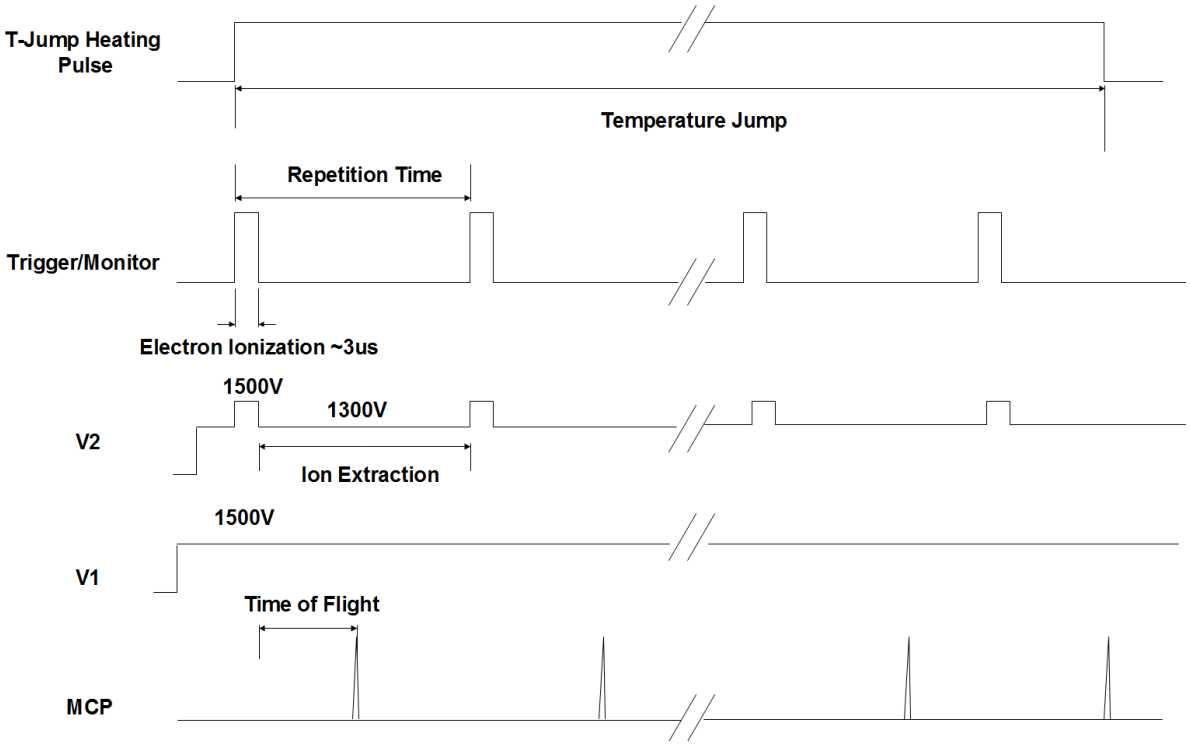

Figure 5.3 Pulse sequence used for EI ionization and ion extraction in the T-jump/TOF mass spectrometer.

5.3 Results and Discussion

Before testing the T-Jump/TOF mass spectrometer, T-Jump probe heating experiments were conducted by heating an un-coated wire to evaluate the performance of T-Jump probe. The heating rate of the probe can be varied by changing the heating pulse width and the output pulse intensity. The pulse width can be varied from ~ 1 ms to ~100 ms, with a maximum output voltage of ~50 V. Figure 5.4 (a) shows a typical current, voltage trace, while Figure 5.4 (b) shows the resulting temporal temperature of the platinum wire. Since the rise time of the heating pulse is in the range of 10 to ~100 us depending on the output pulse voltage, the resistance and the corresponding temperature is calculated after the rise time of the heating pulse. Thus the filament temperature is estimated to be ~400 K initially, and reaches ~1800 K after the 2.5 ms; i.e. a heating rate ~640,000 K/s.

Another important factor to consider in the design of the T-Jump/TOF mass spectrometer is the nature of the ion extraction in the presence of the T-jump probe. The nominal configuration of the ion extraction electrode assembly ensures a uniform extraction field between the plates.[135] However the presence of the probe and in particular its location was found experimentally to be a sensitive parameter to both signal sensitivity and resolution. One might reasonably expect that placing the probe too close to the extraction plates would distort the electric field, and result in a decrease in the mass spectrometer's resolution. Placing the probe too far away from the ionization region would lower the concentration of reaction product species in the ionization region, and consequently decrease the sensitivity of the measurement.

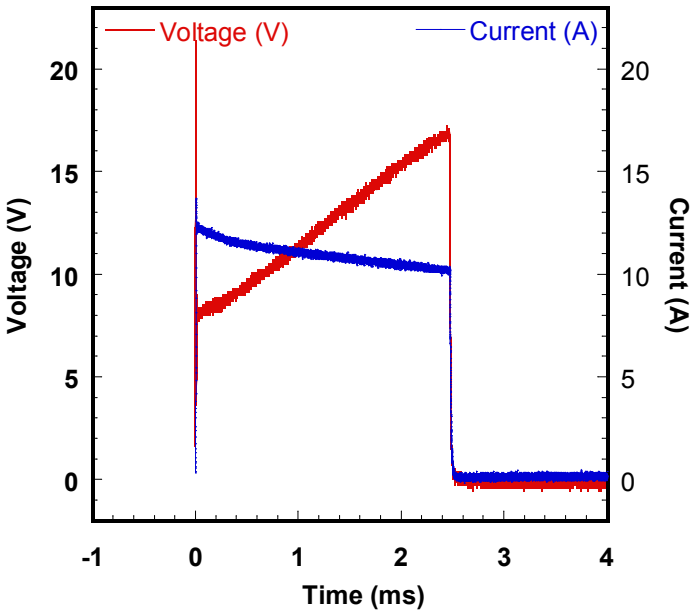

(a)

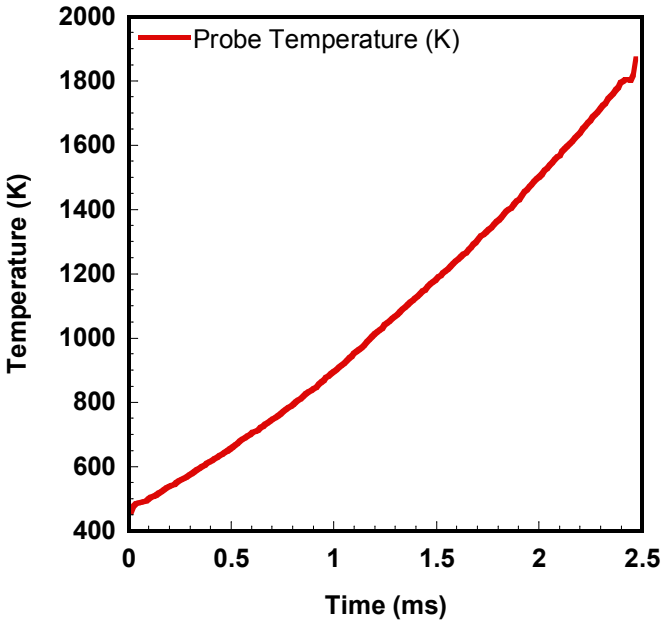

(b)

Figure 5.4 (a) Voltage and current across the T-jump probe. (b). Estimated probe temperature from electrical resistance

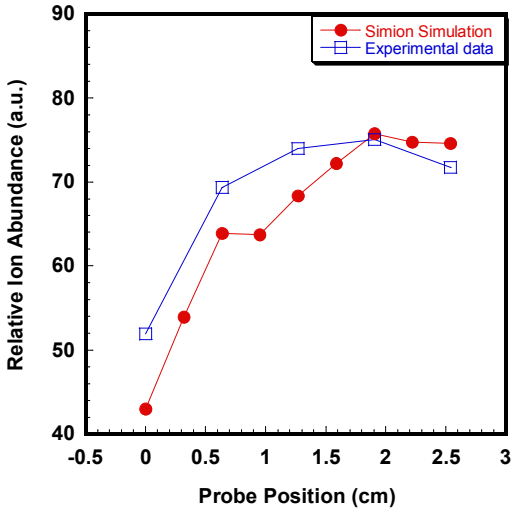

(a)

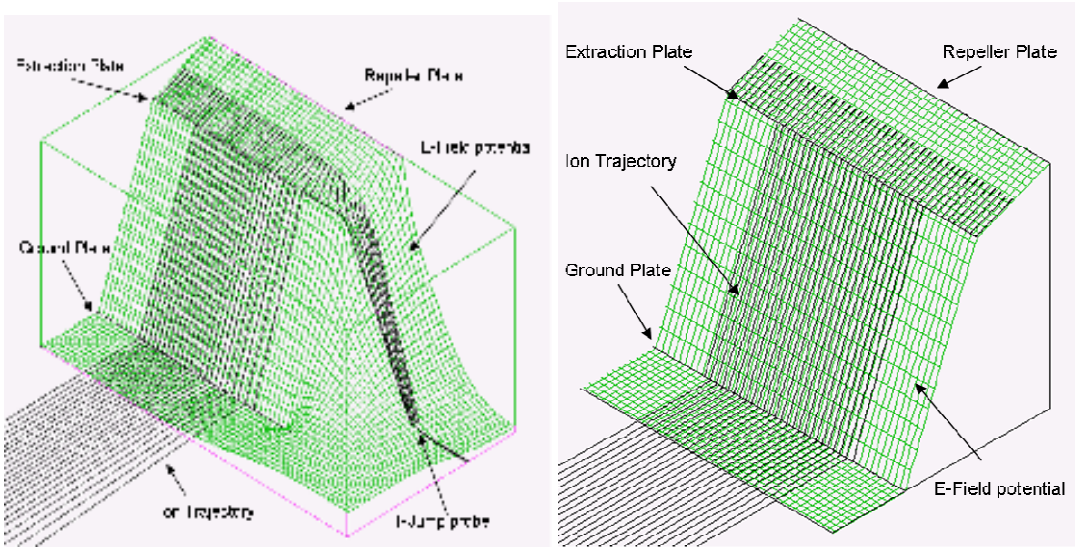

(b) (c)

Figure 5.5 (a) Relative water ion abundance as a function of the probe filament position. (b). Ion trajectory and electric potential at ion source region with the presence of T-Jump probe. (c) Ion trajectory and electric potential calculation at ion source region without probe.

The effect of the T-Jump probe position was examined experimentally by inserting the probe at different distances from the plates, and monitoring the ion signal from the background gas. The relative water (H_2O) ion intensity are plotted in Figure 5.5 (a) as a function of probe position. Each experimental data point is an average of 40 mass spectrum measurements, and normalized by the ion intensity measured without the presence of the T-Jump probe. As a comparison to the experimental data, the effect of the T-Jump probe on the electric field and ion detection was also evaluated by conducting ion-trajectory simulations using Simion.[88] In the simulation, water ions with +1 charge were placed in the center plane of the ion extraction region with a uniform distribution, and their flight trajectories were calculated for the voltages used in the experiment. The relative ion abundance calculated from trajectory simulation is also plotted as the function of probe position in Figure 5.5 (a). Both simulation and experimental data show that the ion signal is significantly decreased when the probe is placed close to the extraction plates. As the probe moves away from the plates, the ion signal increases, and reaches a plateau at a distance of 1.3 cm, suggesting that the presence of the grounded probe significantly perturbs the electric potential in the ion source region. Figure 5.5 (b) shows the calculated electric potential and ion trajectories for T-Jump probe placed 1.3 cm from the ionization region. When compared with the no-probe case in Figure 5.5 (c), it is clear that the probe induces considerable distortion to the electric potential, and ion trajectories in the region closest to the T-Jump probe, but very little change for ion trajectories in the central region. As we further move the probe away from the ionization region, even though the effect of the probe on the electric field is

minimized, a slight decrease of the ion signal in the experimental data was observed. This implies that at larger distances sensitivity will be lost for material originating from the probe, and that a distance 1.3 cm would seem to be a near optimal for this system.

Nitrocellulose and hexahydro-1,3,5-trinitro-1,3,5-triazine (RDX) samples were used to test the performance of the T-Jump/TOF mass spectrometer as examples of a slow and fast "burners". In these experiments, nitrocellulose sample (Mallinckrodt Baker Inc. Phillipsburg, NJ, USA) or RDX was mixed with diethyl ether or acetone, and a small amount of solution (~7 μl) is coated on the T-Jump filament surface using a dropper. While the eventual goal of this instrument is to use the temporal mass spectra, and temperature, to extract mechanistic information, the purpose of current discussion is focus on illustrating the capabilities of the instrument.

The mass spectra obtained for rapid pyrolysis of nitrocellulose are shown in Figure 5.6. The heating duration is about 9 ms with a heating rate of ~1.3 $\times 10^5$ K/s, with a total of 95 spectra sampled with a temporal resolution of 100 s per spectrum (10000Hz). Out of the 95 spectra obtained in the experiment, we plot 17 of them in Figure 5.6, along with a more, detailed view of a spectrum at t = 2.5 ms. Since the heating pulse is synchronized with the first EI duration, the mass spectrum at t = 0 ms is actually the background in the ion source region, which consists of water (m/z 18), N_2 (m/z 28), N (m/z 14), OH (m/z 17), O_2 (m/z 32), and H (m/z 1). We sampled up to m/z ~ 300 for each spectrum, but no heavy ions were observed, and major ions are only seen for m/z <100. At t =1.7 ms, the estimated temperature of the probe is ~575

K, and a new ion of m/z 31 appears which suggest the start of the reaction. At t = 1.8 ms which corresponds to a probe temperature ~590K, the ion signal intensity of m/z 31 increases along with ions at m/z of 15, 27, 29, 45 and 59. As the reaction time advances to t = 1.9 ms (T~ 600K), ion m/z 31 achieves its maximum intensity, and now ions at m/z 30 and 46 appear, along with m/z 16, 43, and 44. These species last for the whole duration of the heating pulse (~9ms), and some species are still present well after the end of the wire heating due to the self-burning of nitrocellulose. The time-resolved feature of the spectra allows us to extract the characteristic time of the reaction. As the highest ion intensity for most of major ions were achieved at t = 2.3 ms, following which the ion signals gradually decreases with no noticeable changes after 4 ms, it is suggested that the most aggressive reaction (ignition) happens within ~4 ms, and the whole reaction lasts ~9 ms. We compare our results for nitrocellulose thermal decomposition with experiments done at lower heating rates. Chen et al used a SMATCH (Simultaneous MAss and Temperature Change)/FTIR system to examine decomposition products of a nitrocellulose film heated at a rate of up to 320^{o} C/s. The reaction products are noted as, NO, CO, CH_2O, CO_2, HCOOH, and NO_2,[136] which we also see, although we are unable to distinguish HCOOH from NO_2. It should also be noted that although m/z 28 is part of our background signal of N_2, there is significant increase for this peak during the heating event, which most like can be attributed to CO. We also compare work with that of Dauerman and co-workers who used a mass spectrometer paired with a low-pressure strand burner to examine nitrocellulose combustion.[126] This work shows multiple spectra at different times during heating, which include significant ions that are consistent with our work. The

major ions cited are m/z of 14, 15, 16, 17, 18, 27, 28, 29, 30, 31, 43, 44, 45, 46, which are all seen in our experiment excepting m/z 14, 17, 18.

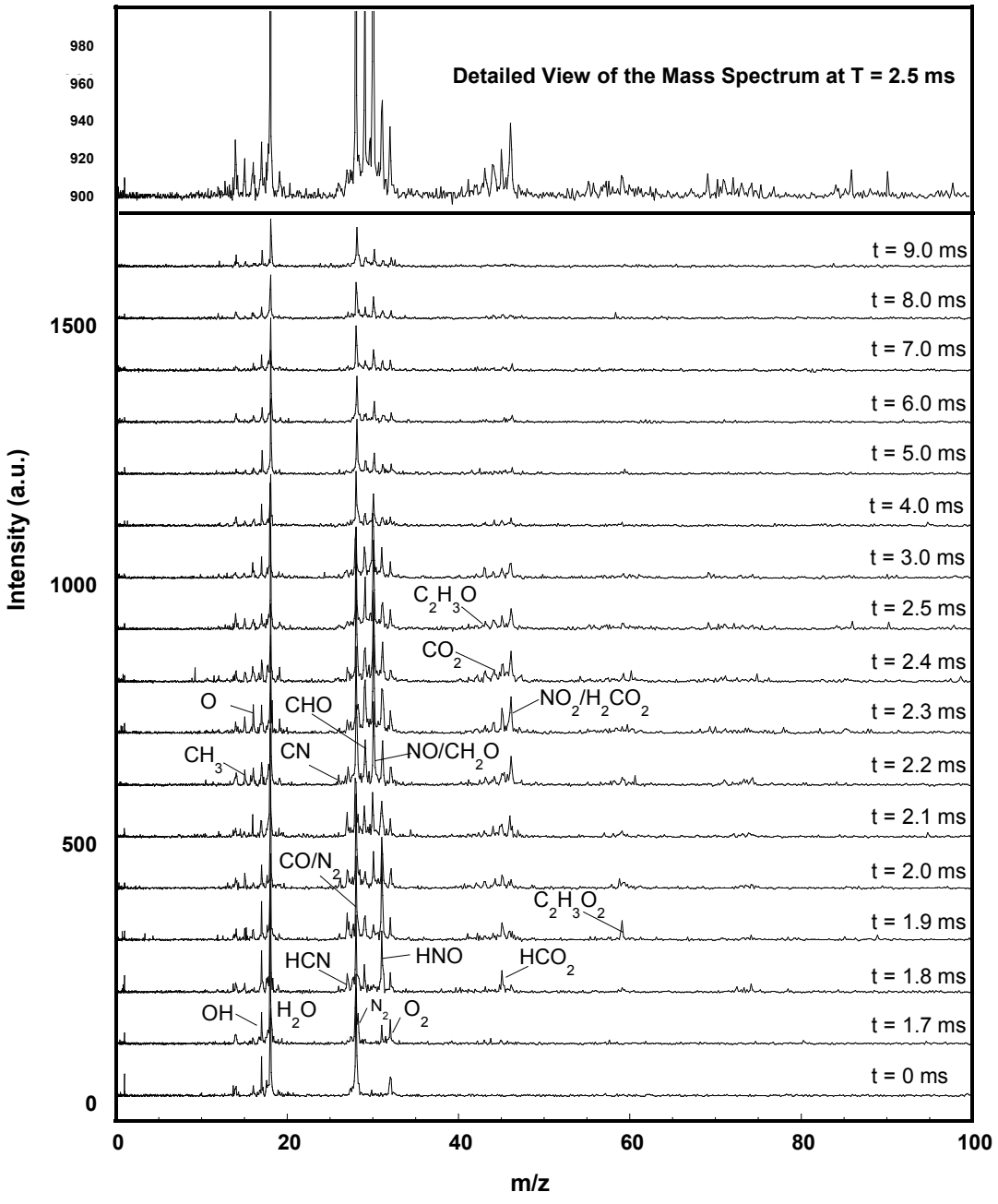

Figure 5.6 Time resolved mass spectrum from rapid heating of nitrocellulose. Heating rate ~ 1.3 $\times 10^5$ K/s

RDX was used as a second example to test the T-Jump/TOF mass spectrometer. RDX decomposition has been the subject of investigation under different conditions. Behrens and co-workers have studied RDX decomposition using the simultaneous thermogravimetric modulated beam mass spectrometry (STMBMS).[130, 137, 138] The results via STMBMS provide detail information about both mechanisms and rates of reaction of RDX decomposition under low heating rate (~1K/min). The combustion like decomposition of RDX has been studied using a T-jump/FTIR method with a heating rate at ~10^3K/s.[108-110, 117, 118, 139] In our experiments, a heating rate of ~10^5 K/s was used to study the ignition and combustion of RDX. Similar to the nitrocellulose experiment, we use a sampling rate of 100 s per spectrum (10,000Hz) to capture the progression of the reaction. The heating pulse is about 8 ms at a heating rate of ~1.5×10^5 K/s, and a total of 95 spectra obtained. Figure 5.7 shows that species, other than background species (water/N_2/O_2), only appear from 0.7 ms - 2.6 ms, which corresponds to a wire temperature of 370K to 670K. These results clearly show as expected that RDX is more facile than Nitrocellulose, and occurs over an interval of only ~2 ms. Although m/z range up to 400 was recorded for each spectrum, no heavy ions were observed above m/z 150. The major ions from RDX decomposition observed are m/z 15, 28, 29, 30, 42, 46, 56, 75 and 127. Small ions of m/z 14, 16, 41, 43, 81, 120 are also found in some spectra. The RDX mass spectra in terms of m/z values observed and their most likely ions structures are tabulated in Table 5.1. Similar to the T-jump/FTIR method,[108-110, 117, 118, 139] species of NO_2, CH_2O, NO, CO, HNCO are also observed by our T-jump/TOF mass spectrometer. Using gas phase CO_2 laser

photolysis of RDX, which provided extremely high heating rates, Zhao et al. observed ions at 42, 56, 75, 81, 120 and 127,[140] which we also see in our experiments. However, HONO, HCN and N_2O which are reported in both T-jump/FTIR and gas-phase infrared multiphoton dissociation experiments were not detected under our conditions. The differences point to the complex nature that heating rate and ambient environment may play in probing the decomposition pathways. For example, it is believed that two global reactions are responsible for the decomposition of RDX under flash heating condition.[139] The reaction channel which leads to the formation of N_2O is dominant at lower temperature region, while the reaction channel to NO_2 favors the higher temperature condition. Our heating rate is much higher than the heating rate employed in T-jump/FTIR experiments ($\sim 10^5$ K/s vs. $\sim 10^3$K/s) it is possible that the chemistry is dominated by the NO_2 channel and N_2O is not favored under these conditions. Moreover, as one of the motivations in developing this T-jump mass spectrometer, was to minimize or eliminate the gas phase chemistry, the failure to detect species such as HCN and HONO and possibly N2O suggests these may be formed primarily in the gas phase.

Table 5.1 Ions observed from mass spectra of RDX pyrolysis and their possible assignments.

m/z	Species
14	$N^{\#}$
15*	CH_3, NH
16	O
17	$OH^{\#}$
18*	$H_2O^{\#}$
28*	$N_2^{\#}$, CH_2N, CO
29*	HCO
30*	NO, CH_2O
32	$O_2^{\#}$
41	CHN_2
42*	C_2H_4N, CH_2N_2, CNO
43	HCNO
46*	NO_2
56*	$C_2H_4N_2$

(*) major ions
($^{\#}$) species also observed in background MS

Since the purpose of this chapter is to demonstrate of the operation and capabilities of the instrument, we defer further analysis on rates of reactions and mechanisms to the future work. Based on the experimental results presented above, it is clear that the characteristic reaction time for the decomposition/combustion of energetic materials is in the order of milliseconds or even less. We note that while a time resolution of 100μs was used to test and demonstrate the instrument, the T-Jump/TOF mass spectrometer can be operated with a scanning rate up to ~ 30 kHz. The experimental results suggest that the time-resolved spectra obtained using T-jump/TOF mass spectrometer should have sufficient sensitivity, and time resolution to probe the reaction dynamics of extremely fast condensed state reactions at high heating rates.

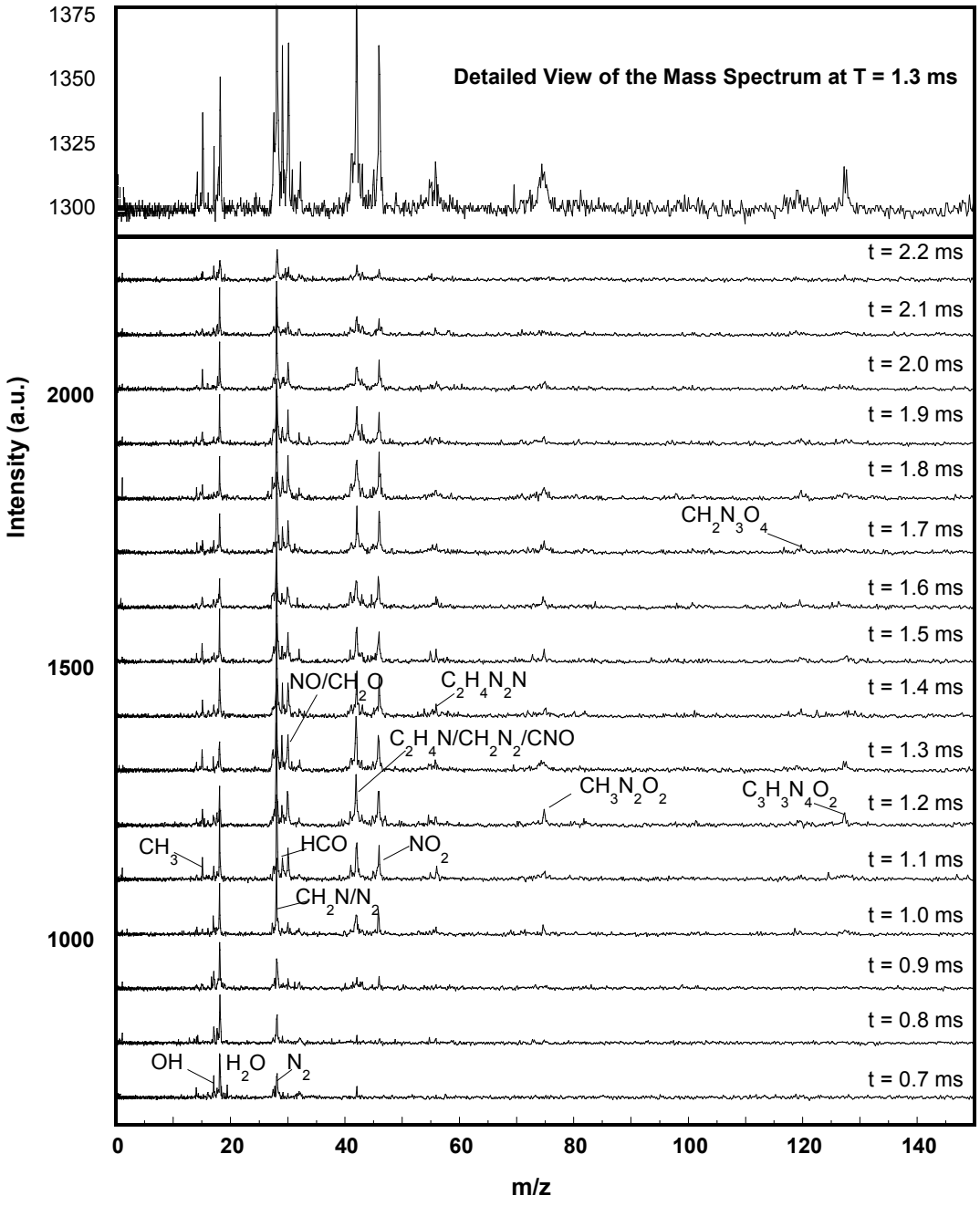

Figure 5.7 Time resolved mass spectrum from rapid heating of RDX. Heating rate ~1.5×10^5

5.4 Conclusion

A new Time-of-Flight mass spectrometer (TOFMS) combined with a temperature jump technique is described. The instrument allows for the time resolved characterization of the decomposition, ignition, and combustion of solid energetic materials or other highly reactive condensed state reactions. Using heating rates of up to 105 K/sec, samples of nitrocellulose and RDX were ignited, and time resolved mass spectra were obtained. By monitoring the electrical characteristics of the heated wire, the temperature could also be obtained and correlated to the mass-spectra. When combined with the time dependent temperature information, the results indicate that the instrument can capture the signature of rapid condensed phase reactions in a time resolved manner.

Chapter 6

Time-Resolved Mass Spectrometry of Nanocomposite Thermite reactions

6.1 Introduction

Thermites are a class of energetic materials which are comprised of a metallic fuel and oxidizer. In most thermite formulations, aluminum is used as a fuel because of its high energy density and low cost, and metal oxides such as CuO and Fe_2O_3 are commonly used as oxidizers. Compared with traditional organic energetic materials such as TNT and RDX, thermite reactions are characterized by high energy release but slow reaction rates due to mass transfer limits. In recent years, nanocomposite thermites, also known as Metastable Intermolecular Composites (MIC), have attracted great attention compared to their micron sized counterparts.[11, 12] In nanocomposite thermites, the reactive components are mixed at the nano-scale so that diffusion length can be greatly reduced and the surface area can be increased. As a result nanostructured particles have a much higher reactivity than their corresponding micron sized cousins. Aside from the fast reaction rate, the unique nanostructure of MICs also allows a control over the reactivity by varying parameters such as particle size, morphology and local composition.[13-15]

Studies of thermite energetic materials are very difficult due to their fast and intense reaction, and the relatively low gas production. Measurement of combustion properties such as flame speed, burn rate, or ignition temperatures are typical methods to characterize thermite reactions.[11, 12, 16-21] The reaction mechanism is often studied with traditional thermal analysis techniques such as thermogravimetric

analysis (TGA), differential thermal analysis (DTA) or digital scanning calorimetry (DSC). With the help of electron microscopy and X-ray diffraction, reaction products and detailed reaction kinetics at slow heating can be revealed.[22-24] Many experimental techniques have been developed to study thermite reactions under combustion-like conditions. Laser induced initiation technique, which can be easily used with other diagnostic techniques, has been used to study thermite combustion processes.[12, 141] The nanoscale aluminum and molybdenum trioxide composite (Al/MoO_3) was studied using CO_2 laser ignition with a high speed camera system, and the size dependent information about ignition behavior and burn rate was obtained.[12] Time-resolved spectroscopy was employed by Dlott and co-workers to investigate laser initiated Al/nitrocellulose mixture.[142] The optical emission spectra were also used to investigate the rate and mechanism in the energy release processes. Moore et al. used the time resolved spectral emission technique to study the combustion of the aluminum/molybdenum trioxide (Al/MoO_3) nanocomposite, where the species AlO was observed as the reaction product.[143] More recently, fast synchrotron x-ray microdiffraction technique was used to characterize the self-propagating exothermic reaction of Al/Ni multilayers, time-resolved measurement was achieved with temporal resolution of 55 μs and spatial resolution of 60 μm.[144] A hot filament heating technique is also widely used in studying reaction kinetics under high heating rates. In particular, temperature-jump (T-Jump)/FTIR has been developed to study reaction kinetics of condensed-phase propellants, and many organic energetic materials have been studied using this technique.[25, 109, 110] Recently, this approach was applied for kinetic analysis of metal powders.

Aluminum/molybdenum trioxide (Al/MoO_3) and aluminum/copper oxide (Al/CuO) nanocomposite mixtures were investigated using this technique and their kinetic reaction model was constructed from experimental data.[22, 23]

Recently, we employed a hot filament heating technique, and developed a T-jump/Time-of-Flight (TOF) mass spectrometer for time-resolved analysis of energetic materials.[66] In this chapter, aluminum/copper oxide (Al/CuO) and aluminum/iron oxide (Al/Fe_2O_3) nanocomposite thermite reactions are studied using T-jump/TOF mass spectrometry. A thin platinum wire coated with nanocomposite thermite was used as the T-jump probe, and was directly inserted into an Electron Ionization (EI) chamber of the mass spectrometer. Time-resolved mass spectra of thermite reactions were obtained at heating rates up to ~10^6 K/s. This work was done along with Nicholas Piekiel, and Snehaunshu Chowdbury, and is currently submitted for publication.

6.2 Experimental

6.2.1 Sample Preparation

Nanocomposite thermite samples were prepared by mixing aluminum nanoparticles with oxidizer particles to obtain a stoichiometric mixture. The aluminum used was 50nm ALEX powder obtained from Argonide Corporation. Copper oxide (CuO) and iron oxide (Fe_2O_3) nanopowders of ~ 100nm obtained from Sigma-Aldrich. TGA showed the ALEX powder is 82% aluminum (by mass) with an outer oxide shell and was accounted for in the preparation of stoichiometric samples (equivalence ratio of 1). Samples were mixed in hexane and the suspensions were

sonicated for about 30 minutes to break the agglomerate and ensure intrinsic mixing between the fuel and oxidizer. The prepared sample suspensions could then be coated on the T-Jump probe with a dropper. The T-Jump probe is a ~10mm long platinum wire with diameter of 76μm, for which the center of the wire is coated with a thin layer of sample with coating length of ~ 5mm. The coating thickness was estimated to be ~ 175 μm from SEM image shown in Figure 6.1, which would yield ~0.3 mg based on an ideal coating geometry model[111] and assuming a uniform particle size of 50 nm.

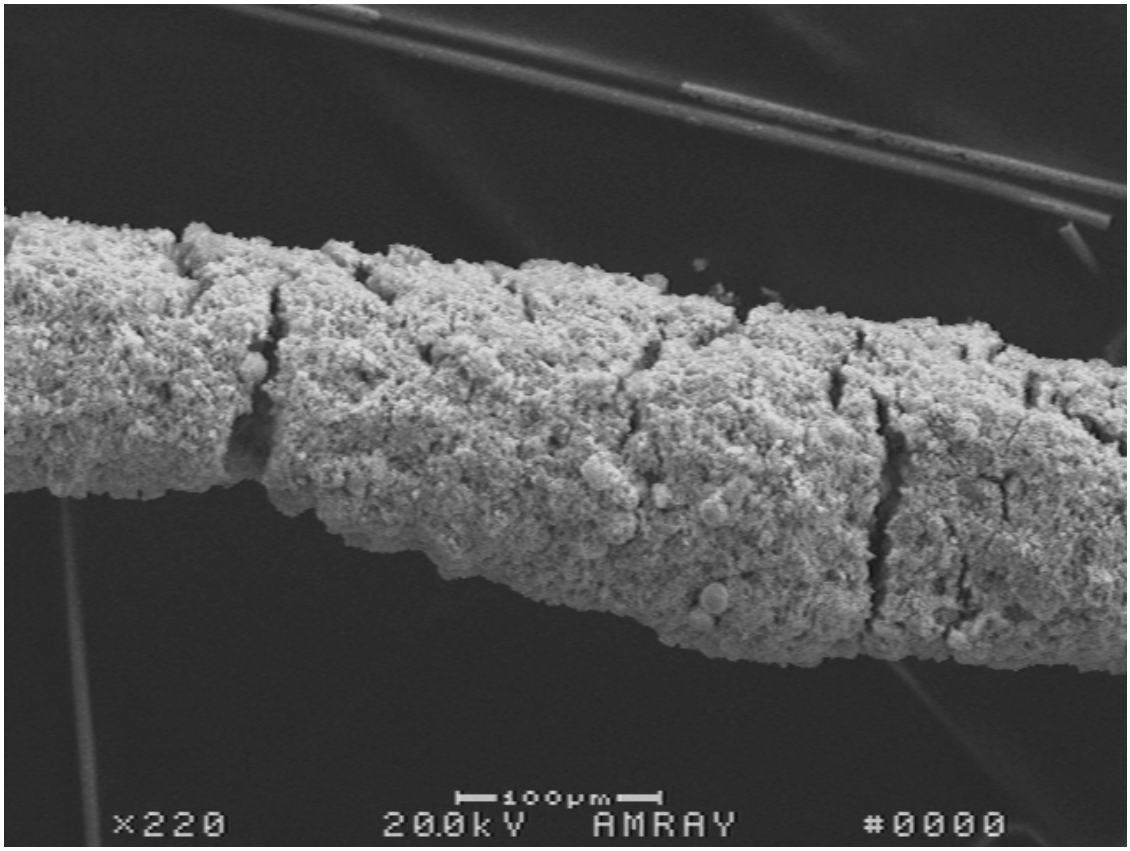

Figure 6.1 SEM image of T-Jump probe coated with Al/CuO nanocomposite mixture

6.2.2 T-jump/Time-of-Flight Mass Spectrometry

The T-Jump/TOF Mass Spectrometer has been discussed in chapter 5. This instrument is comprised of a linear Time-of-Flight chamber, an electron gun for ionization, and the T-Jump probe with an electrical feed-through for rapid sample heating. The schematic of the T-Jump/TOF Mass Spectrometer is shown in Figure 5.1 and re-plotted here in Figure 6.1. The essence of the instrument is that the T-Jump probe is directly inserted close to the Electron Ionization (EI) region of the mass spectrometer, and the species from T-Jump excitation are continuously monitored by the TOF mass spectrometer. The electron beam is normally operated at 70 eV, and 1 mA, with the background pressure in the TOF chamber at $\sim 10^{-10}$ atm. In each experiment, the T-Jump filament is coated with a thin layer of sample powder and can be heated with an in-house built power source at a rate of up to $\sim 8 \times 10^5$ K/s, with the filament replaced after each heating event. A detailed description of the operation of T-Jump/TOF mass spectrometer can be found in the preceding chapter. Briefly, the heating of the T-Jump probe is synchronized with the time-of-flight measurement system. A series of mass spectra as well as the temporal voltage and current of the T-Jump probe during the heating event is recorded by a 500 MHZ digital oscilloscope. From the current and voltage trace, a resistivity measurement can be obtained and related to the instantaneous temperature of the filament, which can be mapped against the mass spectra. Time resolved mass spectra combined with temperature information are then used for characterization of nanocomposite thermite reactions. In a parallel experiment, the T-Jump technique was coupled with a photomultiplier tube (PMT) setup for the measurement of the optical emission from the nanocomposite thermite

reaction. The experiments used the same T-jump wire except that the experiments were performed at atmospheric pressure. As an useful supplemental information, the PMT traces for nanocomposite thermite reactions were compared with the T-Jump/TOF Mass Spectrometry results.

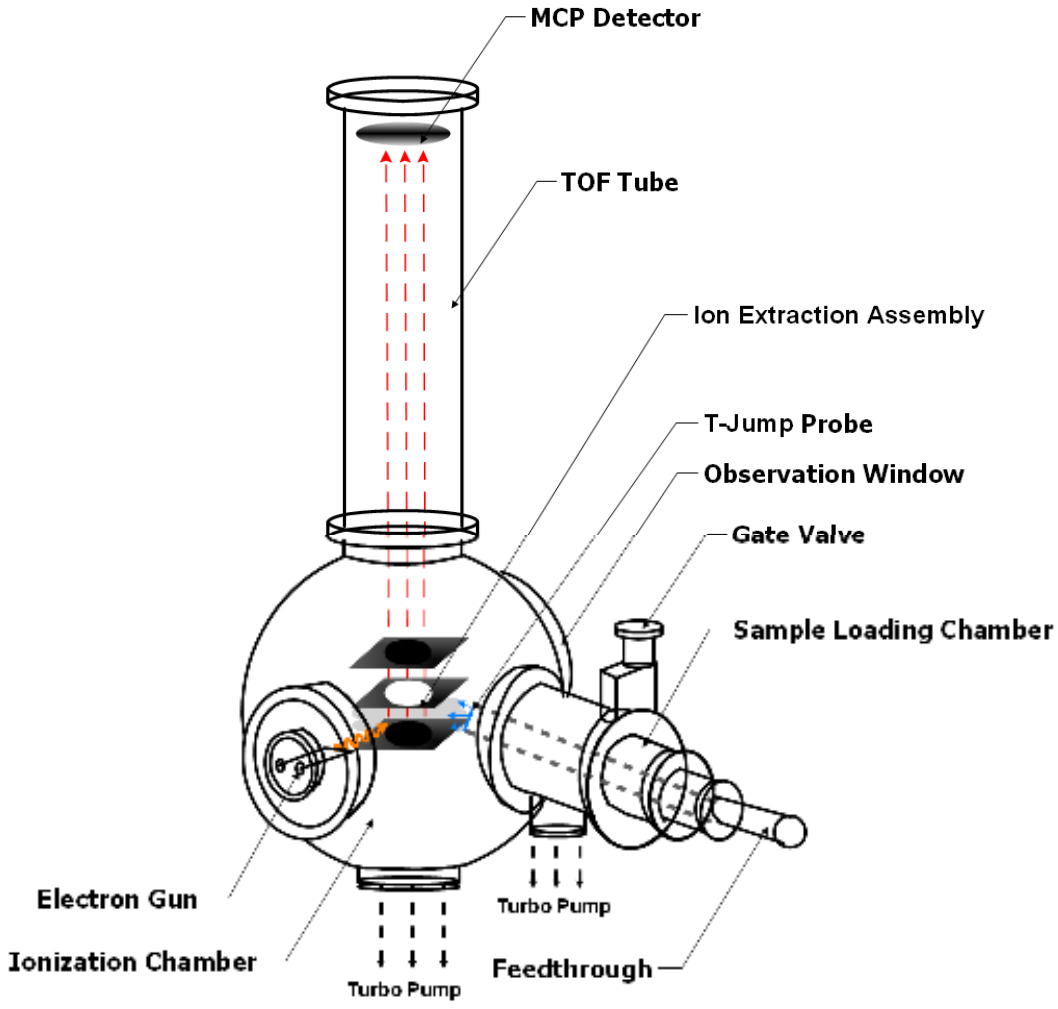

Figure 6.2 Schematic of T-Jump/TOF mass spectrometer.

6.3 Results and Discussion

6.3.1 Mass Spectrometric Measurements of Nanocomposite Thermite Reactions

In the previous chapter, time resolved mass spectra for rapid pyrolysis of organic energetic materials such as RDX and nitrocellulose were obtained using the T-Jump/TOF Mass spectrometer. In those experiments, the ion optics were biased to high potential to extract the ions from ionization region of the mass spectrometer. However, during the course of study the nanocomposite thermite reactions, we found that the initiation of the exothermic reaction can cause the malfunction of high voltage bias on the ion extraction optics and result lost of mass spectra signal. It is believed that there is an electrical conduction zone in the detonation front of solid explosives such as TNT and PETNA, and the corresponding electron density in the detonation front is several orders of magnitude higher than the theoretical value estimated from the Saha equation.[145] Douglas and co-workers reported a much longer conductivity profile for nanocomposite thermites and their work showed that the conduction mechanism is associated with the chemical reaction in nano-thermites.[146] Martirosyan and co-workers have observed a complex electric/magnetic field behavior and transient electric impulses generated from combustion of variety metal-gas reaction systems.[147-149] These works suggest us there are high degrees of ionization processes during the initiation of thermite reaction, and the current pulse can disturb the function of ion extraction optics in the mass spectrometer. We believe investigation on this ionization process reaction can

provide important insight on the initiation of thermite reaction and should be a subject of future research, however, it is beyond the scope of this work.

To characterize the nanocomposite thermite reaction using the T-Jump/mass spectrometry method, the standard ion optics configuration of the TOF mass spectrometer has to be modified to minimize the effect of electric impulse. In the new configuration, the ion source region is operated at ground to avoid collecting electrons/ions generated from the thermite event. The extraction plate is pulsed from ground to -200V by a high voltage pulser for ion extraction. A linear system is employed within the flight tube and biased to DC -1500V, together with the acceleration plate, to transport the ion beam to the MCP detector. This configuration successfully prevents loss of spectral signal caused by the thermite reaction.

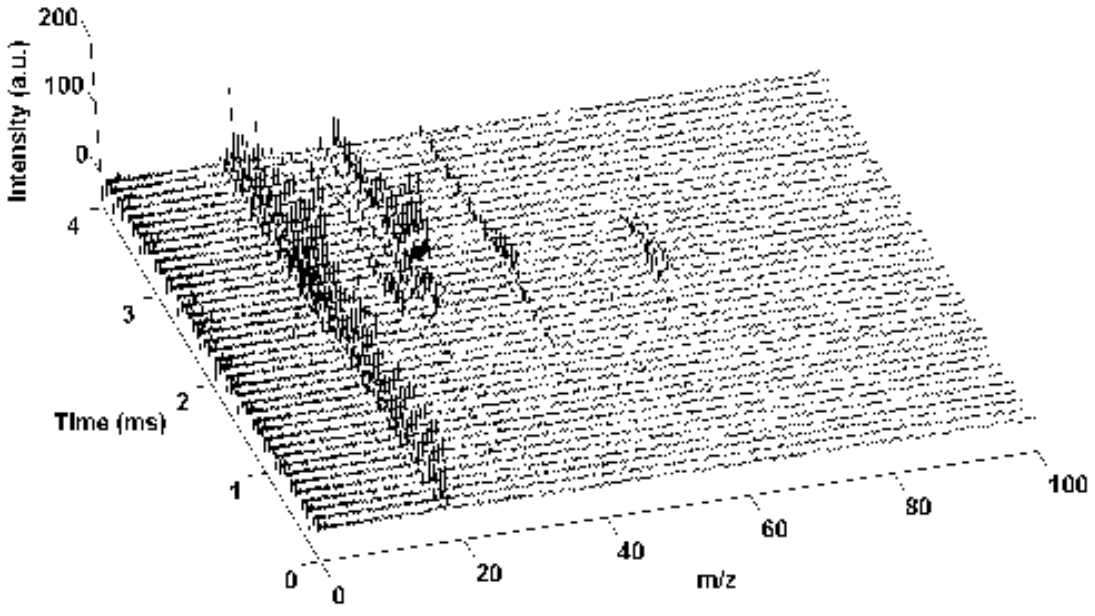

Figure 6.3 Time-resolved mass spectra obtained from Al/CuO thermite reaction

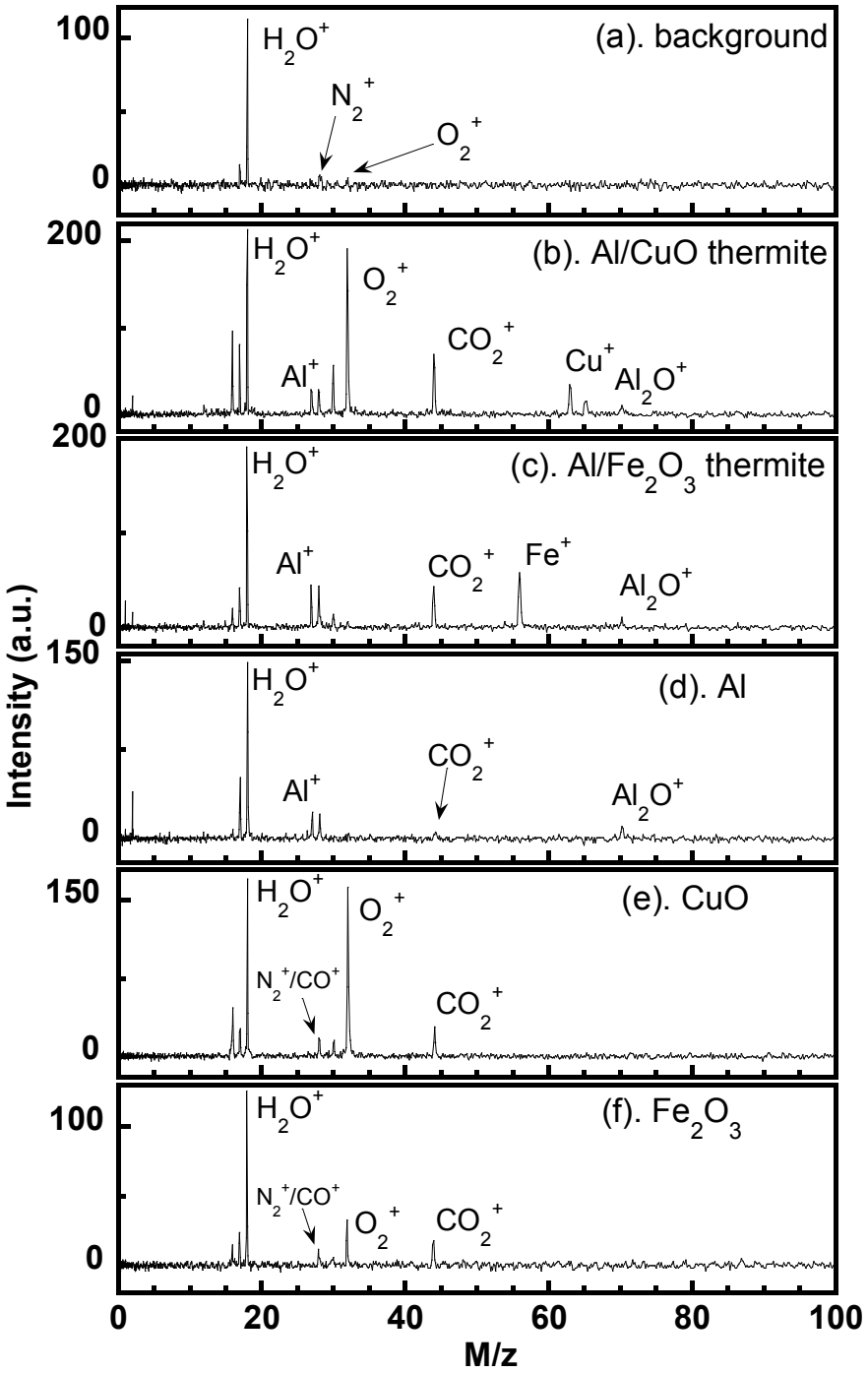

Figure 6.4 Detailed views of selected mass spectra obtained from T-Jump experiments (a) background, (b) Al/CuO mixture (c) Al/Fe_2O_3 mixture (d) Al particles (e) CuO particles (f) Fe_2O_3 particles

Al/CuO and Al/Fe_2O_3 nanocomposite mixtures, as well as aluminum, CuO, Al_2O_3 and Fe_2O_3 nanoparticles were examined under rapid heating conditions. In each heating event, the T-jump probe was heated to ~1700 K with a ~3 ms voltage pulse, so that the heating rate is about 5×10^5 K/s Simultaneously, a sequence of 95 spectra with m/z up to 400 was recorded with a temporal resolution of 100 μs per spectrum. An example mass spectra for rapid heating of a Al/CuO sample were shown in Figure 6.3. The first 41 mass spectra out of total 95 spectra are plotted, which corresponds to 0 to 4 ms of reaction time. The mass spectra in Figure 6.3 clearly show the progression of the reaction as ion-species appear and then decay away. Similar results were obtained for other samples, but due to limitations of space, we select only one mass spectrum for each measurement, which provides an instantaneous snapshot of a reaction event for a particular stoichiometry or mixture and display the result in Figure 6.4. At the start of the heating event, t = 0, the spectrum recorded is that of the background in the ion source region, which consists of water (m/z 18) as a primary species, and a small amount of N_2 (m/z 28) and O_2 (m/z 32) as shown in Figure 6.4 (a). OH^+ ions (m/z = 17) from e-impact fragmentation of water are also observed. As time advanced to the ignition point, the thermite reaction is initiated, and new peaks corresponding to reaction products can be observed. Figure 6.4 (b) is a typical mass spectrum for Al/CuO nanocomposite thermite reaction. New species of O (m/z = 16), Al (m/z =27), CO_2 (m/z = 44), Cu (m/z = 63, 65) and Al_2O (m/z = 70) are identified. Similarly, figure 6.4 (c) is a mass spectrum obtained from an Al/Fe_2O_3 nanocomposite experiment. New species of Al (M/z =27), H_2CO (m/z =30), CO_2 m/z = 44), Fe (m/z = 56) and Al_2O (m/z = 70) are identified. No mass-spectral signals are

observed that correspond to the hexane solution used to coat the particles, indicating that the sample is free of solvent effects. One significant difference in Al/Fe_2O_3 mass spectrum is the O (M/z = 16) and O_2 (M/z = 32) peak. Those peaks can be observed in Figure 6.4 (c) but their intensities are much smaller than the Al/CuO case.

The mass spectra showed in figure 6.4 (b) and (c) enable us to identify the thermite reaction products. We first categorize these observed species into three groups. Species of Al, Al_2O, Cu, and Fe are the first category. Species of CO, H_2CO and CO_2 all contain carbon and are probably originated from the same source. Oxygen species O is presumed to be from fragmentation of the O_2 molecule during electron beam ionization, and form the third category. The species in the first category are compounds from nanocomposite thermite, and are apparently coming from thermite reaction. However the origin of the other species is ambiguous, by simply comparing with the background mass spectrum. Therefore, similar experiments were conducted for Al, CuO and Fe_2O_3 powders without mixing with their corresponding co-reactant and shown in Figure 6.4 (d), (e) and (f), respectively. Al and Al_2O are observed in Figure 6.4 (d) by simply heating Al powder. The Al_2O species is probably resulting from Al_2O_3 shell, while the Al peak suggests that the Al core will melt and leak out or diffuse out from the shell under heating. This has been previously observed by us in slow heating TEM imaging.[28, 150] Notice from Figure 6.4 (e) and (f) that species of CO, H_2CO and CO_2 are only observed from heating of CuO and Fe_2O_3 particles. We also notice that the intensity of the water signal increases upon heating indicating that the powders have absorbed water. It is well know that water catalyzes the formation of copper carbonate ($CuCO_3$) shell on

CuO particles or an iron carbonate ($FeCO_3$) shell on Fe_2O_3 particle formed. Upon heating the carbonate shell decomposes to liberate, CO, H_2CO and CO_2 as identified in the spectra. Presumably this carbonate layer is only on the surface of particles, and should be very thin. The species in the third group (O, O_2) are of particular interest as free oxygen could be a key component in the reaction dynamics. As we can see in Figure 6.4 (d), (e) and (f), no oxygen species are observed in heating of Al powder but a significant amount of O_2 is released from heating of CuO and Fe_2O_3 powder, implying that the oxygen observed during the thermite event are from the metal oxide particles. In addition, no Cu or Fe species is observed upon heating of CuO or Fe_2O_3 powder (figure 6.4 (e) and (f)), implies that the Cu or Fe peak observed in the thermite experiments should be a product from the thermite reaction.

As mentioned above, the mass spectra were recorded in a time-resolved manner. The normalized peak intensity of some major peaks as function of time are plotted and shown for an Al/CuO and Al/Fe_2O_3 in Figures 6.5 (a), (b) respectively. For both metal oxides we see that group 2 species CO (m/z = 28) and CO_2 (m/z = 44) appear before species from other groups, implying that the carbonate layer is first removed by thermal decomposition before the thermite event commences. As time advanced to ~ 1.8 ms in Figure 6.5 (a) (Al/CuO mixture) or ~2.5 ms in Figure 6.5 (b) (Al/Fe_2O_3 mixture), species of Al, Al_2O, Cu and O_2 (for Al/CuO) or Al, Al_2O and Fe (for Al/Fe_2O_3) begin to appear and ignition is considered to occur. The significant difference between Al/CuO system and Al/Fe_2O_3 system is the formation of oxygen species. The mass spectra of Al/CuO reaction show a strong O_2 peak, with a temporal profile (Figure 6.5 (a)) following the same trend as other species, implying that

oxygen is a reactive species, and involved in the thermite reaction. On the other hand, there is only a minor O_2 peak observed in mass spectra of the Al/Fe_2O_3 mixture reaction, despite the fact that oxygen release is observed in the heating of Fe_2O_3 particles. It is very likely then that O_2 formation from the metal oxide is important in the initiation of the thermite reaction. The oxygen specie is not only an oxidizer but may also behave as an energy propagation media that carries heat to neighboring particles, therefore, in contrast to the Al/CuO system where oxygen is generated in abundance, oxygen formation may become the limiting step for the Al/Fe_2O_3 reaction, and as a result, the Al/Fe_2O_3 reaction is much less aggressive compared to the Al/CuO system, despite the fact that their adiabatic temperatures do not differ significantly (Al/CuO 2837K VS Al/Fe_2O_3 3135K at atmospheric pressure, from NASA CEA calculation). Based on these mass spectrometric observations, we can conclude that the reaction of the nanocomposite thermite system occurs in the following steps: (1) decomposition of $CuCO_3$ or $FeCO_3$ shell, (2) CuO or Fe_2O_3 decomposition ($4CuO \rightarrow 2Cu_2O + O_2$ or $6Fe_2O_3 \rightarrow 4Fe_3O_4 + O_2$), and melting and release of the Al core, (3) Al reacting with oxidizers.

As a complement to the T-Jump/MS experiments, the optical emission from nanocomposite thermite reaction was also measured at atmospheric pressure. The optical emissions for these reactions, after background corrections, are shown at the bottom of Figure 6.5 (a) for Al/CuO and (b) for Al/Fe_2O_3. The rapid rise in the optical signal indicates the onset of ignition. There is slight difference in the time to ignition as observed through the PMT due to experimental run-to-run uncertainty. Hence, the PMT signals have been presented with a small time offset to compare with the MS

signal. The widths of the PMT trace are ~ 1.5 ms and ~1.1 ms for Al/CuO and Al/Fe_2O_3 respectively, and agree with the MS signal very well. These also indicates that the combustion time as measured mass-spectrometrically and optically are consistent and provide a measure of the reaction time.

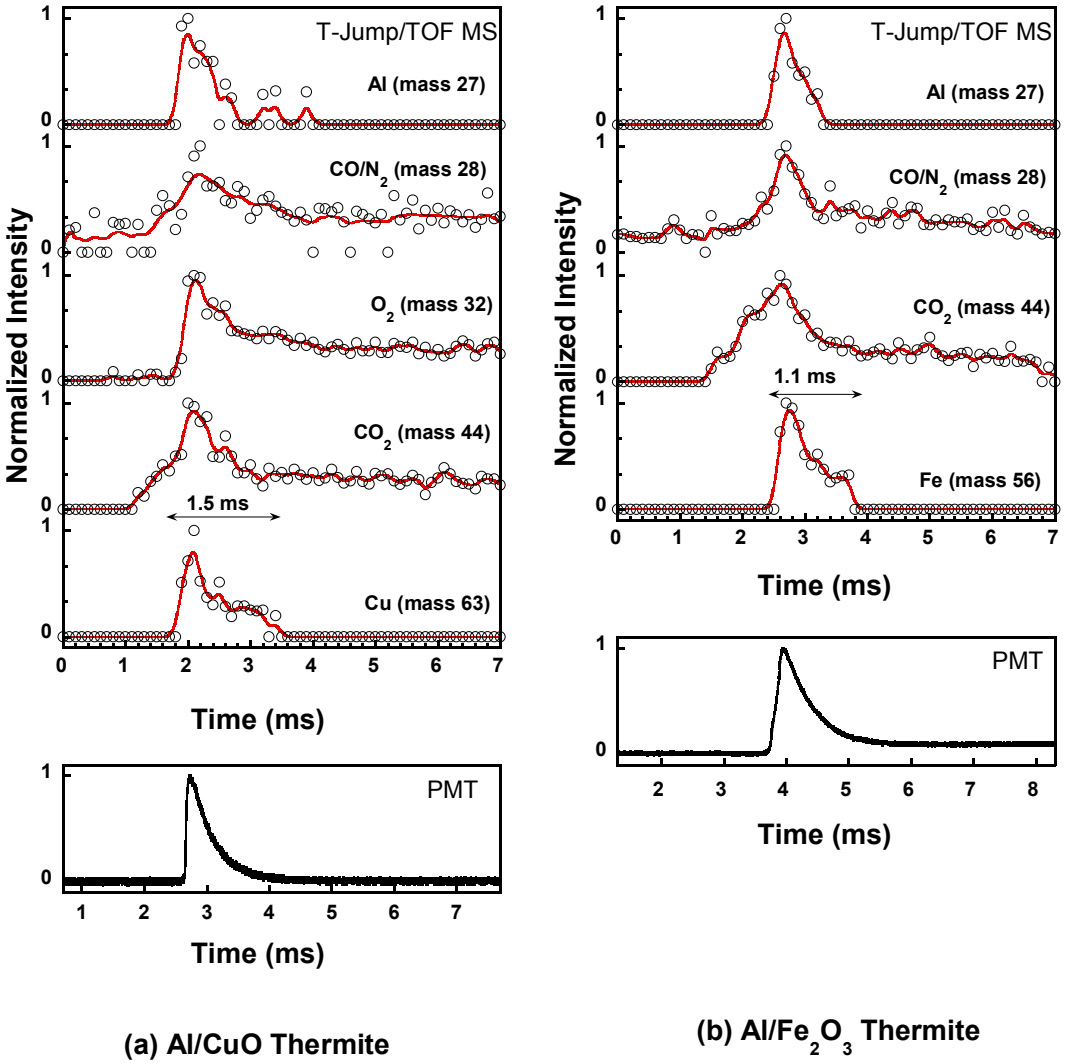

Figure 6.5 Normalized peak intensities as function of reaction time for reaction species observed in (a) Al/CuO reaction, (b) Al/Fe_2O_3 reaction, the bottom plots are optical signal measured from separated experiments, the time axis are shifted to compare to MS signal

Since the optical measurements were conducted in air, while the MS measurement was in vacuum, this result suggest the presence of oxygen in air has little effect on the thermite reaction compare to the oxygen released from the oxidizer particles. If one assumes a mass transfer limited mechanism, and compares the amount of oxygen liberated from decomposition of the oxide with the amount of oxygen in air we can estimate the relative importance of these two sources of oxygen. Since particles are loosely packed in our experiments, we consider a control volume, where an aluminum particle mixed with a CuO particle to form stoichiometirc mixture (based on reaction 2Al + 3CuO -> Al_2O_3 + 3Cu), then the oxygen concentration in this unit cell due to CuO decomposition is given by

$$C_{O2} = \frac{\eta m_{O_2}}{V} = \frac{3\eta M_{O_2}}{8VM_{Al}} m_{Al} \tag{6.1}$$

where η is particle packing density, V is the volume of the particles, M_{O2}, M_{Al} are molecular weight of oxygen gas and aluminum, respectively, and m_{Al} is the mass of the aluminum particle. For 50 nm aluminum particle and 15% packing, the oxygen concentration is estimated to be ~ 55 kg/m^3. On the other hand, the oxygen concentration in the control volume due to ambient air is 0.27 kg/m^3 at room temperature, and only 0.06 kg/m^3 at 1300K, and thus about 3 orders of magnitude less than the oxygen liberated from the CuO particles. This calculation suggests the metal oxide particles behave as an oxygen storage device, and can release oxygen very fast to initiate the reaction. This may also explain while aluminum particles burn much faster if mixed with metal oxide, than combustion in air. Additional optical measurement experiment carried out in an argon environment, are essentially indistinguishable from that in air, corroborating the above analysis and conclusion.

To further understand the mass spectrometric observation, thermal equilibrium calculations were conducted for Al/CuO and Al/Fe_2O_3 system using NASA CEA code. The system pressures were varied from room pressure to 10^{-11} atm, and the calculated mole fraction of the resulting species were compared with the relative peak intensity measured from mass spectra. However, no good agreement can be found between the experimental results and the calculated mole fraction of reaction products. The thermal equilibrium calculation results show that Cu or Fe are dominant gaseous species, and the mole fraction of Cu or Fe are several orders of magnitude higher than gaseous Al or Al_2O. In contrast the mass-spectra result shows that the oxide metal and that of Al are comparable. Another species predicted by the equilibrium calculation is AlO, the mole fraction of gaseous AlO is slightly higher than that of Al_2O, however we only observed Al_2O, except under rich conditions (not discussed in this work). These results imply that the combustion in the T-Jump experiments results in a highly non-equilibrium distribution of species.

6.3.2 Powder Temperature and Heating Rate

The heating rate is an important factor and has significant effect on the ignition and reaction pathways of the thermite systems. One advantage of the T-jump technique is that the heating rate can be easily varied through tuning of the heating pulse and voltage. We conducted experiments for Al/CuO and Al/Fe_2O_3 nanocomposites at different heating rates to examine the effect of heating rate on ignition temperature. Four different heating rates were selected in the range from 10^4 to 10^5 K/s and five experiments were performed for each heating rate. The time resolved mass spectra as well as the voltage and current traces were recorded, and the

probe temperature estimated from the change in resistivity of the platinum wire by using Callendar-Van Dusen equation.[151] However, there is a major drawback of this method. The powder temperature can be different than the filament/wire temperature, and we are only able to directly measure the wire temperature by this method. Therefore, a heat transfer model is required to estimate the true sample temperature during the heating event for processing our experimental data.

Recently, Ward et. al. developed a heat transfer model to study of the ignition of Mg powder coated on a hot filament.[111] In that work, powder packing was treated as individual layers of particles, and the temperature of each layer was calculated. A similar but simplified approach is used in this work. The packing geometry of the powder coating is shown in Figure 6.6. Based on the ideal packing model, and coating thickness estimated from an SEM image (Figure 6.1), the total number of layers can be calculated. If we assume particles in the same layer to have the same temperature, then the heat transfer process can be modeled in two steps. First the filament is heated by an electrical current, and then the powder is heated by the energy transferred through particle layers and thermal radiation. As time advances, and the thermite reaction is initiated, the energy transfer between the filament and the sample is decoupled. The thermite reaction can generate enough energy to sustain the combustion and further ignite the reaction in neighboring layers. Here the assumption of the decoupling between the filament and powder after ignition is based on the following experimental observations: (1) Our probe is a very thin wire and powder is loosely coated on the wire. (2) Little powder residue is observed after

the heating event. (3) Sparks are observed coming off from the probe during the combustion event.

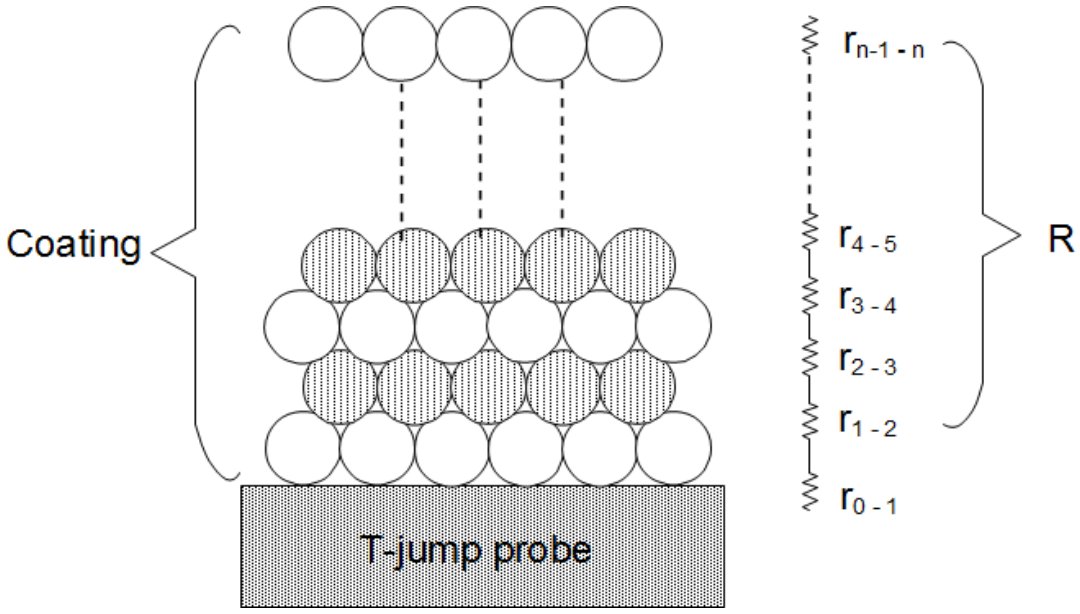

Figure 6.6 Geometry of powder coating on T-jump wire

The total energy input used to heat both the filament and the powder for each heating experiment can be calculated using the measured voltage and current of the heating pulse. The heat transfer between the filament and powder is coupled by the thermal contact resistance as shown in Figure 6.6. The thermal resistance between particle layers under ideal packing conditions is given by[111]

$$r_{n-1\,-\,n} = \alpha \cdot \frac{r_{contact}}{3n_{layer}} \tag{6.2}$$

and the bulk thermal resistance is

$$R_{bulk} = \sum_{1}^{N} r_{n-1\,-\,n} \tag{6.3}$$

where n_{layer} is the number of particles in the n*th* layer. The factor 3 is due to the fact that each particle has 3 contacts in an ideal packing condition, and it should be change

to 1 for particles in contact with the T-jump probe. α is the correction factor that account for non-ideal packing density, and larger than 1 if the packing is not ideal. $r_{contact}$ is the resistance of each particle contact and can be calculated from the bulk thermal diffusivity, bulk density and particle size. In the methodology developed for modeling heat transfer in multilayer powders, Ward et. al. have calculated the contact resistance for their micron-sized particles.[111] Here we can assume the contact resistance is material independent, and the contact resistance for our nano-sized particles can be estimated by considering the particle size effect.

With the knowledge of powder packing, input energy and thermal resistance between particle layers, we can calculate the probe and sample temperature as a function of time. However, since there are more than a thousand layers estimated from the ideal packing model, it is difficult to calculate the temperature for each individual layer. A first attempt to calculate the temperature was made by assuming no temperature gradient inside the sample and the multilayer powder is simplified to monolayer powders with thermal resistance R_{bulk} between the probe and powder. Results suggest the powder can only be heated to about 500K at the time ignition was observed in the mass spectrum for heating rates of ~10^5 K/s. This ignition temperature is apparently too low and therefore the simplification is not acceptable. Ward et. al. showed that the temperature in the multilayers powders are non-uniform, and the temperature profile inside powders is heating rate dependent.[111] For the highest heating rate in their work (~17000K/s), the temperature profile is actually uniform except for the first layer which is in contact with T-jump probe. Since we are heating at a rate an order of magnitude greater, this result suggests that we can

simplify the heat transfer process by treating multilayer powder as two parts. As indicated in Figure 6.6, the particles in the first layer are coupled with the T-jump probe by thermal resistance $r_{0\text{-}1}$ and the rest of the powders are considered as a monolayer and coupled with the first layer by thermal resistance R. Under such assumptions, the temperature of the wire, the temperature of the first layer and the rest of the powder can be calculated from experimentally measured voltage and current data. The thermal radiation is also considered but simplified by only considering the emission from the filament and absorption by particles in the first layer. The energy balance for wire is

$$I^2 r_{wire} = \frac{(T_{wire} - T_{layer1})}{r_{0-1}} + \varepsilon\sigma A T_{wire}^{\ 4} + m_{wire} c_{wire} \frac{dT_{wire}}{dt} \tag{6.4}$$

where I and r_{wire} are the heating current and wire resistance obtained from the measured voltage and current traces. $r_{0\text{-}1}$ is the thermal resistance between wire and the first layer powder, ε is the emissivity of the platinum wire, A is the surface of the platinum wire. m_{wire} is the mass of the wire and c_{wire} is the wire specific heat, the energy balance for the first layer and the rest of powders are

$$\frac{(T_{wire} - T_{layer1})}{r_{0-1}} + \varepsilon\sigma A T_{wire}^{\ 4} = \frac{(T_{layer1} - T_{layer2})}{R} + m_{layer1} c_{powder} \frac{dT_{layer1}}{dt} \tag{6.5}$$

$$\frac{(T_{layer1} - T_{layer2})}{R} = m_{layer2} c_{powder} \frac{dT_{layer2}}{dt} \tag{6.6}$$

respectively. R is the thermal resistance between layer 1 and layer 2 and c_{powder} is the bulk specific heat of the powder.

Figure 6.7 shows results of the filament temperatures calculated from data of an Al/Fe_2O_3 heating experiment. Different packing densities were used as input parameters in the calculation, and different temperature-time trajectories were obtained. The highest possible filament temperature is obtained by assuming all the energy is used to heat the filament, with no heat transfer from the filament to the powder. As previously mentioned, the resistance change of the T-jump filament can be used to estimate the filament temperature, and the result is plotted in Figure 6.7 for comparison. It can be seen that the model result of 20% packing density matches the temperature calculated from wire resistivity very well. Furthermore, the resistance estimated temperature curve shows a significant change in slope (heating rate) at the ignition point, and our model predicted a similar behavior, validating the assumption of decoupling of the filament and sample powder after ignition. The same calculations were performed for all experiments and we found that the resistance estimated temperature fell between the 10% ~20% packing curve for most of our experiments. Hence, this model can be used to determine the temperature and the heating rate enabling us to further investigate the ignition and heating rate effect on thermite reactions.

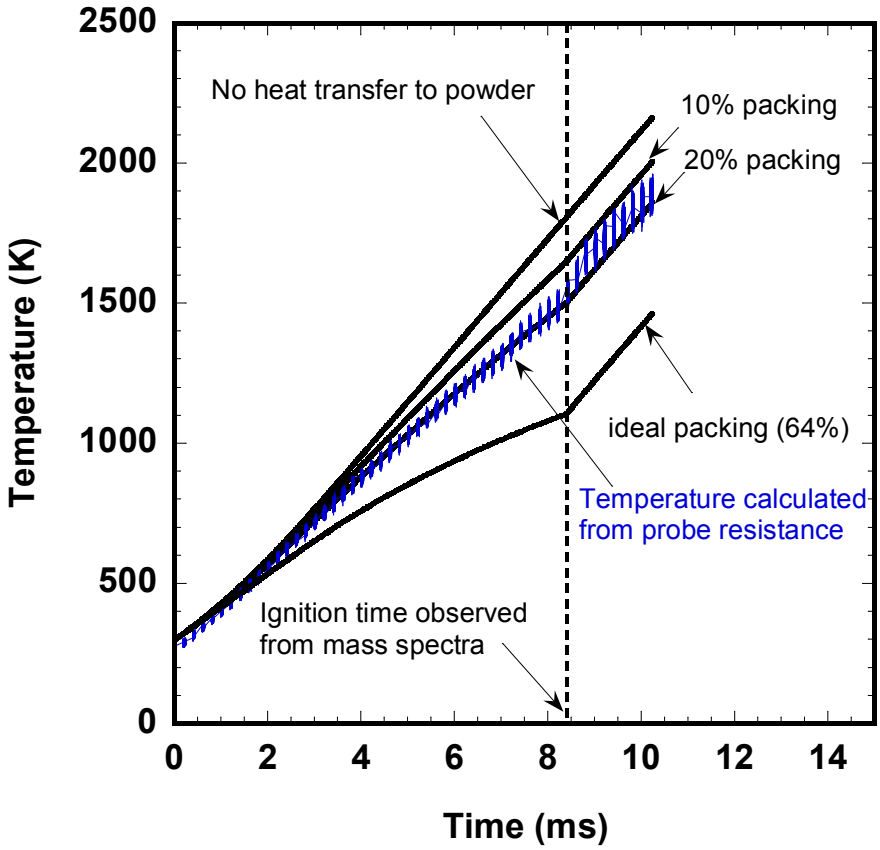

Figure 6.7 T-jump wire temperature histories calculated from model compare with calculated from wire resistance change

Using the reasoning above, we can use the 20% packing density as an input parameter for our temperature calculation. The local heating rate at the ignition point is used and is determined from the slope of the temperature vs. time curve at the ignition point. The results show that there is no significant temperature difference between the filament and the first layer of particles (no more than 5^{o}C at the time of ignition), but large temperature differences for the first layer and rest of the powder. The calculated powder temperature varied depending on the heating rate. For the lowest heating rate(5×10^{4}K/s) used in our experiments, the powder (except the first layer) can only be heated to at most 600K when the ignition occurs, and the powder

temperature is less than 400K for the highest heating rate (8×10^5 K/s) used in the experiments. These results suggest that the first layer temperature profile immediately follows the wire temperature and ignites first, and once the combustion is initiated in the first layer, the reaction propagates through the powder and ignites the rest of the thermite. The experimentally measured flame propagation speed is of the order of 10^2 m/s,[18, 21] so it only takes ~0.5 μs for the complete ignition of 50 μm powder layers. Compared to the time resolution for mass spectrometric measurements of 0.1 ms per spectrum, this time difference can be ignored and the whole of the powder can be considered to have ignited.

Figure 6.8 shows the ignition temperatures of Al/CuO and Al/Fe_2O_3 nanocomposite systems as a function of heating rate. The heating rates were varied in the range from 10^4 to 10^5 K/s and each point is an average of 5 experiments. It can be seen that the ignition temperature for both systems increased as heating rate increased as one would expect. The Al/CuO mixture ignited in the temperature range of 800K to 1300K, and the Al/Fe_2O_3 mixture ignited from 1000K to 1900K depending on heating rate. The Al/Fe_2O_3 mixture has higher ignition temperatures than Al/CuO mixture in the range of the heating rates studied here, and all the ignition temperatures are well above the melting point of Al (933K). This implies that if the process of melting of the Al particle has significant impact on the ignition of thermites, it cannot be the sole factor that dominates initiation of the reaction. Both the melting of Al particles and the formation of oxygen from the metal oxide particles, and their contribution to the overall reaction could be dependent on the heating rate. For the heating rates investigated in this work, the oxygen formation

should be the dominant factor for reaction initiation, and the fact that Fe_2O_3 releases less oxygen than CuO leads to the higher ignition temperature of Al/ Fe_2O_3 system. We believe that the reactivity of a thermite system may be correlated with the amount of oxygen the oxidizer particles generate, and the formation of oxygen from oxidizer particles would be a future objective of research.

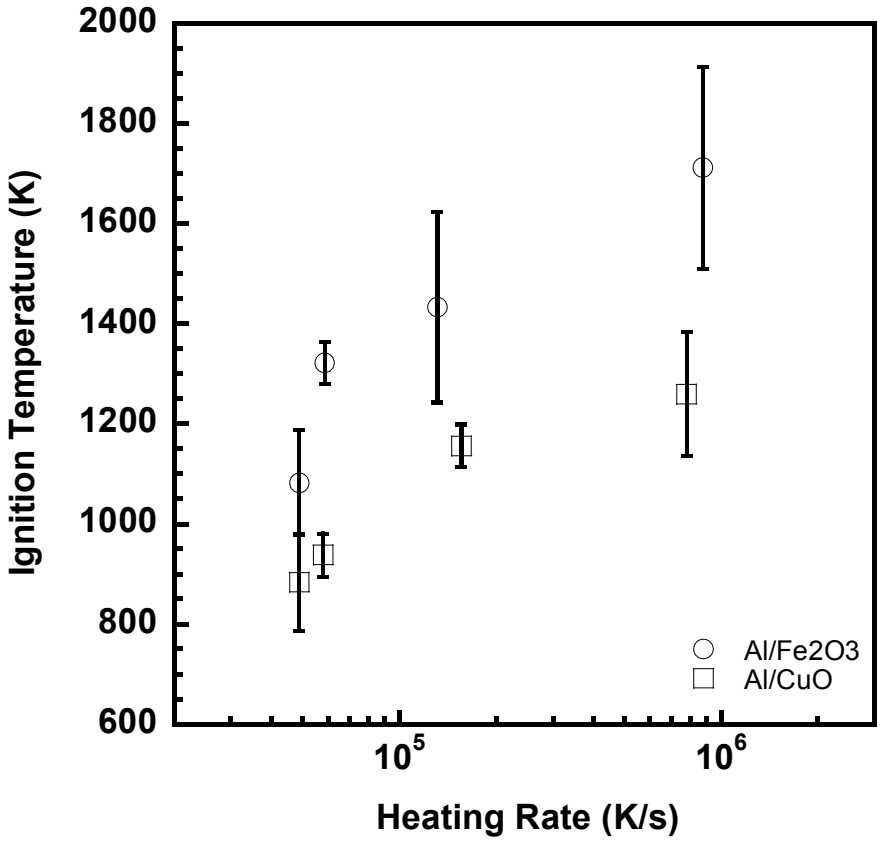

Figure 6.8 Measured ignition temperature as function of heating rate

6.4 Conclusions

In this work, Al/CuO and Al/Fe_2O_3 nanocomposite thermite reactions were investigated for the first time by a recently developed T-jump/TOF mass spectrometer. Experimental results suggest high degrees of ionization during thermite reactions. This phenomenon can disturb the ion extraction process of a mass spectrometer and therefore the ion source region needs to be operated at ground state for mass spectrometric measurements of thermite reactions.

Time resolved mass spectra were obtained for the reaction of Al/CuO and Al/Fe_2O_3 nanocomposites, and species of Al, Al_2O and Cu/Fe were observed. Mass spectra analysis suggests the decomposition of the oxidizer particles to form oxygen as well as Al diffuse out from oxide shell are initial steps of the thermite reactions. Following these initial steps, the Al reacts with the oxidizers to form Al_2O. A heat transfer model was developed to determine the onsite temperature and heating rate, and the thermite reactions were investigated under different heating rates. The spectral analysis and ignition temperature data support the theory that the formation of oxygen from oxidizer particles may be the important factor for reaction of nanocomposite thermite mixtures and would be worthy of further investigation. The results obtained from the T-Jump/TOF mass spectrometer show promising features of this instrument. Effects of the equivalence ratio, particle size or new additive effects on nanocomposite thermites as well as detailed kinetic studies should be the subject of future investigations using the T-jump/TOF mass spectrometer.

Chapter 7

Summary

7.1 Conclusion of this work

The recent advances in nanotechnology have created many nanoscale materials and devices with entirely new properties. The spotlight of current research interests are focused on exploring the novel properties of these materials. Knowledge on the characteristic behaviors of nanostructure materials is essential for understanding their capabilities and identifying their potential utilizations. The objective of this work is to develop novel diagnostic tools and methods to characterize nanomaterials and provide a better understanding on the underlying nature of reactivity and properties of this class of materials.

The theme of this thesis can be considered two fold. First, to study the intrinsic properties of individual nanoparticle and provide information on how reactive a material is for the intend applications. And second, explore the reactivity of nanocomposites and probe the reaction between nanoparticles. Chapter 2, chapter3, and chapter 4 are devoted to the first theme. In these chapters, we demonstrate the development of ion-mobility and mass spectrometry methods and their application on charactering the intrinsic reactivity of individual nanoparticle. Chapter 5 and chapter 6 are dedicated to the second theme and present the development of a new T-Jump/TOF Mass Spectrometry to probe solid phase reactions between nanocomposite particles.

Tandem ion-mobility spectrometry is a well established technique in aerosol community. Chapters 2 described the application of this approach toward the use of novel nanoscale reactive material as energetic materials. The ion-mobility approach offers the advantage of manipulating nanoparticles on the fly by means of electric classification, which promote it to an ideal candidate for tracking the change of a individual nanoparticle undergo upon a chemical/physical process. Here we combine two ion-mobility spectrometry approaches, tandem differential mobility analysis (TDMA) and tandem differential mobility – particle mass analysis (DMA-APM) to probe the size resolved oxidation kinetics of nickel nanoparticles, with the focus of their potential use as a fuel in energetic materials.

In chapter 3 and chapter 4, we focusd on the characterization of laser ablation/ionization single particle mass spectrometry, with the goal of quantitatively characterize the size, elemental composition, and gas-particle reactivity of nanoparticles using SPMS. Chapter 3 showed the hydrodynamic simulation on the characteristic behavior of ions produced from aluminum nanoparticle that are heated and ionized by a pulsed laser. We focus on regimes of laser width from 0.01 ns to 10 ns (532 nm wavelength, 100mJ/pulse) and particle size (20 - 400 nm in diameter) most relevant to commonly used SPMS, and determine the temporal evolution of ionization state and energy of ions generated during the laser-particle interaction. With this knowledge, we conducted further experimental investigation on the SPMS and the complete ionization technique. The results were discussed in chapter 4, and suggested that there are component and morphology biases on the quantification of

MS signal, which can be related to the high nonlinear properties of the laser-particle interaction.

Chapter 5 describes a new T-Jump/Time-of-Flight mass spectrometer (TOFMS) that is developed for time resolved analysis of the ultrafast condensed phase reaction. This instrument is designed to characterize chemistry under high heating rate conditions (i.e. fast chemistry), and conduct the experiments under conditions where the secondary gas phase chemistry can be minimized. The essence of the experiment is that the T-Jump probe is directly inserted into the Electron Ionization chamber of the mass spectrometer, and the species from T-Jump excitation are monitored by the TOF mass spectrometer continuously. As the first application of this instrument, nanocomposite thermite systems of aluminum/copper oxide (Al/CuO) and aluminum/iron oxide (Al/Fe_2O_3) were studied and the results are discussed in chapter 6.

7.2 Future Work

The work highlighted in this thesis links aerosols science, nanoparticles research and energetic materials, three methods were developed from aerosols based concepts: tandem ion-mobility spectrometry, single particle mass spectrometry and T-Jump/TOF mass spectrometry, to probe the properties and reactivity of nanoparticles and nanocomposites with a focus on the energetic materials. The future extension of this work would involve further development and improvement of these techniques and their applications for studying other properties of nanoparticles, as well as

detailed investigation on reaction mechanism and pathways of nanocomposite thermites using T-Jump/TOF mass spectrometry.

Based on the results and discussions presented in chapter 3, the main concern for SPMS determination of particle size and composition is the low detection sensitivity for highly energetic ions. The low transport efficiency of ions through the TOF tube not only limits our ability of characterize smaller particles, but also introduces a detection bias against the surface species. Moreover, chapter 4 shows that there is a component and morphology bias on the complete ionization technique for multi-component inhomogeneous structured particles due to the complex nature of the laser-particle interaction process. Thus, to achieve the goal of quantitative characterization of individual aerosol particles using single-particle mass spectrometry, it becomes imperative to improve the existing design.

Essentially there are two possible approaches to enhance the sensitivity of SPMS. One is to develop a new system to improve the transport efficiency of ions through the TOF tube. An Einzel lens system has been integrated into our SPMS, with appropriate lens voltages so that ions with high kinetic energies can be focused to prevent loss in the TOF tube. Figure 7.1 shows the SIMION simulation results of the DE at various lens voltages for different initial ion kinetic energies and Figure 7.2 is the experimental results for Einzel lens effects on aluminum particle detection. Those results clearly show that the detection sensitivity of SPMS can be effectively increased by employing the Einzel lens system.

In addition to improving the design with the ion optics system, there have been efforts to modify the ionization technique. Ideally high ionization efficiency but

low initial ion kinetic energy is preferred. As described in chapter 5 and chapter 6, an Electron Ionization (EI) approach is currently used as a secondary ionization source. EI requires that the particle first be pre-vaporized/atomized into gaseous form. Electrons with 70 eV energy are usually employed in the ion source region. The analyte molecules or atoms are impacted with energetic electrons, the interaction process results in energy absorption of analyte and ejection of thermal electrons as shown in the following equation:

$$M + e^-_{(70eV)} \rightarrow M^+ + e^-_{(50ev)} + e^-_{thermal} \tag{7.1}$$

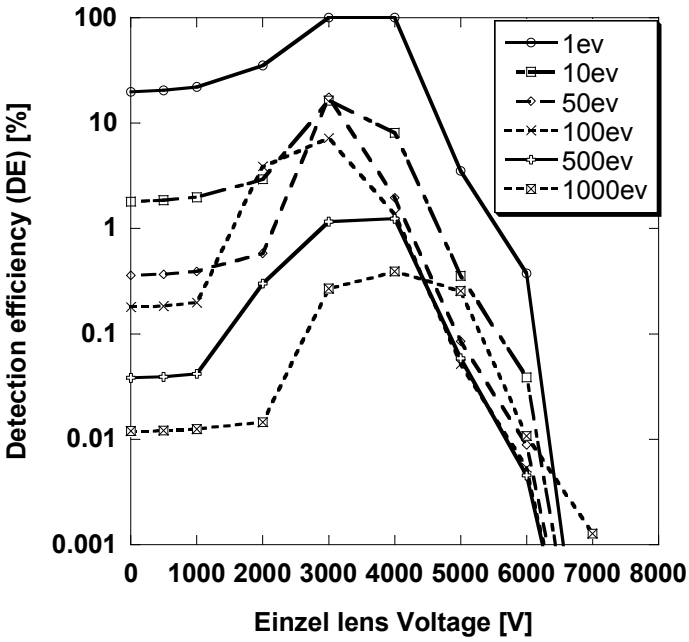

Figure 7.1 Simulation of Einzel lens effect on detection efficiency.

The remaining energetic electrons can interacte further with other analyte atoms. Compared with the current laser power level, a lower fluency laser coupled with EI would presumably result in the formation of low ion kinetic energies, while still guaranteeing efficient ionization.

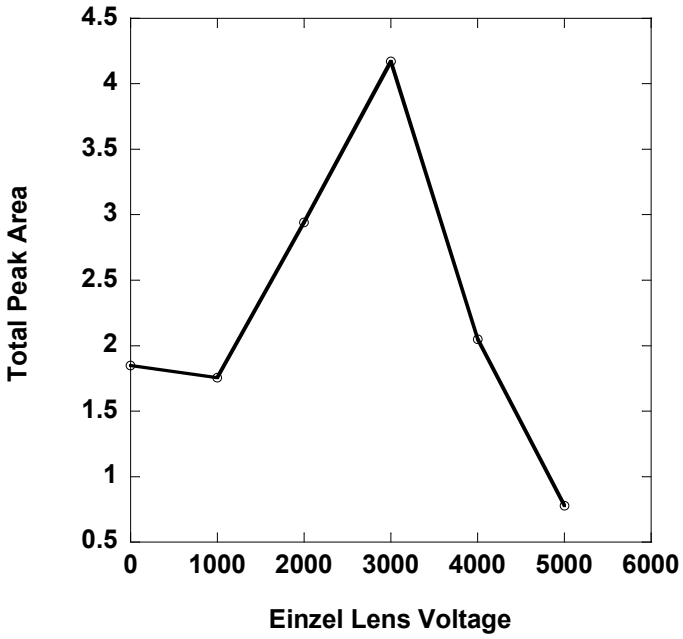

Figure 7.2 Experimental result of Einzel lens effect on aluminum particles detection

In this work, we have demonstrated the capabilities of tandem DMA and DMA-APM approaches for tracking the intrinsic reactivity of metal nanoparticles. This idea can also be extended to study other properties of nanoparticles. For instance, this technique has been employ by our group to measure the surface energies of Zn nanoparticles, as well as study the size dependent hydrolysis of Zn nanoparticles for the potential applications of Zn nanoparticles in thermo-chemical solar hydrogen generation. The future development on this method would involve on the integration of mobility techniques with other existing experimental diagnostic tools for tandem measurements on properties of nanoparticles. The recent advancements of tandem ion-mobility techniques have been reviewed by Park et. al..[152] This scheme can also be extended with the T-Jump/TOF mass spectrometer to study size-resolved reactions of nanocomposite thermites. The possible

experimental setup would involve using DMA to size select nanoparticles for deposition on the T-Jump probe, and subsequentially conducting ignition experiments.

In chapter 6, we observed high degrees of ionization occurring in thermite reactions. Similar phenomenon such as transient electric field formation and nonequilibrium high energy radiation that associated with the combustion of thermites were also reported by others.[145-149, 153] Further investigations on these interesting observations would certainly benefit our overall understanding of nanocomposite reactions

As an attempt to investigate the ionization process, we conducted experiments to measure the ions and electrons generated from Al/CuO nanocomposite thermite. In the experiments, the sample probe was inserted in between the repeller plate and ion extraction plate and the electron beam was turned off. This allowed the spectrometer to sample the ions generated from thermite reaction. For positive species extraction, the repeller plate, ion extraction plate and acceleration plate were biased to ground, -50V and -1500V respectively, and biased to ground, +50V, +1500V for negative species extraction. The Al/CuO nanocomposite thermite samples were rapid heated and ignited with a ~ 3 ms heating pulse, the positive ion and negative ion/electron signals were shown in Figure 7.3 (a) and (b), respectively. The detailed view of the signals as well as the voltages applied on the extraction plate was also shown in the figures.

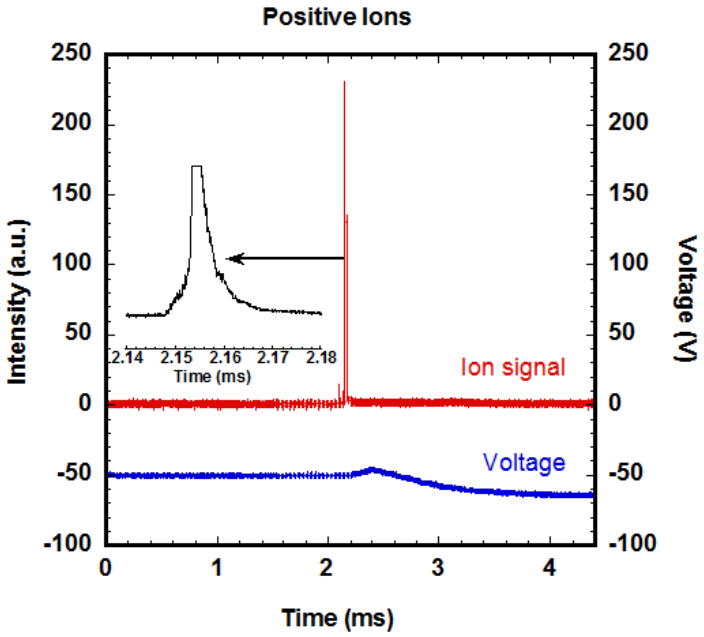

(a)

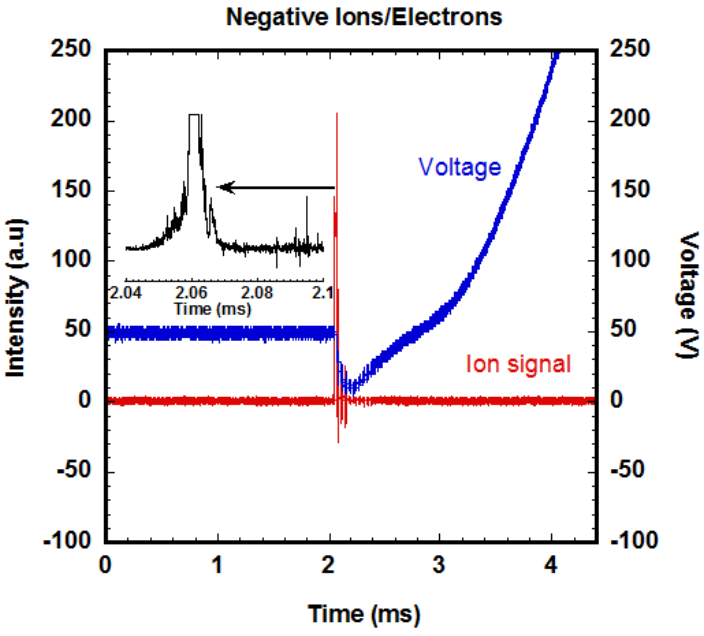

(b)

Figure 7.3 (a) the positive ion (b) negative ion/electron signals measured from Al/CuO thermite reaction by T-Jump/TOF mass spectrometer.

Strong ion signals were observed from the initiation of thermite reaction, the zoom-in view of the signals show that both the positive ions and negative ions/electron signal saturate the scope, suggesting there are high degrees of ionization when thermite reaction initiated. Moreover, this ionization process is extremely short as the signal shown in Figure 7.3 (a), (b) only have a ~20 us peak width. As we see in the chapter 6, the mass spectra measurement show a much longer reaction time, about 1 ms, for Al/CuO nanocomposite thermite reaction. Now we further examine the voltage profile shown in the figures, we can see that the positive ions only slightly perturb the voltage while negative ions/electrons significantly alter the voltage. Since part of positive ions or negative ions/electrons was collected by the extraction plate during the ion extraction, these results imply that there are more negative species generated than positive species during the ionization process. Notice that the ions were continuously extracted in the experiments, therefore we are not able to identify the ion species. Further experiments for the ion species identification and electron density profile measurement are required. We believe the study of ionization during thermite reaction can provide important insight on the initiation of thermite reaction and may lead to a better understanding of the reaction process of nanocomposite thermite.

References

1. Friedlander, S.F., *Smoke, Dust, and Haze*. 2 ed. 2000, New York, NY: Oxford University Press, Inc.
2. Hinds, W.C., *Aerosol Technology: Properties, Behavior, and Measurement of airborne particles*. 2 ed. 1999, New York, NY: John Wiley & Sons, Inc.
3. Suess, D.T. and K.A. Prather, *Mass Spectrometry of Aerosols.* Chem. Rev., 1999. **99**(10): p. 3007-3036.
4. Park, K., D. Lee, A. Rai, D. Mukherjee, and M.R. Zachariah, *Size-Resolved Kinetic Measurements of Aluminum Nanoparticle Oxidation with Single Particle Mass Spectrometry.* J. Phys. Chem. B, 2005. **109**(15): p. 7290-7299.
5. Mahadevan, R., D. Lee, H. Sakurai, and M.R. Zachariah, *Measurement of Condensed-Phase Reaction Kinetics in the Aerosol Phase Using Single Particle Mass Spectrometry.* J. Phys. Chem. A, 2002. **106**(46): p. 11083-11092.
6. Ortega, A., *The kinetics of solid-state reactions toward consensus part I: Uncertainties, failures, and successes of conventional methods.* International Journal of Chemical Kinetics, 2001. **33**(6): p. 343-353.
7. *ICT Database of thermochemical values*. 2001, Pfinztal, Germany: Fraunhofer Institut für Chemische Technologie:.
8. *CRC Handbook of Chemistry and Physics*. 2002: Hampden Data Services Ltd.
9. Thomas N. Hall, J.R.H., *Navy Explosives Handbook, NSWCMP 88-116*. 1988.
10. Son, S.F., R.A. Yetter, and V. Yang, *Introduction: Nanoscale composite energetic materials.* J. Propul. Power, 2007. **23**(4): p. 643-644.
11. Pantoya, M.L. and J.J. Granier, *The effect of slow heating rates on the reaction mechanisms of nano and micron composite thermite reactions.* Journal of Thermal Analysis & Calorimetry, 2006. **85**(1): p. 37-43.
12. Granier, J.J. and M.L. Pantoya, *Laser ignition of nanocomposite thermites.* Combustion and Flame, 2004. **138**(4): p. 373-383.

13. Umbrajkar, S.M., S. Seshadri, M. Schoenitz, V.K. Hoffmann, and E.L. Dreizin, *Aluminum-rich Al-MoO3 nanocomposite powders prepared by arrested reactive milling.* J. Propul. Power, 2008. **24**(2): p. 192-198.
14. K. Sullivan, G. Young, and M.R. Zachariah, *Enhanced Reactivity of Nano-B/Al/CuO MICs.* submitted to Combustion and Flame., 2007.
15. Prakash, A., A.V. McCormick, and M.R. Zachariah, *Tuning the reactivity of energetic nanoparticles by creation of a core-shell nanostructure.* Nano Letters, 2005. **5**(7): p. 1357-1360.
16. Young, G., K. Sullivan, and M.R. Zachariah. *Investigation of Boron Nanoparticle Combustion*. in *46th AIAA Aerospace Sciences Meeting and Exhibit AIAA-2008-0942*. 2007. Reno, Nevada.
17. Son, S.F., B.W. Asay, T.J. Foley, R.A. Yetter, M.H. Wu, and G.A. Risha, *Combustion of nanoscale Al/MoO3 thermite in microchannels.* J. Propul. Power, 2007. **23**(4): p. 715-721.
18. Sanders, V.E., B.W. Asay, T.J. Foley, B.C. Tappan, A.N. Pacheco, and S.F. Son, *Reaction propagation of four nanoscale energetic composites (Al/MoO3, Al/WO3, Al/CuO, and Bi2O3).* J. Propul. Power, 2007. **23**(4): p. 707-714.
19. Shoshin, Y.L., M.A. Trunov, X. Zhu, M. Schoenitz, and E.L. Dreizin, *Ignition of aluminum-rich Al-Ti mechanical alloys in air.* Combustion and Flame, 2006. **144**(4): p. 688-697.
20. Trunov, M.A., M. Schoenitz, and E.L. Dreizin, *Ignition of aluminum powders under different experimental conditions.* Propellants Explos. Pyrotech., 2005. **30**(1): p. 36-43.
21. Plantier, K.B., M.L. Pantoya, and A.E. Gash, *Combustion wave speeds of nanocomposite Al/Fe2O3: the effects of Fe2O3 particle synthesis technique.* Combustion and Flame, 2005. **140**(4): p. 299-309.
22. Schoenitz, M., S. Umbrajkar, and E.L. Dreizin, *Kinetic analysis of thermite reactions in Al-MoO3 nanocomposites.* J. Propul. Power, 2007. **23**(4): p. 683-687.
23. Umbrajkar, S.M., M. Schoenitz, and E.L. Dreizin, *Exothermic reactions in Al-CuO nanocomposites.* Thermochimica Acta, 2006. **451**(1-2): p. 34-43.

24. Mei, J., R.D. Halldearn, and P. Xiao, *Mechanisms of the aluminium-iron oxide thermite reaction.* Scripta Materialia, 1999. **41**(5): p. 541-548.
25. Brill, T.B., M.C. Beckstead, J.E. Flanagan, M.C. Lin, T.A. Litzinger, R.H.W. Waesche, and C.A. Wight, *Chemical speciation and dynamics in the surface combustion zone of energetic materials.* J. Propul. Power, 2002. **18**(4): p. 824-834.
26. Higgins, K.J., H.J. Jung, D.B. Kittelson, J.T. Roberts, and M.R. Zachariah, *Size-selected nanoparticle chemistry: Kinetics of soot oxidation.* J. Phys. Chem. A, 2002. **106**(1): p. 96-103.
27. Knutson, E.O. and K.T. Whitby, *Aerosol classification by electric mobility: apparatus, theory, and applications.* Journal of Aerosol Science, 1975. **6**(6): p. 443-451.
28. Rai, A., K. Park, L. Zhou, and M.R. Zachariah, *Understanding the mechanism of aluminium nanoparticle oxidation.* Combustion Theory and Modelling, 2006. **10**(5): p. 843 - 859.
29. Ehara, K., C. Hagwood, and K.J. Coakley, *Novel method to classify aerosol particles according to their mass-to-charge ratio - Aerosol particle mass analyser.* Journal of Aerosol Science, 1996. **27**(2): p. 217-234.
30. Christopher A. Noble, K.A.P., *Real-time single particle mass spectrometry: A historical review of a quarter century of the chemical analysis of aerosols.* Mass Spectrometry Reviews, 2000. **19**(4): p. 248-274.
31. Kane, D.B., B. Oktem, and M.V. Johnston, *Nanoparticle detection by aerosol mass spectrometry.* Aerosol Science and Technology, 2001. **34**(6): p. 520-527.
32. Reents, W.D. and Z. Ge, *Simultaneous elemental composition and size distributions of submicron particles in real time using laser atomization/ionization mass spectrometry.* Aerosol Science and Technology, 2000. **33**(1-2): p. 122-134.
33. Murray, V.J., *Sampling and analysis of individual particles by aerosol mass spectrometry.* Journal of Mass Spectrometry, 2000. **35**(5): p. 585-595.
34. Jayne, J.T., D.C. Leard, X. Zhang, P. Davidovits, K.A. Smith, C.E. Kolb, and D.R. Worsnop, *Development of an aerosol mass spectrometer for size and*

composition analysis of submicron particles. Aerosol Science and Technology, 2000. **33**(1-2): p. 49-70.

35. Salt, K., C.A. Noble, and K.A. Prather, *Aerodynamic Particle Sizing versus Light Scattering Intensity Measurement as Methods for Real-Time Particle Sizing Coupled with Time-of-Flight Mass Spectrometry.* Anal. Chem., 1996. **68**(1): p. 230-234.
36. Milchberg, H.M., S.J. McNaught, and E. Parra, *Plasma hydrodynamics of the intense laser-cluster interaction.* Physical Review E: Statistical, Nonlinear, and Soft Matter Physics, 2001. **64**(5-2): p. 056402/1-056402/7.
37. Park, K., A. Rai, and M.R. Zachariah, *Characterizing the coating and size-resolved oxidative stability of carbon-coated aluminum nanoparticles by single-particle mass-spectrometry.* Journal of Nanoparticle Research, 2006. **8**(3-4): p. 455-464.
38. Mrowec, S. and Z. Grzesik, *Oxidation of nickel and transport properties of nickel oxide.* Journal of Physics and Chemistry of Solids, 2004. **65**(10): p. 1651-1657.
39. Rellinghaus, B., S. Stappert, E.F. Wassermann, H. Sauer, and B. Spliethoff, *The effect of oxidation on the structure of nickel nanoparticles.* European Physical Journal D, 2001. **16**(1-3): p. 249-252.
40. Fromhold, J.A.T., *Growth rate of low-space-charge oxides on spherical metal particles.* Journal of Physics and Chemistry of Solids, 1988. **49**(10): p. 1159-1166.
41. Atkinson, A., *Transport processes during the growth of oxide films at elevated temperature.* Reviews of Modern Physics, 1985. **57**(2): p. 437.
42. A. T. Fromhold, Jr., *Theory of Metal Oxidation Volume 2*. Vol. 2. 1980: North-Holland Publishing Company.
43. Sales, B.C., M.B. Maple, and F.L. Vernon, *Initial oxidation kinetics near the Curie temperature of nickel.* Physical Review B, 1978. **18**(1): p. 486.
44. Sales, B.C. and M.B. Maple, *Oxidation of Nickel in the Vicinity of Its Curie Temperature.* Physical Review Letters, 1977. **39**(25): p. 1636.

45. A. T. Fromhold, Jr., *Theory of Metal Oxidation Volume 1*. Vol. 1. 1976: North-Holland Publishing Company.
46. Graham, M.J. and M. Cohen, *On the Mechanism of Low-Temperature Oxidation (23[degree]--450[degree]C) of Polycrystalline Nickel.* Journal of The Electrochemical Society, 1972. **119**(7): p. 879-882.
47. Caplan, D., M.J. Graham, and M. Cohen, *Effect of Cold Work on the Oxidation of Nickel at High Temperature.* Journal of The Electrochemical Society, 1972. **119**(9): p. 1205-1215.
48. Fromhold, A.T. and E.L. Cook, *Kinetics of Oxide Film Growth on Metal Crystals: Electronic and Ionic Diffusion in Large Surface-Charge and Space-Charge Fields.* Physical Review, 1968. **175**(3): p. 877.
49. Pizzini, S. and R. Morlotti, *Thermodynamic and Transport Properties of Stoichiometric and Nonstoichiometric Nickel Oxide.* Journal of The Electrochemical Society, 1967. **114**(11): p. 1179-1189.
50. Fromhold, A.T. and E.L. Cook, *Kinetics of Oxide Film Growth on Metal Crystals: Thermal Electron Emission and Ionic Diffusion.* Physical Review, 1967. **163**(3): p. 650.
51. A. T. Fromhold, Jr. and L.C. Earl, *Diffusion Currents in Large Electric Fields for Discrete Lattices.* Journal of Applied Physics, 1967. **38**(4): p. 1546-1553.
52. Kazuo, F. and J. Bruce Wagner, Jr., *Studies of the Oxidation of Nickel in the Temperature Range of 900[degree] to 1400[degree]C.* Journal of The Electrochemical Society, 1965. **112**(4): p. 384-388.
53. A. T. Fromhold, Jr., *Parabolic Growth Law for Coherent Oxides.* The Journal of Chemical Physics, 1964. **41**(2): p. 509-514.
54. W. L. Phillips, Jr., *Oxidation Rates of Pure and Less Pure Nickel.* Journal of The Electrochemical Society, 1963. **110**(9): p. 1014-1015.
55. Carter, R.E., *Kinetic Model for Solid-State Reactions.* Journal of Chemical Physics, 1961. **34**(6): p. 2010-&.
56. Gulbransen, E.A. and K.F. Andrew, *High Temperature Oxidation of High Purity Nickel between 750-Degrees-C and 1050-Degrees-C.* Journal of the Electrochemical Society, 1957. **104**(7): p. 451-454.

57. Gulbransen, E.A. and K.F. Andrew, *The Kinetics of Oxidation of High Purity Nickel.* Journal of the Electrochemical Society, 1954. **101**(3): p. 128-140.
58. Dravnieks, A., *The oxidation of several metals in activated oxygen at high temperatures.* Journal of the American Chemical Society, 1950. **72**: p. 3761-7.
59. Cabrera, N. and N.F. Mott, *Theory of the Oxidation of Metals.* Reports on Progress in Physics, 1948. **12**: p. 163-184.
60. Wagner, C., *The theory of the warm-up process. Z.* Phys. Chem. Abt. B, 1933. **21**(25).
61. Niklasson, G.A. and R. Karmhag, *Oxidation kinetics of metallic nanoparticles.* Surface Science, 2003. **532**: p. 324-327.
62. Karmhag, R., G.A. Niklasson, and M. Nygren, *Oxidation kinetics of nickel nanoparticles.* Journal of Applied Physics, 2001. **89**(5): p. 3012-3017.
63. Karmhag, R., T. Tesfamichael, E. Wackelgard, G.A. Niklasson, and M. Nygren, *Oxidation Kinetics of Nickel Particles: Comparison Between Free Particles and Particles in an Oxide Matrix.* Solar Energy, 2000. **68**(4): p. 329-333.
64. Karmhag, R., G.A. Niklasson, and M. Nygren, *Oxidation kinetics of small nickel particles.* Journal of Applied Physics, 1999. **85**(2): p. 1186-1191.
65. Karmhag, R., G.A. Niklasson, and M. Nygren, *Oxidation kinetics of large nickel particles.* Journal of Materials Research, 1999. **14**(7): p. 3051-3058.
66. Zhou, L., A. Rai, N. Piekiel, X. Ma, and M.R. Zachariah, *Ion-Mobility Spectrometry of Nickel Nanoparticle Oxidation Kinetics: Application to Energetic Materials.* J. Phys. Chem. C, 2008. **112**: p. 16209-16218.
67. Kim, S.H., R.A. Fletcher, and M.R. Zachariah, *Understanding the difference in oxidative properties between flame and diesel soot nanoparticles: The role of metals.* Environmental Science & Technology, 2005. **39**(11): p. 4021-4026.
68. Park, K., D.B. Kittelson, M.R. Zachariah, and P.H. McMurry, *Measurement of inherent material density of nanoparticle agglomerates.* Journal of Nanoparticle Research, 2004. **6**(2-3): p. 267-272.
69. McMurry, P.H., X. Wang, K. Park, and K. Ehara, *The Relationship between Mass and Mobility for Atmospheric Particles: A New Technique for*

Measuring Particle Density. Aerosol Science and Technology, 2002. **36**(2): p. 227 - 238.

70. Sahoo, Y., Y. He, M.T. Swihart, S. Wang, H. Luo, E.P. Furlani, and P.N. Prasad, *An aerosol-mediated magnetic colloid: Study of nickel nanoparticles.* Journal of Applied Physics, 2005. **98**(5): p. 054308/1-054308/6.
71. He, Y.Q., X.G. Li, and M.T. Swihart, *Laser-driven aerosol synthesis of nickel nanoparticles.* Chem. Mat., 2005. **17**(5): p. 1017-1026.
72. Kim, S.H. and M.R. Zachariah, *In-flight kinetic measurements of the aerosol growth of carbon nanotubes by electrical mobility classification.* Journal of Physical Chemistry B, 2006. **110**(10): p. 4555-4562.
73. Higgins, K.J., H.J. Jung, D.B. Kittelson, J.T. Roberts, and M.R. Zachariah, *Kinetics of diesel nanoparticle oxidation.* Environmental Science & Technology, 2003. **37**(9): p. 1949-1954.
74. Jung, H., D.B. Kittelson, and M.R. Zachariah, *The influence of a cerium additive on ultrafine diesel particle emissions and kinetics of oxidation.* Combustion and Flame, 2005. **142**(3): p. 276-288.
75. Tsyganov, S., J. Kastner, B. Rellinghaus, T. Kauffeldt, F. Westerhoff, and D. Wolf, *Analysis of Ni nanoparticle gas phase sintering.* Physical Review B, 2007. **75**(4).
76. Antonsen, D.H. and D.T. Meshri, *Nickel compounds.* Kirk-Othmer Encyclopedia of Chemical Technology (5th Edition), 2006. **17**: p. 106-132.
77. Levenspiel, O., *Chemical Reaction Engineering*. 3rd ed. 1999: John Wiley & Sons.
78. Aiken, J.G. and A.G. Jordan, *Electrical transport properties of single crystal nickel oxide.* Journal of Physics and Chemistry of Solids, 1968. **29**(12): p. 2153-2167.
79. Mitchell, D.F. and M.J. Graham, *A kinetic study of the initial oxidation of Ni (111) and (211) surfaces by rheed and X-ray emission.* Surface Science, 1982. **114**(2-3): p. 546-562.

80. Huang, Y., G.A. Risha, V. Yang, and R.A. Yetter, *Combustion of bimodal nano/micron-sized aluminum particle dust in air.* Proceedings of the Combustion Institute, 2007. **31**(2): p. 2001-2009.
81. Valery, I.L., W.A. Blaine, F.S. Steven, and P. Michelle, *Melt dispersion mechanism for fast reaction of nanothermites.* Applied Physics Letters, 2006. **89**(7): p. 071909.
82. Lee, D., K. Park, and M.R. Zachariah, *Determination of the size distribution of polydisperse nanoparticles with single-particle mass spectrometry: The role of ion kinetic energy.* Aerosol Science and Technology, 2005. **39**(2): p. 162-169.
83. Zhou, L., K. Park, H.M. Milchberg, and M.R. Zachariah, *Understanding the Interaction of an Intense Laser Pulse with Nanoparticles: Application to the Quantification of Single Particle Mass Spectrometry.* Aerosol Science and Technology, 2007. **41**(9): p. 818-827.
84. Lezius, M., S. Dobosz, D. Normand, and M. Schmidt, *Explosion Dynamics of Rare Gas Clusters in Strong Laser Fields.* Physical Review Letters, 1998. **80**(2): p. 261.
85. Ditmire, T., T. Donnelly, A.M. Rubenchik, R.W. Falcone, and M.D. Perry, *Interaction of intense laser pulses with atomic clusters.* Physical Review A: Atomic, Molecular, and Optical Physics, 1996. **53**(5): p. 3379-3402.
86. Parra, E., I. Alexeev, J. Fan, K.Y. Kim, S.J. McNaught, and H.M. Milchberg, *Hydrodynamic time scales for intense laser-heated clusters.* Journal of the Optical Society of America B: Optical Physics, 2003. **20**(1): p. 118-124.
87. Ammosov, M.V., N.B. Delone, and V.P. Krainov, *Tunnel Ionization of Complex Atoms and Atomic Ions in a Varying Electromagnetic-Field.* Zhurnal Eksperimentalnoi I Teoreticheskoi Fiziki, 1986. **91**(6): p. 2008-2013.
88. Dahl, D.A., Scientific Instrument Services, Inc. www.simion.com: Ringoes, NJ.
89. Zhou, L., A. Rai, and M.R. Zachariah, *Component and morphology biases on quantifying the composition of nanoparticles using single-particle mass*

spectrometry. International Journal of Mass Spectrometry, 2006. **258**(1-3): p. 104-112.

90. Wang, S., C.A. Zordan, and M.V. Johnston, *Chemical Characterization of Individual, Airborne Sub-10-nm Particles and Molecules.* Anal. Chem., 2006. **78**(6): p. 1750-1754.
91. Zelenyuk, A. and D. Imre, *Single Particle Laser Ablation Time-of-Flight Mass Spectrometer: An Introduction to SPLAT.* Aerosol Science and Technology, 2005. **39**(6): p. 554-568.
92. Erdmann, N., A. Dell'Acqua, P. Cavalli, C. Gruening, N. Omenetto, J.-P. Putaud, F. Raes, and R. Dingenen, *Instrument Characterization and First Application of the Single Particle Analysis and Sizing System (SPASS) for Atmospheric Aerosols.* Aerosol Science and Technology, 2005. **39**(5): p. 377-393.
93. Carson, P.G., K.R. Neubauer, M.V. Johnston, and A.S. Wexler, *On-line chemical analysis of aerosols by rapid single-particle mass spectrometry.* Journal of Aerosol Science, 1995. **26**(4): p. 535-545.
94. McKeown, P.J., M.V. Johnston, and D.M. Murphy, *On-line single-particle analysis by laser desorption mass spectrometry.* Analytical Chemistry, 1991. **63**(18): p. 2069-73.
95. Neubauer, K.R., M.V. Johnston, and A.S. Wexler, *Chromium speciation in aerosols by rapid single-particle mass spectrometry.* International Journal of Mass Spectrometry and Ion Processes, 1995. **151**(2-3): p. 77-87.
96. Reilly, P.T.A., A.C. Lazar, R.A. Gieray, W.B. Whitten, and J.M. Ramsey, *The elucidation of charge-transfer-induced matrix effects in environmental aerosols via real-time aerosol mass spectral analysis of individual airborne particles.* Aerosol Science and Technology, 2000. **33**(1-2): p. 135-152.
97. Ge, Z., A.S. Wexler, and M.V. Johnston, *Multicomponent Aerosol Crystallization.* Journal of Colloid and Interface Science, 1996. **183**(1): p. 68-77.

98. Kane, D.B. and M.V. Johnston, *Size and Composition Biases on the Detection of Individual Ultrafine Particles by Aerosol Mass Spectrometry.* Environ. Sci. Technol., 2000. **34**(23): p. 4887-4893.

99. Ge, Z., A.S. Wexler, and M.V. Johnston, *Laser Desorption/Ionization of Single Ultrafine Multicomponent Aerosols.* Environ. Sci. Technol., 1998. **32**(20): p. 3218-3223.

100. Woods, E., G.D. Smith, Y. Dessiaterik, T. Baer, and R.E. Miller, *Quantitative Detection of Aromatic Compounds in Single Aerosol Particle Mass Spectrometry.* Anal. Chem., 2001. **73**(10): p. 2317-2322.

101. Cabalo, J., A. Zelenyuk, T. Baer, and R.E. Miller, *Two-color laser induced evaporation dynamics of liquid aerosols probed by time-of-flight mass spectrometry.* Aerosol Science and Technology, 2000. **33**(1-2): p. 3-19.

102. Morrical, B.D., D.P. Fergenson, and K.A. Prather, *Coupling two-step laser desorption/ ionization with aerosol time-of-flight mass spectrometry for the analysis of individual organic particles.* Journal of the American Society for Mass Spectrometry, 1998. **9**(10): p. 1068-1073.

103. Kim, S.H., B.Y.H. Liu, and M.R. Zachariah, *Synthesis of Nanoporous Metal Oxide Particles by a New Inorganic Matrix Spray Pyrolysis Method.* Chem. Mater., 2002. **14**(7): p. 2889-2899.

104. Kim, J.H., V.I. Babushok, T.A. Germer, G.W. Mulholland, and S.H. Ehrman, *Cosolvent-assisted spray pyrolysis for the generation of metal particles.* Journal of Materials Research, 2003. **18**(7): p. 1614-1622.

105. Lushnikov, A.A. and A.E. Negin, *Aerosols in Strong Laser-Beams.* Journal of Aerosol Science, 1993. **24**(6): p. 707-&.

106. Armstrong, R.L., *Aerosol Heating and Vaporization by Pulsed-Light Beams.* Applied Optics, 1984. **23**(1): p. 148-155.

107. Vyazovkin, S., *Thermal analysis.* Analytical Chemistry, 2006. **78**(12): p. 3875-3886.

108. Thynell, S.T., P.E. Gongwer, and T.B. Brill, *Condensed-phase kinetics of cyclotrimethylenetrinitramine by modeling the T-jump/infrared spectroscopy experiment.* J. Propul. Power, 1996. **12**(5): p. 933-939.

109. Brill, T.B., H. Arisawa, P.J. Brush, P.E. Gongwer, and G.K. Williams, *Surface Chemistry of Burning Explosives and Propellants.* J. Phys. Chem., 1995. **99**(5): p. 1384-1392.

110. Brill, T.B., P.J. Brush, K.J. James, J.E. Shepherd, and K.J. Pfeiffer, *T-Jump/FT-IR Spectroscopy: A New Entry into the Rapid, Isothermal Pyrolysis Chemistry of Solids and Liquids.* Applied Spectroscopy, 1992. **46**: p. 900-911.

111. Ward, T.S., M.A. Trunov, M. Schoenitz, and E.L. Dreizin, *Experimental methodology and heat transfer model for identification of ignition kinetics of powdered fuels.* Int. J. Heat Mass Transf., 2006. **49**(25-26): p. 4943-4954.

112. Furutani, H., H. Fukumura, H. Masuhara, S. Kambara, T. Kitaguchi, H. Tsukada, and T. Ozawa, *Laser-Induced Decomposition and Ablation Dynamics Studied by Nanosecond Interferometry. 2. A Reactive Nitrocellulose Film.* J. Phys. Chem. B, 1998. **102**(18): p. 3395-3401.

113. Makashir, P.S., R.R. Mahajan, and J.P. Agrawal, *Studies on Kinetics and Mechanism of Initial Thermal-Decomposition of Nitrocellulose - Isothermal and Nonisothermal Techniques.* J. Therm. Anal., 1995. **45**(3): p. 501-509.

114. Roberts, T.A., R.L. Burton, and H. Krier, *Ignition and Combustion of Aluminum Magnesium Alloy Particles in O-2 at High-Pressures.* Combustion and Flame, 1993. **92**(1-2): p. 125-143.

115. Blais, N.C., H.A. Fry, and N.R. Greiner, *Apparatus for the mass spectrometric analysis of detonation products quenched by adiabatic free expansion.* Rev. Sci. Instrum., 1993. **64**(1): p. 174-183.

116. Dauerman, L., G.E. Salser, and Y.A. Tajima, *Characterization of Volatilized Species from Solid Propellants.* Aiaa J., 1967. **5**(8): p. 1501-&.

117. Kim, E.S., H.S. Lee, C.F. Mallery, and S.T. Thynell, *Thermal decomposition studies of energetic materials using confined rapid thermolysis / FTIR spectroscopy.* Combustion and Flame, 1997. **110**(1-2): p. 239-255.

118. Hiyoshi, R.I. and T.B. Brill, *Thermal decomposition of energetic materials 83. Comparison of the pyrolysis of energetic materials in air versus argon.* Propellants Explos. Pyrotech., 2002. **27**(1): p. 23-30.

119. Brill, T.B. and H. Ramanathan, *Thermal decomposition of energetic materials 76: chemical pathways that control the burning rates of 5-aminotetrazole and its hydrohalide salts.* Combustion and Flame, 2000. **122**(1-2): p. 165-171.

120. Brill, T.B. and P.E. Gongwer, *Thermal decomposition of energetic materials 69. Analysis of the kinetics of nitrocellulose at 50 degrees C-500 degrees C.* Propellants Explos. Pyrotech., 1997. **22**(1): p. 38-44.

121. Morelli, J.J., *Thermal-Analysis Using Mass-Spectrometry - a Review.* J. Anal. Appl. Pyrolysis, 1990. **18**(1): p. 1-18.

122. Jones, D.E.G., R. Turcotte, B. Acheson, Q.S.M. Kwok, and M. Vachon, *The thermal decomposition of nitrocellulose.* International Annual Conference of ICT, 2003. **34th**: p. 46/1-46/17.

123. Mo Yang, J.M.R.B.J.K., *Laser-induced Selective Dissociation of Nitro Groups in Nitrocellulose.* Rapid Communications in Mass Spectrometry, 1996. **10**(3): p. 311-315.

124. Fowler, A.H.K. and H.S. Munro, *A preliminary investigation of the thermal and X-ray induced degradation of cellulose nitrates by FAB/SIMS and 13C NMR.* Polymer Degradation and Stability, 1985. **13**(1): p. 21-29.

125. Farber, M. and R.D. Srivastava, *A mass-spectrometric investigation of the chemistry of plateau burning propellants.* Combustion and Flame, 1978. **31**: p. 309-323.

126. Dauerman, L. and Y.A. Tajima, *Thermal Decomposition and Combustion of Nitrocellulose.* Aiaa J., 1968. **6**(8): p. 1468-&.

127. Blais, N.C., R. Engelke, and S.A. Sheffield, *Mass Spectroscopic Study of the Chemical Reaction Zone in Detonating Liquid Nitromethane.* J. Phys. Chem. A, 1997. **101**(44): p. 8285-8295.

128. Stiegman, A.E., M.L. Mileham, and M.P. Kramer, *Decomposition studies of thermite-based energetic materials using MALDI-TOF mass spectrometry.* Abstracts of Papers, 233rd ACS National Meeting, Chicago, IL, United States, March 25-29, 2007, 2007: p. INOR-176.

129. Mileham, M.L., M.P. Kramer, and A.E. Stiegman, *Laser Initiation Processes in Thermite Energetic Materials Using Laser Desorption Ionization Time-of-Flight Mass Spectrometry.* J. Phys. Chem. C, 2007. **111**(45): p. 16883-16888.

130. Maharrey, S. and R. Behrens, *Thermal Decomposition of Energetic Materials. 5. Reaction Processes of 1,3,5-Trinitrohexahydro-s-triazine below Its Melting Point.* J. Phys. Chem. A, 2005. **109**(49): p. 11236-11249.

131. Leanna Minier, Richard Behrens, and S. Bulusu, *Mass spectra of 2,4-dinitroimidazole and its isotopomers using simultaneous thermogravimetric modulated beam mass spectrometry.* Journal of Mass Spectrometry, 1996. **31**(1): p. 25-30.

132. Behrens, R., *New Simultaneous Thermogravimetry and Modulated Molecular-Beam Mass-Spectrometry Apparatus for Quantitative Thermal-Decomposition Studies.* Rev. Sci. Instrum., 1987. **58**(3): p. 451-461.

133. Korobein.Op, V.V. Boldyrev, and Y.Y. Karpenko, *Use of a Pulse Mass Spectrometer to Investigate High-Speed Processes Associated with High-Temperature Decomposition of Ammonium Perchlorate.* Combust. Explos., 1968. **4**(1): p. 19.

134. Chowdhury, A. and S.T. Thynell, *Confined rapid thermolysis/FTIR/ToF studies of imidazolium-based ionic liquids.* Thermochimica Acta, 2006. **443**(2): p. 159-172.

135. Wiley, W.C. and I.H. McLaren, *Time-of-Flight Mass Spectrometer with Improved Resolution.* Rev. Sci. Instrum., 1955. **26**(12): p. 1150-1157.

136. Chen, J.K. and T.B. Brill, *Thermal decomposition of energetic materials 50. Kinetics and mechanism of nitrate ester polymers at high heating rates by SMATCH/FTIR spectroscopy.* Combustion and Flame, 1991. **85**(3-4): p. 479-488.

137. Behrens, R. and S. Bulusu, *Thermal decomposition of energetic materials. 4. Deuterium isotope effects and isotopic scrambling (H/D, 13C/18O, 14N/15N) in condensed-phase decomposition of 1,3,5-trinitrohexahydro-s-triazine (RDX).* J. Phys. Chem., 1992. **96**(22): p. 8891-8897.

138. Behrens, R. and S. Bulusu, *Thermal decomposition of energetic materials. 3. Temporal behaviors of the rates of formation of the gaseous pyrolysis products from condensed-phase decomposition of 1,3,5-trinitrohexahydro-s-triazine (RDX).* J. Phys. Chem., 1992. **96**(22): p. 8877-8891.

139. Brill, T.B., P.J. Brush, S.A. Kinloch, and P. Gray, *Condensed Phase Chemistry of Explosives and Propellants at High-Temperature - Hmx, Rdx and Bamo.* Philosophical Transactions of the Royal Society of London Series a-Mathematical Physical and Engineering Sciences, 1992. **339**(1654): p. 377-385.

140. Xinsheng, Z., J.H. Eric, and T.L. Yuan, *Infrared multiphoton dissociation of RDX in a molecular beam.* The Journal of Chemical Physics, 1988. **88**(2): p. 801-810.

141. Henric, O. and R. Nils, *Laser ignition of pyrotechnic mixtures: Ignition mechanisms.* Journal of Applied Physics, 1993. **73**(4): p. 1993-2003.

142. Yang, Y., Z. Sun, S. Wang, and D.D. Dlott, *Fast Spectroscopy of Laser-Initiated Nanoenergetic Materials.* J. Phys. Chem. B, 2003. **107**(19): p. 4485-4493.

143. Moore, D.S., S.E. Son, and B.W. Asay, *Time-resolved spectral emission of deflagrating nano-Al and nano-MoO3 metastable interstitial composites.* Propellants Explos. Pyrotech., 2004. **29**(2): p. 106-111.

144. Trenkle, J.C., L.J. Koerner, M.W. Tate, S.M. Gruner, T.P. Weihs, and T.C. Hufnagel, *Phase transformations during rapid heating of Al/Ni multilayer foils.* Applied Physics Letters, 2008. **93**(8).

145. Ershov, A.P., *Ionization During Detonation of Solid Explosives.* Combust. Explos., 1975. **11**(6): p. 798-803.

146. Douglas, G.T., W.A. Blaine, C.K. James, V.E. Sanders, and F.S. Steven, *Dynamic measurements of electrical conductivity in metastable intermolecular composites.* Journal of Applied Physics, 2006. **99**(2): p. 023705.

147. Martirosyan, K.S., M. Setoodeh, and D. Luss, *Electric-field generated by the combustion of titanium in nitrogen.* Journal of Applied Physics, 2005. **98**(5).

148. Martirosyan, K.S., I.A. Filimonov, M.D. Nersesyan, and D. Luss, *Electric field formation during combustion of single metal particles.* Journal of the Electrochemical Society, 2003. **150**(5): p. J9-J16.

149. Martirosyan, K.S., J.R. Claycomb, G. Gogoshin, R.A. Yarbrough, J.H. Miller, and D. Luss, *Spontaneous magnetization generated by spin, pulsating, and planar combustion synthesis.* Journal of Applied Physics, 2003. **93**(11): p. 9329-9335.

150. Rai, A., D. Lee, K. Park, and M.R. Zachariah, *Importance of Phase Change of Aluminum in Oxidation of Aluminum Nanoparticles.* J. Phys. Chem. B, 2004. **108**(39): p. 14793-14795.

151. *Resistance Temperature Measurment: using RTDs*, OMEGA ENGINEERING, INC. : OMEGA's Temperature Technical Reference Section.

152. Park, K., D. Dutcher, M. Emery, J. Pagels, H. Sakurai, J. Scheckman, S. Qian, M.R. Stolzenburg, X. Wang, J. Yang, and P.H. McMurry, *Tandem Measurements of Aerosol Properties: Review of Mobility Techniques with Extensions.* Aerosol Science and Technology, 2008. **42**(10): p. 801 - 816.

153. Korogodov, V.S., A.I. Kirdyashkin, Y.M. Maksimov, A.A. Trunov, and R.M. Gabbasov, *Microwave radiation from combustion of an iron-aluminum thermite mixture.* Combust. Explos., 2005. **41**(4): p. 481-483.